Title: Modern Mars' geomorphological activity, driven by wind, frost, and gravity

Authors: Serina Diniega[1,*], Ali M. Bramson[2], Bonnie Buratti[1], Peter Buhler[3], Devon M. Burr[4], Matthew Chojnacki[3], Susan J. Conway[5], Colin M. Dundas[6], Candice J. Hansen[3], Alfred S. McEwen[7], Mathieu G. A. Lapôtre[8], Joseph Levy[9], Lauren Mc Keown[10], Sylvain Piqueux[1], Ganna Portyankina[11], Christy Swann[12], Timothy N. Titus[6], Jacob M. Widmer

[1]Jet Propulsion Laboratory, California Institute of Technology, 4800 Oak Grove Dr., Pasadena, CA 91009, USA
[2] Department of Earth, Atmospheric, and Planetary Sciences, Purdue University, 550 Stadium Mall Dr., West Lafayette, IN 47907, USA
[3]Planetary Science Institute, 1700 East Fort Lowell, Suite 106, Tucson, AZ 85719, USA
[4]Northern Arizona University, 537 S Beaver St, Flagstaff AZ 86011-6010, USA
[5] CNRS UMR 6112 Laboratoire de Planétologie et Géodynamique, Université de Nantes, 44330 Nantes, France
[6]U.S. Geological Survey, Astrogeology Science Center, 2255 N. Gemini Drive, Flagstaff, AZ 86001, USA
[7]Lunar and Planetary Laboratory, University of Arizona, 1629 E University Blvd, Tucson, AZ 85721, USA
[8]Department of Geological Sciences, Stanford University, 450 Jane Stanford Way, Stanford, CA 94305, USA
[9]Colgate University, 13 Oak Dr., Hamilton, NY 13346, USA
[10]National History Museum, Cromwell Rd, South Kensington, London SW7 5BD, United Kingdom
[11]Laboratory for Atmospheric and Space Physics, University of Colorado – Boulder, 1234 Innovation Dr., Boulder, CO 80303, USA
[12]U.S. Naval Research Laboratory, 4555 Overlook Ave. S.W., Washington, DC 20375, USA
*Correspondence author: serina.diniega@jpl.nasa.gov, +1 818-393-1487.

ABSTRACT

Extensive evidence of landform-scale martian geomorphic changes has been acquired in the last decade, and the number and range of examples of surface activity have increased as more high-resolution imagery has been acquired. Within the present-day Mars climate, wind and frost/ice are the dominant drivers, resulting in large avalanches of material down icy, rocky, or sandy slopes; sediment transport leading to many scales of aeolian bedforms and erosion; pits of

various forms and patterned ground; and substrate material carved out from under subliming ice slabs. Due to the ability to collect correlated observations of surface activity and new landforms with relevant environmental conditions with spacecraft on or around Mars, studies of martian geomorphologic activity are uniquely positioned to directly test surface-atmosphere interaction and landform formation/evolution models outside of Earth. In this paper, we outline currently observed and interpreted surface activity occurring within the modern Mars environment, and tie this activity to wind, seasonal surface CO_2 frost/ice, sublimation of subsurface water ice, and/or gravity drivers. Open questions regarding these processes are outlined, and then measurements needed for answering these questions are identified. In the final sections, we discuss how many of these martian processes and landforms may provide useful analogs for conditions and processes active on other planetary surfaces, with an emphasis on those that stretch the bounds of terrestrial-based models or that lack terrestrial analogs. In these ways, modern Mars presents a natural and powerful comparative planetology base case for studies of Solar System surface processes, beyond or instead of Earth.

KEY WORDS

Geomorphological activity; Mars; Comparative Planetology; Aeolian; Sublimation; Mass wasting

HIGHLIGHTS

- Mars' surface is actively shaped in the present due to wind, frost/ice, and gravity.
- Overlapping, high-resolution images from orbit are key for detection of activity.
- In situ and orbital data are needed to fully characterize the active Mars processes.
- Mars studies provide critical information about activity beyond that seen on Earth.

1 Introduction

Numerous studies since the early Mars missions have documented evidence of surface activity on Mars (e.g., Figure 1), but it was only with the advent of high-resolution and repeat imaging over multiple martian years that the full scope of present-day martian surface activity, including topographic changes, has been appreciated. Direct observations of geomorphological activity, over all areas of Mars (Figure 2), has enabled testing of hypotheses about the driving conditions and processes causing observed changes. In particular, many of the types of landforms hypothesized to be recently formed have been shown to form or be modified in the present day, with observations and models tying activity rates and timing to frost(s), wind, and gravity (i.e., movement down slopes).

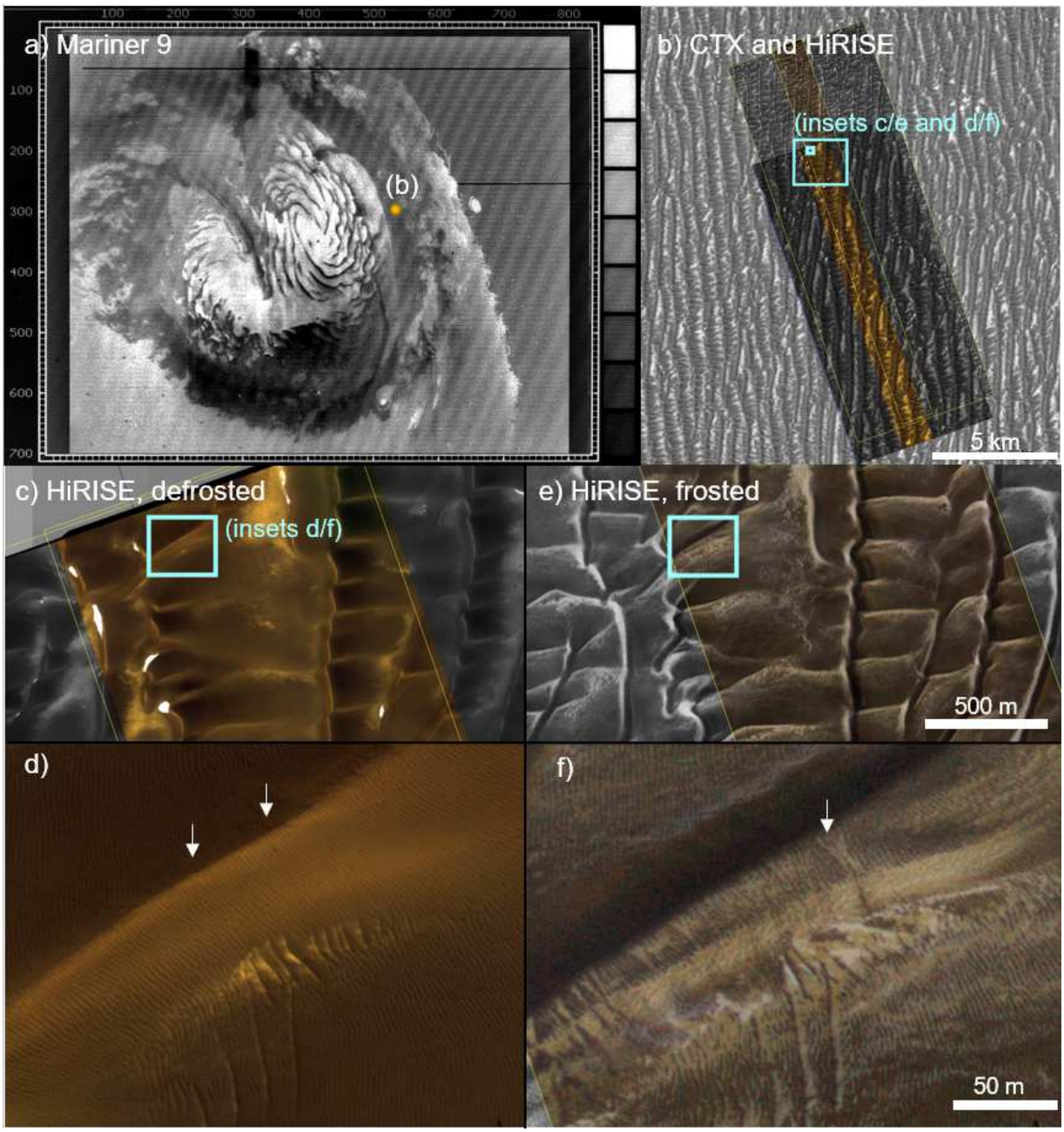

Figure 1. Example images of early and recent images of martian polar dunes, and the details that become apparent in zoomed-in images. (*a*) Mariner 9 image of the north polar cap and polar erg, acquired 1972-10-12 (= Mars Year (MY) 10 L_s 95°, see §1.2 for date nomenclature), ~3 km/px (MTVS 4297-47). (*b*) Basemap is from CTX images (~5 m/px) and shown are 2 pairs of monochromatic and false color HiRISE images (50 cm/px): ESP_027012_2610, acquired 2012-05-01 (MY 31 L_s 104°) and ESP_058950_2610, acquired 2019-02-22 (MY 34 L_s 345°). At L_s 104° (early summer), the seasonal frost layer is subliming, with only a few small patches of ice remaining (i.e., the bright spots). The large ripples are clearly visible on the dunes (§2.1.3), along with a few new dune furrows (arrows; §3.3.2). At L_s 354° (end of winter), the surface is completely covered in CO_2 frost, so is more uniform in color and brighter. Some underlying

ripples are visible beneath the frost, as is a new dune alcove (arrow; §3.2.2). The false color scheme is based on an automatic contrast enhancement algorithm with further manual tweaks to increase visibility of small features. The dunes are dark in color because they are made of basalt and the interdune substrate is lighter, with frost/ice brightest. North is up and illumination is from the left in all HiRISE images. Scale bars are approximate as images are not orthorectified.

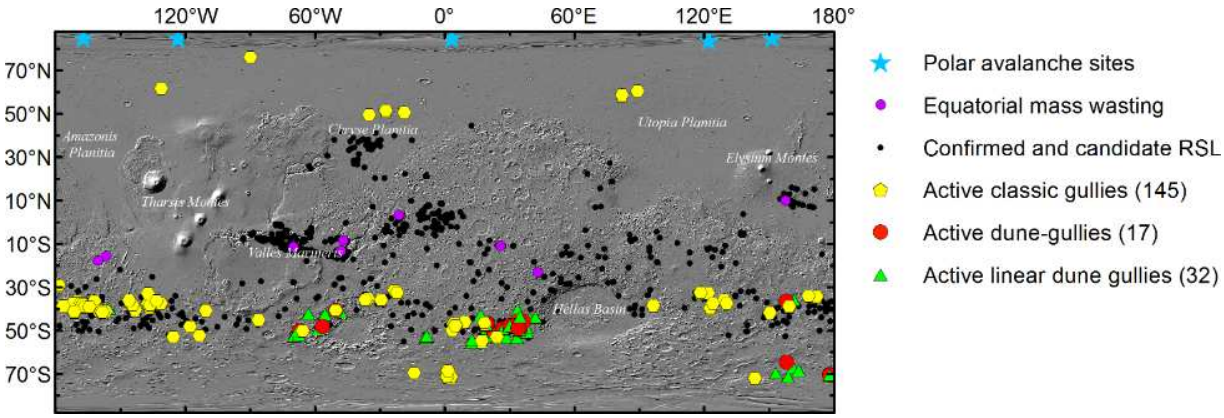

Figure 2. Map showing observations of activity for features where global surveys have been completed; note that this map is incomplete due to the patchy spatial coverage of repeat imaging: monitoring locations for polar avalanches (*Becerra et al.*, 2020) and presumed to occur at all steep scarps, equatorial mass-wasting (*M.F. Thomas et al.*, 2020), RSL (*Stillman et al.,* 2020), classic gullies (*Dundas et al.*, 2019a), dune gullies (*Dundas et al.*, 2019a; *Diniega et al.*, 2010), and linear dune gullies (*Dundas et al.*, 2019a; *Pasquon et al.*, 2016).

Studies of present-day geomorphological activity, especially if tied to correlated observations of activity and the relevant environment, are uniquely positioned to directly test surface-atmosphere interaction and landform formation/evolution models. Such studies are of great importance for understanding Mars' environmental and geologic history because landforms can serve as proxy records of specific processes and environmental conditions, such as surface thermo/mechanical properties, grain size(s), and wind velocities and variability. Studies of present-day activity on Mars are also uniquely enabling for studies of processes active on other planetary bodies because these either provide a matchless detailed planetary data point outside of Earth's gravity, atmosphere, and other conditions for comparison to terrestrial studies and derived models, or provide a detailed look into a process that has no terrestrial analog.

This review is on martian landforms that can be robustly connected to specific surface environmental conditions and processes. We focus on martian surface activity that *(1)* is observed or hypothesized to be happening in the present climate (albeit, in some cases, potentially at very slow, not yet directly observable rate), and *(2)* creates a specific and

166 interpretable change to the martian rocky or icy surface's shape that can be detected for >1
167 martian year.
168 Throughout this paper, we discuss the "modern Mars" environment, and in particular on the
169 present martian climate, which has been observed at high frequency and resolution over the last
170 few decades via spacecraft. However, modern Mars also includes the "recent" climate—a term
171 generally used to refer to the time since the last major obliquity excursion (around 500 kyr,
172 *Laskar et al.*, 2004), as this is the time period for the most recent significant sculpting of the
173 currently observable landscape. This time period is important as it is the only period where direct
174 characterization of the environment, based on present-day measurements, can be paired with
175 specific surface changes and thus hypothesized landform formation and evolution models can be
176 robustly tested with observations. Additionally, the climate conditions during the present and
177 recent past are thought to be representative of the martian climate over the last few billion years.
178 Throughout this period, called the Amazonian, Mars is thought to have been dry and cool, with
179 very low surface pressures and little liquid water. (Recent studies and our present understanding
180 about the Amazonian climate are summarized in *Diniega and Smith*, 2020.) Thus, while this
181 review focuses on activity that has been observed in or hypothesized to be occurring in the
182 present day, what we learn about surface-altering processes and driving environmental
183 conditions is likely to be relevant through a few billion years of Mars' geological and
184 climatological history—and so interpretations of even relict landscapes should take into account
185 the presently observed surface-altering processes.
186 In this review, we will outline observed and interpreted surface activity occurring within the
187 modern Mars environment. This activity, when tied to specific environmental drivers, has been
188 shown to be primarily caused by wind- and frost-related processes, although in many cases the
189 exact mechanism driving the geomorphological change has not yet been determined. The frost or
190 ice involved in present-day landform evolution is of two broad classes: the atmosphere-sourced
191 CO_2 and H_2O frost that accumulates each winter on the martian surface, and the previously
192 buried/preserved ice deposits beneath the martian surface or within the polar cap that now are
193 undergoing long-term loss (although for the cap, short-term loss occurs in some areas but it is
194 unclear if there is total net long-term loss or gain). Three sections describe landforms with
195 formation mechanisms associated with wind (i.e., aeolian features) and these two classes of frost.
196 Gravity also plays a role as many of these landforms involve material moving downslope (i.e.,

mass-wasting features). In a separate section, we describe a few landforms where the initiation of or additional environmental control on such downslope movement has not yet been determined.

In each of these sections, after outlining what is known, we outline open questions about the exact processes and environmental thresholds/controls. We also summarize current big questions about the martian surface and atmosphere environment in the present and through the Amazonian that could be addressed through continued study of these specific surface changes and landforms. Additionally, we identify the measurements needed to answer these questions. Finally, we discuss how many of these environmental conditions and processes may provide useful analogs for conditions and processes active on other planetary surfaces, with an emphasis on those that lack terrestrial analogs and for which Mars is a more natural comparative planetology base case.

1.1 Why focus on wind and sublimation as drivers for surface activity?

Some of the earliest Mars investigations via Earth-based telescopes or spacecraft observed Mars' atmosphere and seasonal frost (e.g., *Johnson*, 1965; *Lowell*, 1895). Orbital observations have enabled tracking of seasonal frost caps (§3.1) and movement of dust and sand (§2), as reflected in bedform movement and regional albedo changes. In situ indications of wind and at least trace amounts of seasonal frost (H_2O and/or CO_2) have been observed by all Mars landers that have survived through a martian winter (missions listed in Table 2, references listed in §3.1). The northernmost lander (*Phoenix*) even had one of its solar panels crushed due to accumulation of a thick layer of frozen CO_2 (https://www.nasa.gov/mission_pages/phoenix/news/phx20100524.html). Evidence that both wind and seasonal frost affect landform evolution has built up over the last two decades as the martian surface environment and morphology, and changes in the surface morphology, have been observed and characterized globally at sub-landform-scales and in places at sub-meter-scale resolution (§2–3, 5). As shown in Figure 3, many of the examples of observed present-day surface changes appear to be explained through some combination of wind, annual frost/ice formation or sublimation, and gravity (i.e., mass wasting). Close study of these landforms/surface changes along with concurrent measurement of their environment enables testing and refinement of quantitative models of the underlying processes, under Mars conditions.

In addition, there are martian landforms that have not yet been directly observed to form and change, but which are interpreted to be forming in the present climate due to long-term (i.e., multi-annual) sublimation or modification of surface or subsurface water ice reservoirs (§4). Such landforms are also important to study, again with concurrent detailed measurement of their present environments, because they provide a bridge to a recent past climate when that ice was deposited.

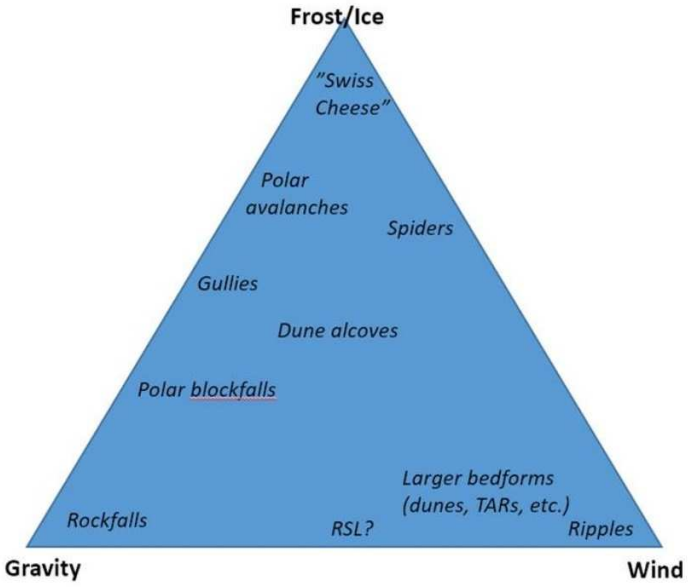

Figure 3. A ternary diagram illustrating the proposed relative controls by frost/ice, wind, and gravity on many of the landforms discussed in this review (§2–3, 5). (Not included here are the landforms created through long-term subsurface ice processes, §4, and landforms not discussed within this paper.)

Beyond wind and frost, a few other known or hypothesized present-day surface processes are widespread and can move large amounts of material over the martian surface. However, for reasons described here, these processes and landforms are not discussed further within this paper.

- Rocky landforms and textures that appear similar to terrestrial features formed through wind erosion, such as ventifacts (*Laity and Bridges*, 2009) and yardangs (*Liu et al.*, 2020; *Ward*, 1979) have been identified on Mars. Such erosion is likely occurring in the present martian climate but would be occurring at very slow rates; terrestrial sand abrasion occurs at tens to thousands of microns per year (discussed in *Laity and Bridges*, 2009) and bulk Mars surface aeolian erosion rates are at the low end of that range (§2.2.3). Thus, we are not yet able to draw quantitative connections to specific environmental conditions, including roughly when these environmental conditions existed, and constrained modeling of the formation process is difficult. Hence, we do not discuss such landforms in this review.
- Impact cratering is also actively changing the shape of the martian surface in the present climate (e.g., *Daubar et al.*, 2013; 2019), but the dominant controls for that process are

characteristics of the impactor and the impacted surface structure, not the environment at the time of impact. Thus, impactor-related processes are not a focus of this review.

- We will not discuss processes that generally change the appearance of the surface by moving around only a surficial layer, such as insolation-driven dust lifting or dust devils (*Balme and Greeley*, 2006) or thin slope streaks (*Chuang et al.*, 2007), although slope streaks do occasionally transport greater thicknesses (*Dundas*, 2020b). Such processes do not yield a significant change in the shape of the landscape and/or a clear geomorphic change retained for >1 martian year, and so are considered beyond the scope of this study. One exception is recurring slope lineae (RSL, discussed in §5.1), which is a landform of recent high interest.

Other drivers, such as volcanism or liquid water, have been proposed to explain observed geomorphologies and, in a few cases, observed surface activity. Some studies have suggested that these other drivers may be important and influential for shaping martian geology during the Amazonian and into the present. However, as outlined above, we focus this review on geomorphic processes known or generally thought to be active in the present day, and processes where existing observations of the martian environment are (so far) at least qualitatively consistent with the models we describe. For example, we note that this review does not include discussion of liquid water-driven geomorphic activity because, although many studies have proposed recent or present-day water-driven activity to explain observed geomorphologies (e.g., *Chevrier and Rivera-Valentin*, 2012; *Malin et al.*, 2006), no studies have yet been able to explain a water source that is consistent with all environmental observations or with behaviors/timing of activity that is consistent with observations of changes. In addition to liquid water-driven processes, volcanism, tectonics, glacial flow, rainfall, and biological activity will not be discussed within this review.

1.2 Sources of seminal data

The primary data that have led to studies of present-day surface geomorphological changes have been high-resolution visible images that allow for identification of smaller surface features and changes. For the latter, a key enabler were visible images of the same site, repeated over time—between the high resolution of these images (down to 0.25 cm/px by the Mars Reconnaissance Orbiter (MRO) High Resolution Imaging Science Experiment (HiRISE)) and a longer temporal baseline (currently at seven martian years for the highest-resolution images;

292 longer for comparisons to coarser resolution data: Table 1), many more examples of surface
293 changes have been identified. An example of such repeat images is shown in Figure 4;
294 comparisons of such images need to consider different resolutions and illumination conditions
295 (i.e., time of day).
296 In discussions of the timing of observed activity, we use the common Mars Year (MY – note
297 the difference from million years = Myr) and solar longitude (L_s) nomenclature. Enumeration of
298 Mars Years and seasons is described in detail by *Piqueux et al.* (2015a), but a brief description is
299 as follows:
300 • A Mars year is nearly twice as long as an Earth year (~687 Earth days).
301 • The solar longitude denotes the position of Mars in its orbit, running from L_s 0° to 360°.
302 (Due to Mars' orbital eccentricity, a degree of L_s spans 1.5-2.2 martian days or 'sols'.)
303 • A Mars Year starts at L_s 0° = northern spring equinox, and proceeds to L_s 90° = northern
304 summer solstice, L_s 180° = northern autumnal equinox, and L_s 270° = northern winter
305 solstice.
306 • MY 1, L_s 0° started on April 11, 1955.
307 After a surface change has been clearly identified, science investigations of that present-day
308 activity generally aim to identify the driving environmental conditions and relevant processes.
309 With visible imagery, a temporal survey can be done over a sequence of overlapping images to
310 determine when the change occurs, or a spatial survey can be used to constrain where this
311 landform exists (as well as where it doesn't exist). With other observational datasets,
312 environmental information can be gathered—for example:
313 • spectral data can yield constraints for the surface composition;
314 • atmospheric observations and modeling can yield information about wind patterns and
315 surface pressure variations; and
316 • topographic data, measurements of shadows, or photoclinometry analysis can yield
317 estimates of heights and slopes.
318 Such environmental information can be gathered from orbit or in situ. Table 2 contains a listing
319 of the Mars rovers and landers often referenced in studies of present-day activity and
320 surface/atmosphere environmental conditions.
321

322 Table 1. Primary instruments used to acquire orbital visible imagery used in studies of present-day surface activity, in reverse
323 chronological order of start of operations. To definitively measure a feature or surface change in an image, at least three pixels are
324 generally needed. The date of last contact is used to denote the end of operations.

Instrument	**Spacecraft**	**Period of Operation**	**Nadir Pixel Scale**	**Field of View**	**Global Coverage (as of July 2020)**
Colour and Stereo Surface Imaging System (CaSSIS: *N. Thomas et al.*, 2017)	ESA's ExoMars Trace Gas Orbiter (TGO)	2016-11-22 to present	~5 m/px	>8 km-wide swath in 3-colors or >6 km-wide swath in 4 colors; typical length of 50 km	Total area of images is 2.3%, but <1.6% after removing overlap
High Resolution Imaging Science Experiment (HiRISE: *McEwen et al.*, 2007)	NASA's Mars Reconn-aissance Orbiter (MRO)	2006-03-24 to present	~0.3 m/px for most images (from 300 km altitude)	6 km-wide swath in grayscale, with nested 1.2 km wide swath in 3-colors; typical length of 10 km	Total area of images is 3.6%, but <2.5% after removing overlap
Context (CTX) Camera (*Malin et al.*, 2007)		2006-04-13 to present	~6 m/px (from 300 km altitude)	30 km-wide swath in grayscale; typical length of 90 km	~100%, and a global mosaic has been created (*Dickson et al.*, 2018)
High Resolution Stereo Camera (HRSC: *Neukum et al.*, 2004a)	ESA's Mars Express (MEx)	2004-01-14 to present	~10 m/px for nadir channel (from 250 km altitude)	53 km-wide swath in 4-colors with length at least 300 km for regular images	~75% with resolution 10-20 m/px; 100% with resolution >100 m/px (*Gwinner et al.*, 2019)
Mars Orbital Camera (MOC: *Malin et al.*, 1992)	NASA's Mars Global Surveyor (MGS)	1997-09-15 to 2006-11-02	1.4–12 m/px for narrow angle; 225–7500 m/px for wide angle (from 378 km altitude)	3 km-wide swath in grayscale for narrow angle; 115 km-wide swath in 2-colors for wide angle; typical length of 30 km	0.5% at better than 3 m/px; 5.45% at better than 12 m/px (*Malin et al.*, 2010); 100% for wide angle

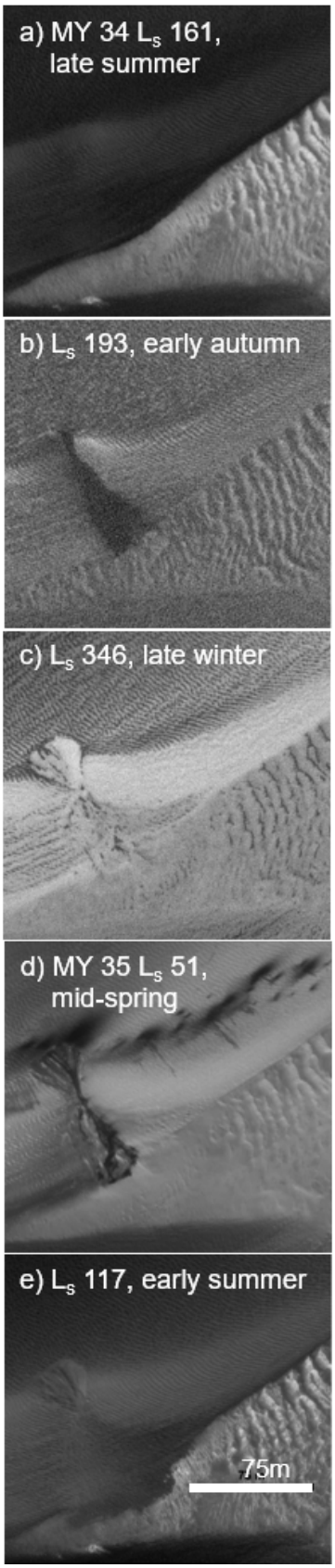

Figure 4. An example of how repeat imagery enables identification of activity, with timing constraints. In this chronological sequence of images, the polar dune slope (Tleilax dune field, 83.5°N, 118.5°E) becomes covered with frost and a new dune alcove forms *(b)* during L_s 161–193° (and likely during L_s 180–189°, intervening images are shown in SOM1). The alcove has formed by L_s 346° (*c*) and is clearly present under the seasonal frost layer. Sublimation begins in spring, with spots appearing preferentially along the dune brink and within the alcove and apron *(d)*. Sublimation completes L_s 51–117°. HiRISE images are (*a*) ESP_054971_2635, (*b*) ESP_055683_2635, (*c*) ESP_058967_2635, (*d*) ESP_060734_2635, and *(e)* ESP_062633_2635. A scale bar is shown in the last image (75 m), but absolute distances are approximate as images are not orthorectified. North is up and illumination is from the left.

Table 2. Successful Mars rovers and landers are often referenced in studies of present-day activity and surface/atmosphere environmental conditions, as these provide critical in situ data. These are listed here, in reverse chronological order of start of operations. For missions that have ended, the date of last contact is given to denote the end of operations.

Mission/*Spacecraft*	**Landing site**	**Period of Operation**
NASA's *InSight* lander	4.5°N, 135.9°E Elysium Planitia	2018-11-26 to present
NASA's Mars Science Laboratory (MSL) rover, *Curiosity*	4.6°S, 137.4°E Gale crater	2012-08-06 to present
NASA's *Phoenix* lander	68.2°N, 234.3°E Vastitas Borealis	2008-05-05 to 2008-11-02
NASA's Mars Exploration Rover (MER)-B, *Opportunity*	1.9°S, 354.5°E Meridiani Planum	2004-01-25 to 2018-06-10
NASA's Mars Exploration Rover (MER)-A, *Spirit*	14.6°S, 175.5°E Gusev crater	2004-01-04 to 2010-03-22
NASA's Mars Pathfinder *Sojourner* rover	19.1°N, 326.7°E Ares Vallis	1997-07-04 to 1997-09-27
NASA's *Viking* 2 lander	47.64°N, 134.3°E Utopia Planitia	1976-09-03 to 1980-04-12
NASA's *Viking* 1 lander	22.27°N, 312.1°E Chryse Planitia	1976-07-20 to 1982-11-11

2 Wind-formed landforms

Although the martian atmosphere is very thin compared to the Earth's (~0.1–1% surface pressure; e.g., *Banfield et al.*, 2020; *Harri et al.*, 2014; *Hess et al.*, 1976; *Taylor et al.*, 2010; *Withers and Smith*, 2006), wind-driven sediment transport has been observed (e.g., *Baker et al.*, 2018a; 2018b*; Bridges et al.*, 2012a; 2012b; 2017) and aeolian bedforms analogous to terrestrial features have been found over all scales. These include decimeter- and decameter-scale windblown ripples (e.g., *Lapôtre et al.*, 2018; *Silvestro et al.*, 2010), migrating barchan dunes (e.g., *Chojnacki et al.*, 2015; 2018; 2019), and megadunes (e.g., Figure 5; *Silvestro et al.*, 2012). In many cases, higher-resolution images show that multiple scales of bedforms are superimposed over each other (Figures 5, 6), reflecting the dominant local wind conditions over different spatial and temporal scales and potentially different types of surface-atmosphere interaction dynamic regimes (e.g., see §2.2). Studies of these bedforms have yielded much insight into atmospheric characteristics, wind directions and speeds (and variability), surface grain characteristics and availability, and sediment fluxes (as summarized for a range of planetary bodies in *Diniega et al.*, 2017). Environmental and geologic history, as inferred from these bedforms and the grains that compose them, are the focus of much of this section. Additionally,

we briefly describe some of the fundamental models used to relate atmospheric and grain characteristics to sediment fluxes (§2.2).

Sediment flux rates can also be estimated based on the appearance of denuded surfaces and degraded crater forms, where the amount of removed sediment and absolute age of the present surface can be estimated (§2.2.3). Wind-driven erosion can also be inferred from features such as yardangs and ventifacts which are common on the martian surface; however, rates of erosion or sediment flux are difficult to estimate from studies of these features, so we do not discuss them in this review.

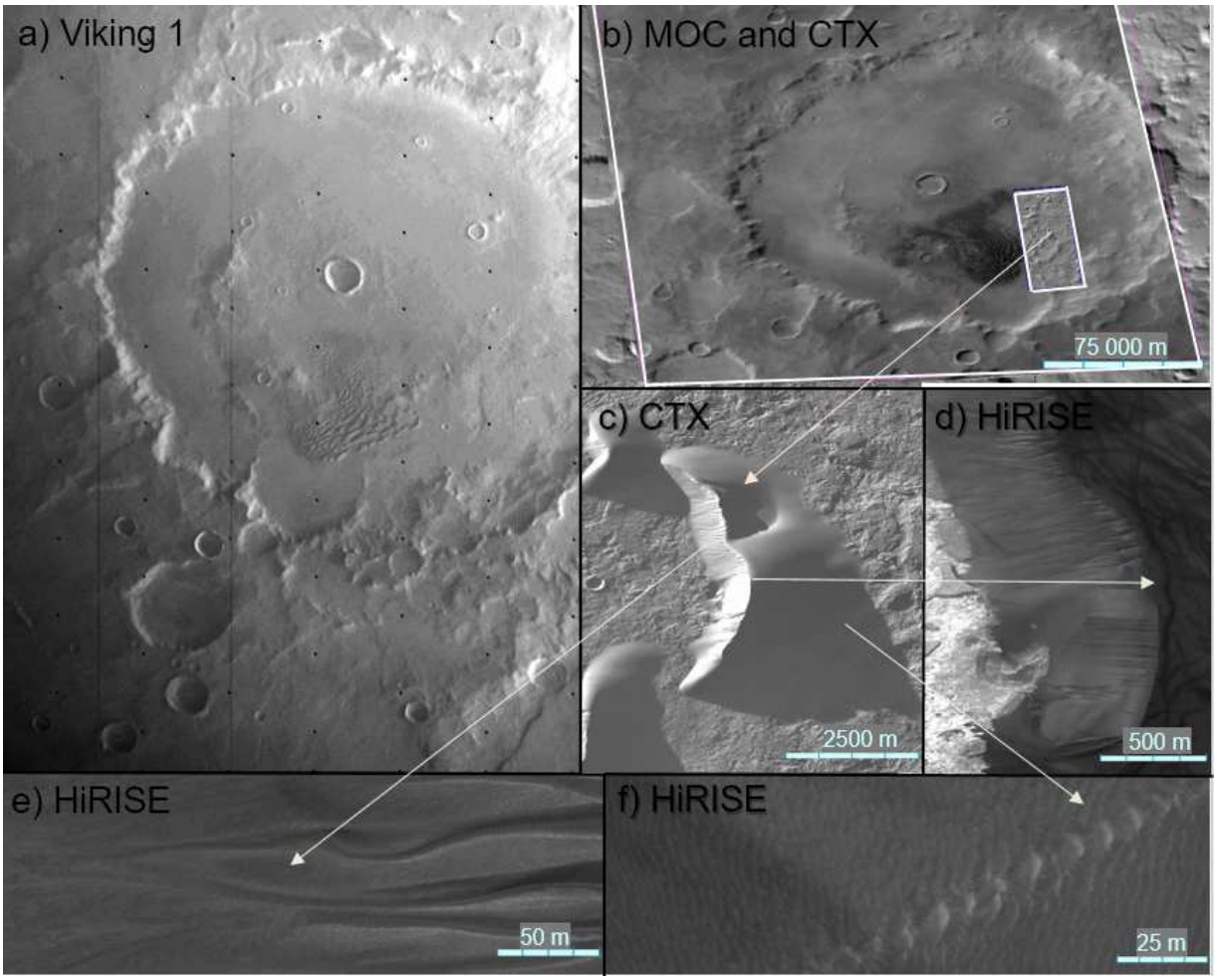

Figure 5. Images of Kaiser crater (47.4°S, 18.8°E) and its dunes, acquired over the last 50 years. *(a)* This Viking 1 image (094A42) was acquired 1976-09-22 (MY 12 L_s 126°) and has a resolution of 259 m/px. The identification of a dune field in a nearby crater in a Mariner 9 image was the first indication that sufficient sediment transport for bedform development was occurring in the thin martian atmosphere (*Sagan et al.*, 1972 -- see Figure 11, image ID MTVS 4264:16). However, >20 years later, the MOC camera on the Mars Global Surveyor orbiter reimaged

Kaiser crater (the large image in *(b)*: MOC M0101026, was acquired MY 24 L_s 137° or 1999-05-11). While some MOC images had resolution ~5 m/px, the image shown in *(b)* is of resolution 233 m/px – but in all cases, no signs of dune shape change or migration were identified. It wasn't until MRO arrived that clear signs of present-day activity were identified: *(b/c)* this CTX image (P21_009193_1329_XI_47S339W, acquired MY 29 L_s 97° or 2008-07-12) with resolution <4 m/px showed mass-wasting features in the barchan megadune. HiRISE images of that same dune yielded clear information about surface activity, including: dust devil tracks (the dark curvy lines along the upwind/right slope of the dune in *(d)*), large-scale mass-wasting in the dune gullies along the southern side of the downwind slope of the dune in *(d)* (first reported in *Diniega et al.*, 2010), *(e)* small-scale downslope sediment avalanching is evident in surface roughness changes over the ripple patterns, and *(f)* several scales of ripples migrating up the stoss dune slope. The HiRISE image shown in *(d-f)* is ESP_058972_1330_RED (acquired 2019-02-24 or MY 34 L_s 346°, resolution 0.25 m/px). The arrows extending from *(b)* to *(c)* and from *(c)* to *(d-f)* are to show the locations of the zoom-in views. The megadune that is the main landform within (*c,d*) is ~750 m tall—the largest known barchan dune in the Solar System. In all images, north is up. In the Viking image illumination is from the bottom right; in the MOC image illumination is from the upper left; in the CTX and HiRISE images illumination is from the upper left. Contrast has been tweaked to bring out details for each view.

2.1 Depositional and Erosional Aeolian Landscapes: Materials and Landforms

2.1.1 Wind-transported sediment grain properties

In situ observations of bedforms and transported grains by MER showed that a variety of grain sizes, from dust (<62 µm diameter) to sand (up to 2 mm) to granules (> 2 mm) (*Greeley et al.*, 2006; *Sullivan et al.*, 2008), are transported via present-day aeolian processes. *Curiosity* visited the Bagnold dune field and confirmed that martian dune sand was unimodally distributed in the very-fine-to-fine sand range, with median grain size of 100–150 µm (*Ehlmann et al.*, 2017; *Ewing et al.*, 2017; *Lapôtre et al.*, 2016; *Sullivan and Kok*, 2017; *Weitz et al.*, 2018). This countered early hypotheses, based on coarse resolution (2–30 km/px) orbital thermal measurements, that martian dune sand was composed of coarse sand grains with diameter ~500 µm (*Edgett and Christensen*, 1991; *Pelkey and Jakosky*, 2002); *Edwards et al.* (2018) suggested that some of these previous estimates may have overestimated grain size due to subpixel mixing of sandy and rocky materials. Much of the dune sands actively transported on Mars today are likely to be similar in size to the grains found in the Bagnold dunes because this size is thought to be most easily mobilized by winds (§2.2.1).

Coarser grains have been observed by *Curiosity* along the crest of large ripples along the trailing edge of the Bagnold dune field (median ~ 350 µm; *Weitz et al.*, 2018), where coarse grains are expected to concentrate based on analogy with terrestrial dune fields (*Ewing et al.*, 2017; *Lapôtre et al.*, 2016), as well as along the crests of isolated ripples (e.g., *Day and Kocurek*,

2016), in a sand shadow (*Minitti et al.*, 2013), and in ripple fields outside of the Bagnold dunes (median ~300–500 μm with <~1% grains >1 mm; *Weitz et al.*, 2018). Some of these coarser-grained ripples were covered in dust (*Lapôtre et al.*, 2018; Weitz et al., 2018), similar to observations by the *Spirit* rover at El Dorado (*Sullivan et al.*, 2008). On bedrock surfaces, coarser sediments (~1–3 mm) appear to be mobilized by aeolian processes (*Baker et al.*, 2018a).

Other observations of contiguous dune fields near their putative sand sources show decreasing thermal inertia downwind, suggesting some grain size variability (*Chojnacki et al.*, 2014). Alternatively, in situ investigations have shown surface crusts composed of dust, including on bedforms, that have been suggested to form from slow chemical weathering and/or salt formation as duricrusts (*Ewing et al.*, 2017; *McSween et al.*, 2004; *Moore et al.*, 1999; *Sullivan et al.*, 2008). This apparent induration of dusty bedform surfaces may play a role in the occurrences of lithified dune fields found with largely intact morphologies (*Chojnacki et al.*, 2020; *Edgett and Malin*, 2000; *Milliken et al.*, 2014).

In situ observations of grains generally find them to be subangular with high circularity (e.g., *Ehlmann et al.*, 2017; *Weitz et al.*, 2018), which is consistent with the observed properties of many smaller grains in desert aeolian systems on Earth (e.g., *Goudie and Watson*, 1981). Slip faces of dunes and large ripples at Gale crater have Earth-like ~30° angle of repose, with a few steeper outliers, possibly indicating local cohesion but otherwise largely loose sand (*Atwood-Stone and McEwen*, 2013; *Ewing et al.*, 2017). Their results are consistent with MER in situ observations of grains that suggest low-to-no cohesion in non-dusty aeolian materials (*Sullivan et al.*, 2008).

2.1.2 Wind-transported sediment composition

One important control in aeolian processes is the source of wind-transported sediment because the source region influences the availability of sediment and physical properties of the grains. (Here we discuss primarily the 'latest' erosion-source of the sediment, which is not necessarily the original source because grains presently eroding out of a crater or icy wall may be exhumed from sedimentary deposits formed during past aeolian transport (e.g., *Chojnacki et al.*, 2014b; *Fenton*, 2005; *Tirsch et al.,* 2011).) In some areas the sources of sediment are easy to identify in visible images, such as in the north polar erg where sand is clearly seen to be eroding from within the north polar basal unit (*Byrne and Murray,* 2002; *Massé et al.*, 2012; *Tsoar et al.*, 1979; SOM 2). In other areas, it is likely that aeolian sands have been transported long distances

(up to hundreds of kilometers) and may then be mixed with several sources within sediment "sinks," such as topographic lows (*Dorn and Day*, 2020).

However, in most cases, visible imagery is insufficient to definitively locate sediment sources for specific observed bedforms. In conjunction with visible imagery, orbital and in situ compositional data can be used to attempt to constrain the source regions of saltating sand. Such studies consistently find that martian dune sand is primarily basaltic (pyroxene-rich and olivine-bearing sands), consistent with the bulk composition of the martian surface, with some broad concentrations of gypsum and other sulfates primarily within the north polar erg (e.g., *Achilles et al.*, 2017; *Chojnacki et al.*, 2014b; *Ehlmann et a*l., 2017; *Fenton et al.*, 2019; *Gendrin et al.*, 2005; *Johnson et al.*, 2017; 2018; *Rampe et al.*, 2018; *Rogers and Aharonson*, 2008; *Sullivan et al.*, 2008). This broad similarity in martian dune sand composition makes it difficult to link aeolian sediments to their potential source, although a few studies have attempted to do this. Based on orbital data, candidate sources for intracrater fields were identified in nearby mafic layers outcropping in crater or valley walls (e.g., *Chojnacki et al.*, 2014b; *Fenton*, 2005; *Lapôtre et al.*, 2017; *Stockstill-Cahill et al.*, 2008; *Tirsch et al.*, 2011) based on the presence of a few minor phases. (Although, in the study by *Fenton* (2005), the grain composition was also traced to other, widespread rocky units in the region, suggesting that sand-bearing layers may have first accumulated through region-wide deposition(s), with numerous local exposures being now exhumed and recycled.) However, both orbital and in situ data have also shown compositional variation within a dune field (e.g., *Chojnacki et al.*, 2014a; *Lapôtre et al.*, 2017; *Pan and Rogers*, 2017; *Seelos et al.*, 2014), suggesting that winds may sort grains by mineralogy, potentially due to correlations between grain composition and phenocryst size, grain density, and shape (*Baratoux et al.*, 2011; *Fedo et al.*, 2015; *Lapôtre et al.*, 2017; *Mangold et al.*, 2011). For example, observations from the *Spirit* rover found that mafic minerals were concentrated in the coarse-grained targets in Gusev crater (e.g., *Morris et al.*, 2006; *Ming et al.*, 2008; *Sullivan et al.*, 2008), and observations from *Curiosity* found Mg, Fe, Ni, and Mn to be enriched in coarser samples (*O'Connell-Cooper et al.*, 2017; 2018) and more crystalline and amorphous ferric materials in finer-grained targets (*Johnson et al.*, 2017; 2018). Such sorting would affect bulk mineral composition measurements and cause significant variation from that of the parent rock after aeolian transport.

Grain composition can also yield information about the general history of sediment on a planetary body and provide clues for a grain's original source region. For example, both orbital and in situ measurements of the dune sand within Gale crater showed that a small (<10%) fraction of sand was composed of X-ray amorphous materials, indicating the presence of weathered silicates and nanophase Fe oxides and sulfates (*Achilles et al.*, 2017; *Ehlmann et al.*, 2017; *Lane and Christensen*, 2013; *Rampe et al.*, 2018). Such materials suggest the grains were weathered through contact with water (*Ehlmann et al.*, 2017). However, without clear knowledge of the source region of the grains, it is difficult to tie their history to the geologic history of a specific site. Additionally, this amorphous component may come from martian dust, which is well mixed globally, reflecting regular global circulation of fine particles (*Berger et al.*, 2015; *Lasue et al.*, 2018). In situ measurements of martian airfall dust by multiple rovers have shown that it is very consistent over the martian surface and is reflective of the global Mars soil unit and its general basaltic crust, but is elevated in S and Cl relative to martian rocks and sand (*Berger et al.*, 2015; *Ehlmann et al.*, 2017; *Lasue et al.*, 2018; *Yen et al.*, 2005).

2.1.3 Bedforms: Types and Morphologies

From orbiter images, aeolian bedforms of meter-wavelength ripples (i.e., just visible at the highest image resolution: Table 1) to kilometers-scale megadunes have been mapped and measured around the globe (e.g., *Bridges et al.*, 2007; *Brothers and Kocurek*, 2018; *Hayward et al.*, 2007; 2014). Rovers have driven through a few centimeters-high to meter-high ripples (e.g., *Curiosity* drove through Dingo gap (*Arvidson et al.*, 2017)) and around the meters-high dunes in Bagnold dune field (*Bridges and Ehlmann*, 2017; *Lapôtre and Rampe*, 2018). In this section, and again when discussing bedform migration (§2.2.2), we discuss five classes of bedforms (their names are underlined) because these are presently proposed to reflect different regimes of aeolian bedform dynamics; however, questions remain about how distinct these bedforms may be.

Sand ripples with decimeter wavelength have been observed by all Mars rovers (Table 2), but are below the image resolution limit of orbital data. (Larger ripples observed by these rovers were recognizable in orbital images, see below.) The *Spirit* rover observed dark decimeter-scale ripples within the El Dorado ripple field (*Sullivan et al.*, 2008), which were some of the first documented to migrate (*Sullivan et al.*, 2008), demonstrating that these were active aeolian bedforms (discussed further in §2.2.2). Within Gale crater, similar ripples with wavelengths of

~5–12 cm, straight crests, and subdued sub-centimeter topography were observed in fine sand (*Ewing et al.*, 2017; *Lapôtre et al.*, 2016; 2018). On Earth, ripples of similar size and morphology (i.e., with straight crests and relatively subdued profiles) are called impact ripples and are created through grain splash (*Bagnold*, 1941; *Rubin*, 2012; *Sharp*, 1963; *Werner et al.*, 1986; *Wilson*, 1972). By analogy, decimeter-scale ripples on Mars have been interpreted as impact ripples—an interpretation also consistent with numerical (*Yizhaq et al.*, 2014) and theoretical modeling (*Andreotti et al.*, 2006; *Duran Vinent et al.*, 2019), predicting impact ripples should have decimeter-scale wavelengths on Mars.

Larger (i.e., meter- to decameter-wavelength) ripples were originally grouped together within the polygenetic class of "mega-ripples," similar to how aeolian ripples on Earth were originally designated by scale and grain size population as smaller unimodal impact ripples and larger bimodal "mega-ripples" (*Bagnold*, 1941; *Sharp*, 1963). However, the martian megaripple class has since been divided into three groups based on observed activity, morphology, albedo, and consistency of grain size within the features. Dark meter-scale ripples are visible in orbital imagery of dune fields and sand sheets, which shows them to be ubiquitous and to migrate over seasonal timescales (§2.2.2) (*Bridges et al.*, 2012a; SOM 3). In addition to being larger than martian impact ripples, these features differ in morphology. For example, their crestline geometry and orientation is highly variable, with dark meter-scale ripples on the gentle stoss of dunes tending to be transverse-to-oblique and highly sinuous, whereas those on steeper slopes have straight linear crests (*Ewing et al.*, 2017; *Lapôtre et al.*, 2016; 2018). Their downwind profiles also vary, from transverse large ripples with asymmetric profiles, gentle stoss slopes, and near-angle of repose lee faces (*Ewing et al.*, 2017; *Lapôtre et al.*, 2016; 2018; *Sullivan et al.*, 2008) to longitudinal large ripples with symmetric profiles (*Lapôtre et al.*, 2018). Furthermore, grainfall and grainflow deposits are observed on the lee of transverse large ripples (*Ewing et al.*, 2017; *Lapôtre et al.*, 2016; 2018), and decimeter-scale impact ripples form concurrently and migrate on the stoss of large ripples (*Ewing et al.*, 2017; *Lapôtre et al.*, 2016; 2018; *Sullivan et al.*, 2008). These bedform wavelengths were found to correlate negatively with elevation on the planet (*Lapôtre et al.*, 2016; *Lorenz et al*., 2014) (discussed again in §7.3).

Two additional classes of meter-scale (and larger) ripples are observed on Mars with coarser grains inferred to occur along the crest and limited observed activity: coarse-grained ripples and transverse aeolian ridges. As with terrestrial mega-ripples, the coarser fraction along the crest has

implications for both the morphology and activity of these bedforms. As coarser elements accumulate near the crests, mega-ripple dimensions (spacing and heights) gradually increase (*Andreotti et al.*, 2002). Mega-ripples on Earth migrate and respond to changes in winds relatively slowly as typical wind stresses are below the threshold to initiate and sustain surface creep of coarser sand (*Bagnold*, 1941; *Lämmel et al.*, 2018). Critically, mega-ripples may need ample saltating sand driven by a formative, preferentially uni-directional wind regime to migrate (e.g., during infrequent storms).

Meter-scale, bimodal coarse-grained ripples (descriptive term employed here without implication of specific modes of transport) were identified during MER traverses at Gusev crater (*Sullivan et al.*, 2008) and Meridiani Planum (*Jerolmack et al.*, 2006; *Sullivan et al.*, 2005). For example, with the active decimeter ripples, ~3 m wavelength and ~30 cm tall dark ripples were observed in the El Dorado ripple field. This location contained both fine- and coarse-grained ripples, and both appeared to be static based on the grain size distribution and lack of sediment mobility, except for dust removal (*Sullivan et al.*, 2008). Coarse-grained ripples have also been observed by the *Curiosity* rover in Gale crater along the trailing edge of Bagnold dune field and outside of the active dune field in isolated sand sheets (Figure 6), with variable crest grain sizes and amount of dust cover (*Lapôtre et al.*, 2018; *Weitz et al.*, 2018). More recently martian "mega-ripples" were interpreted using orbital data due to their greater dimensions (5–20 m spacing, ~1–5 m tall) and brighter crests than typical dark decameter ripples, where the latter was inferred as a coarser grain size component (*Silvestro et al.*, 2020). These intermediate-scale bedforms are typically trailing the stoss side of or flanking dunes, dominantly transverse in morphology, and some were recently reported to be migrating (*Chojnacki et al.*, 2019; *Silvestro et al.*, 2020; SOM 4).

Larger, martian bedforms (10-200 m wavelength, 1-14 m tall) termed transverse aeolian ridges (TARs) were first noted and debated following their discovery in early high-resolution image data (*Bourke et al.*, 2003). TARs tend to have longer, more widely distributed wavelengths and are brighter than the large ripples (*Lapôtre et al.*, 2016), and tend to have more symmetric profiles than most bedforms (*Zimbelman*, 2010). These enigmatic bedforms are concentrated in the martian tropics, appearing in isolated or expansive fields across plains, within craters or canyons, or in association with large dark dunes (*Balme et al.*, 2008; *Berman et al.*, 2011; 2018; *Bourke et al.*, 2003; *Geissler*, 2014; *Geissler and Wilgus*, 2017; *Hugenholtz et al.*,

572 2017; *Wilson and Zimbelman*, 2004; *Zimbelman*, 2010; 2019). TARs are generally thought to
573 form from surface creep of coarse-grained particles (e.g., *Bourke et al.*, 2003; *Hugenholtz et al.*,
574 2017; *Zimbelman*, 2010) or the deposition, induration, and erosion of dominantly dust-sized
575 particles (*Geissler*, 2014). Although initially without a good terrestrial analog, moderate-scale
576 aeolian bedforms (2–250 m wavelength, 1–4 m tall) were recently identified in deserts of Iran
577 and Libya (*Foroutan and Zimbelman*, 2016; *Foroutan et al.*, 2019). It was also recently proposed
578 that *Curiosity* traversed a TAR in Gale crater (*Zimbelman and Foroutan*, 2020).
579 As on the Earth, the largest aeolian bedform class are sand dunes. These features were seen
580 in some of the earliest imagery (*Greeley et al*., 1992; *Masursky*, 1973; *Sagan et al.,* 1972; 1973)
581 and have been mapped globally (*Hayward et al.*, 2007; 2010; 2012; 2014; *Fenton*, 2020). The
582 most extensive coverage of dune sand occurs within the northern circum-polar basins as nearly
583 continuous sand seas (e.g., Olympia Undae) (*Hayward et al.*, 2014; *Lancaster and Greeley*,
584 1990). Impact craters are the most wide-spread locale for dune fields because these serve as a
585 natural sediment sink (*Dorn and Day*, 2020; *Greeley et al.*, 1992; *Hayward et al.*, 2007; 2014;
586 *Roback et al.*, 2020). Other common settings for dune fields are topographic depressions such as
587 troughs, valleys, and chaotic terrain, including the great structural rift system of Valles Marineris
588 (*Chojnacki et al.*, 2014a). Less commonly, extra-crater plains may host dispersed clusters of
589 dunes (*Chojnacki et al.*, 2018; *Fenton*, 2005; *Hayward et al.*, 2007).
590 Specific dune morphologies could be properly classified following the advent of high-
591 resolution image data (*Malin et al.*, 1992; 2007; *McEwen et al.*, 2007) and are sorted using
592 classic terrestrial classifications as defined by *McKee* (1979) (SOM 5). The vast majority of
593 martian dune morphologies occur as crescent-shaped dunes (i.e., barchan, barchanoid) where
594 horns overall point in the downwind direction (e.g., Figures 4, 5), although the occurrence of
595 asymmetric barchans and linear dunes growing through a fingering instability (*Courrech du Pont*
596 *et al.*, 2014) has been recognized on Mars (e.g., *Ewing et al.*, 2017; *Silvestro et al.*, 2016). Other
597 not-uncommon dune types include linear, transverse (e.g., Figure 1), star, sand sheet, and dome
598 dunes (*Davis et al.*, 2020; *Fenton et al.*, 2013; *Hayward et al.*, 2007). Overlapping dunes
599 (compound) and/or combinations of dune morphologies (complex) are also very commonly
600 observed in large dune fields or ergs (*Brothers and Kocurek*, 2018; *Chojnacki et al.*, 2014a;
601 *Fenton et al.*, 2013). Less common classes of topographically related dunes may be found on
602 crater or canyon walls as falling or climbing dunes (*Bourke et al.*, 2004; *Chojnacki et al.*, 2010).

Additional occurrences of dunes possessing unusual morphologies that were not readily classified using terrestrial types were also found (*Hayward et al.*, 2007). For example, "bullseye" dune fields, based on their concentric ring patterns, only occur in high-southern latitude craters and are unreported on Earth (*Fenton and Hayward*, 2010; *Hayward et al.*, 2014). More broadly, sand dune morphology of the high southern latitudes (poleward of 50°S) show well-rounded crests and lee-sides below the angle of repose, likely due to limited aeolian activity and the prominence of ground ice (*Banks et al.*, 2018; *Fenton and Hayward*, 2010). Ultimately, these different dune morphologies form in response to the numerous extraneous environmental factors of Mars (e.g., wind direction and variability, transport capacity, sand supply, topography, seasonal frost/ice) (e.g., *Courrech du Pont et al.*, 2014; *Ewing and Kocurek*, 2010; *Gao et al.*, 2015; *Kocurek and Lancaster*, 1999, *Rubin and Hunter*, 1987). The only ground observations of martian dunes to-date come from *Curiosity*'s investigation of the Bagnold dune field, where barchans migrate along the field's trailing edge, transitioning into barchanoidal ridges and into linear oblique dunes further south towards Aeolis Mons (informally known as Mount Sharp) (*Bridges and Ehlmann*, 2017; *Lapôtre and Rampe*, 2018).

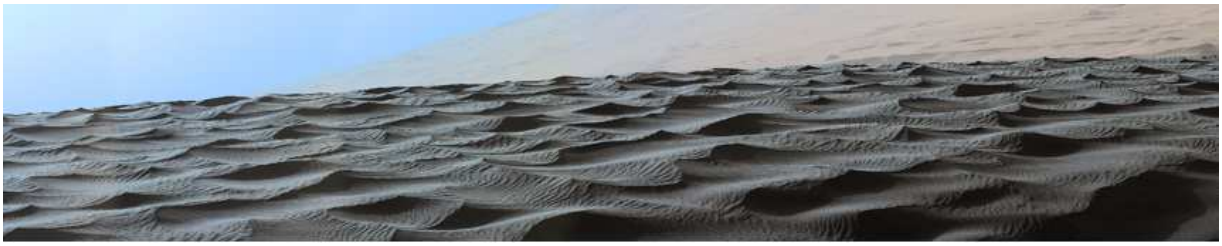

Figure 6. MSL Mastcam image showing two sizes of ripples over the stoss slope of Namib dune, Bagnold dune field. The large ripples have ~2-m wavelength, and the smaller ones have ~10-cm wavelength. Image is NASA photojournal PIA20755, acquired 2015-12-13 on *Curiosity*'s 1192nd sol.

2.2 Aeolian Transport, Fluxes, and Erosion Rates

Knowledge of the minimum wind speed capable of inducing aeolian transport is central in predicting bedform migration rates, resurfacing rates, and dust emissions in ancient and contemporary martian climates (e.g., *Bagnold*, 1941; *Greeley and Iversen*, 1985; *Kok et al.*, 2012; *Sullivan and Kok*, 2017). Winds below the threshold, or minimum wind speed for motion, are not sufficient to mobilize material; thus, determining the minimum wind speed required to initiate motion on the surface of Mars can unlock clues regarding Mars' past climate and weather phenomena. For example, aeolian sedimentary strata reveal the sizes of grains transported under

past climates and directional changes in transport. Such strata are found throughout Mars' landscape giving us hard evidence for how the wind has interacted with the surface, especially when having speeds greater or equal to the threshold for grain motion (e.g., *Banham et al.*, 2018; *Chojnacki et al.*, 2020; *Day et al.*, 2019; *Grotzinger et al.*, 2005; *Milliken et al.*, 2014). By understanding how the threshold of wind-driven grain motion has changed over time as the climate shifted, we can begin mapping aeolian processes throughout Mars' history using the process-based evidence solidified in martian sedimentary strata. We can also use these thresholds to predict contemporary activity on Mars—in particular to forecast surface dust emission rates, which is critical for landed robotic and human exploration.

2.2.1 Thresholds of motion and transport hysteresis

The fluid threshold for wind-blown sand is the minimum shear velocity required to initiate grain movement by the force of the wind alone and was developed to predict dust emission and landform change in sandy environments on Earth (*Bagnold*, 1936; 1937). The Shields-type function is central to most modern threshold equations for Mars and uses shear velocity, a height independent variable that represents the momentum transfer from the boundary layer to the surface, $u_* = \sqrt{\frac{\tau}{\rho}}$ (in m/s; where τ is stress in Pa, ρ is density in kg/m^3), to predict the onset of motion:

$$u_{*t} = A\sqrt{\left(\frac{\rho_s - \rho}{\rho}\right) g d} \quad \text{(Eqn 1)}$$

where u_{*t} is the threshold shear velocity (m/s), ρ_s and ρ are sediment and fluid densities (kg/m^3), g is gravitational acceleration (m/s^2), d is grain size (m), and A is an empirically derived constant (equal to square root of the Shields criterion) that includes a dependence on particle Reynolds number at threshold conditions, $Re_{pt} = \frac{u*\mathrm{d}}{\nu}$, where $\nu = \frac{\mu}{\rho}$ is the kinematic viscosity of the winds (m^2/s), with μ as their dynamic viscosity (Pa·s). The first threshold models for Mars resolved estimates of the A parameter based on wind tunnel experiments in the Planetary Aeolian Laboratory's MARtian Surface WInd Tunnel (MARSWIT) at NASA's Ames Research Center (*Greeley et al.*, 1976; 1980; *Iversen and White*, 1982): the threshold was reached when "…saltation (along the entire wind tunnel) test bed was initiated (following *Bagnold* (1941))" (*Greeley et al.*, 1976, p. 418). Observations of u_{*t} were used to back out detailed models for estimating the A parameter using Re_{pt}, resulting in three conditional models:

663 $$A = 0.2\sqrt{\frac{\left(1+\frac{0.006}{\rho_s g d^{2.5}}\right)}{1+2.5Re_{pt}}}\ for\ 0.03 \leq Re_{pt} \leq 0.3$$ (Eqn 2)

664 $$A = 0.129\sqrt{\frac{\left(1+\frac{0.006}{\rho_s g d^{2.5}}\right)}{1.928Re_{pt}^{0.092}-1}}\ for\ 0.3 \leq Re_{pt} \leq 10$$ (Eqn 3)

665 $$A = 0.120\sqrt{(1+0.006/\rho_s g d^{2.5})}\{1-0.0858\ exp[-0.0671(Re_{pt}-10)]\}\ for\ Re_{pt} \geq$$

666 10 (Eqn 4).

667 These original models predicted the minimum shear velocity required to mobilize sand as well as
668 the optimum grain size for windblown transport over a range of atmospheric densities (Figure 7).
669 Yet, these equations predict threshold winds speeds higher than those modelled or measured at
670 the surface of on Mars (e.g., *Gomez-Elvira et al.*, 2014; *Lorenz*, 1996; *Newman et al.*, 2017) and
671 leading to a discrepancy between lower than threshold martian wind speeds and active sediment
672 transport observed from orbital imagery and landers on Mars.
673

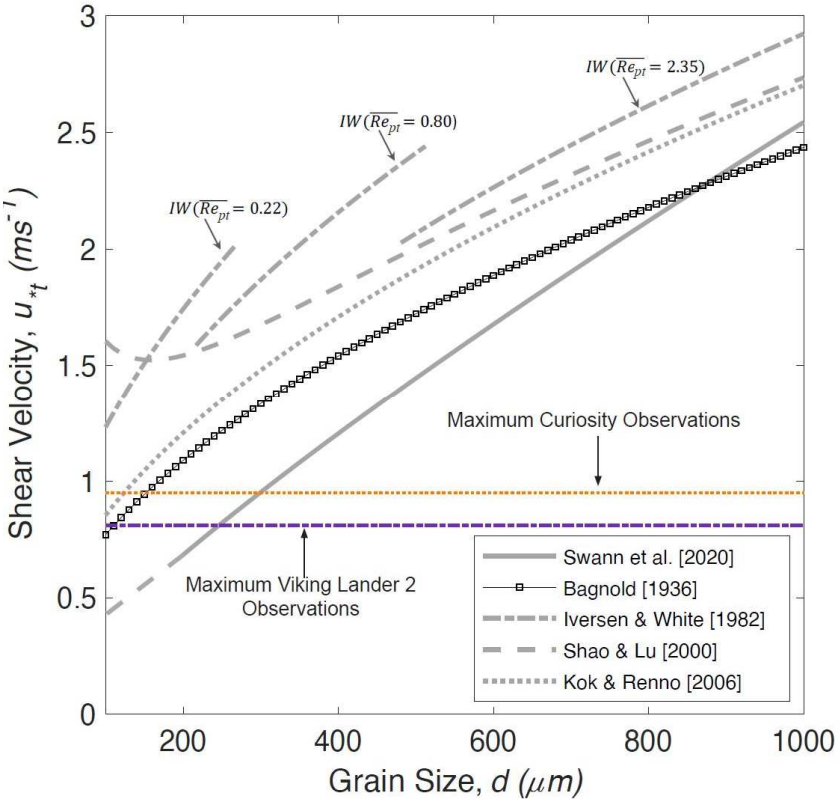

Figure 7. Plot showing different Martian threshold models for sediment transport, along with estimated shear velocities from *Curiosity* and Viking Lander 2. 'IW' refers to the Iversen and White (1982) model, estimated using specified values of Re_{pt}.

Two reasons for this discrepancy are *(1)* the experimental criterion used to define the threshold and *(2)* the absence of a complete dimensional transformation of their empirical data (*Swann et al.*, 2020). Defining the threshold as the onset of continuous motion over the test bed, a common practice on Earth, disregards intermittent sporadic motion that occurs at slower shear velocities. In particular, this definition disregards the ability for a small burst of sand grains to induce equilibrium transport downwind through impact cascades (*Bauer et al.*, 2009; *Sullivan and Kok*, 2017). Through a set of numerical experiments, *Sullivan and Kok* (2017) determined that, on Mars, cascading saltation can lead to continuous saltation but over distances much longer than available in laboratories. This finding is highly significant for martian aeolian processes. High-frequency turbulent fluctuations that momentarily exceed the threshold for motion can induce transport of a small patch of grains that, downwind, can become equilibrium transport. The concept is hinged on a lower, impact threshold, u_{*it}. The impact threshold occurs at slower shear velocities because the momentum transferred to particles at rest is a function of the wind and the impact of saltating grains. Thus, the momentum from the wind does not need to be as

great in order to sustain motion because the impact of saltating grains dislodges particles at rest. On Earth, the impact threshold is approximately 80% of the fluid threshold, but on Mars it is predicted to be as low as 10–20% of the fluid threshold due to the much lower atmospheric density (*Kok*, 2010). Thus, once particles are mobilized, wind speed has to drop significantly in order for particle motion to cease.

In light of these findings, new experimental observations were recently conducted in the MARSWIT to resolve the threshold at the onset of cascading saltation of sand-sized particles (*Burr et al.,* 2020: 150–1000 μm; *Swann et al.*, 2020: 200–800 μm). Incrementally increasing the speed over a bed of particles at rest, these studies dimensionally transformed wind tunnel observations from a set of vertically stacked pitot tubes to calculate shear velocities corresponding to discontinuous, sporadic motion; here, we report primarily on the results from *Swann et al.* (2020). These shear velocities were used to resolve Bagnold's *A* parameter for cascading motion from Equation (1):

$$A_{Fluid} = 0.0502\, D_*^{0.3157} \quad \text{(Eqn 5)}$$

$$A_{General} = 0.0646\, D_*^{0.2426} \quad \text{(Eqn 6)}$$

where

$$D_* = d\left(\frac{\rho(\rho_s-\rho)}{\mu^2}\right)^{\frac{1}{3}} \quad \text{(Eqn 7).}$$

The new model predicts threshold shear velocities that are slower than previous models by a factor of 1.6 to 2.5. In their model, for a surface with an average grain size of 200 μm, the minimum shear velocity required to initiate cascading motion ranges from 0.63 to 0.81 m/s at atmospheric densities between 0.013 to 0.025 kg/m^3, reconciling theory with measured wind speeds (Figure 7). However, their model is only valid for particles ranging from 200 to 800 μm, excluding values for finer particles where interparticle cohesion increases the threshold for motion (*Bagnold*, 1937; *Iversen and White*, 1982; *Shao and Lu*, 2000). The transition from cohesion-dominated to gravity-dominated threshold is represented by a marked upturn, or inflection, in threshold curves where forces required to initiate motion increase due to an increase in interparticle attractive forces between finer particles (Figure 7). Predicting the inflection point in the threshold curve determines the optimum grain size (i.e. the easiest particles to move by the force of the wind) and represents the most commonly mobilized particles. Early workers estimated that this inflection point should lie between 100 and 200 μm(*Bagnold*, 1937;

Iversen and White, 1982; *Shao and Lu*, 2000); this prediction is consistent with *Curiosity*'s observations of well sorted, unimodally distributed 100–150 μm sand in the active Bagnold dune field (e.g., *Weitz et al.*, 2020).

2.2.2 Bedform migration and evolution

Bedforms, from small impact ripples up through mature dunes, have been observed to migrate in a range of locations on Mars. These migration rates and the scale of the bedforms indicate variable sediment flux rates, which are typically an order of magnitude lower than terrestrial rates (*Bridges et al.*, 2012b; *Chojnacki et al.*, 2019).

Small ripples with decimeter wavelength have been observed to migrate short distances over a few sols around Mars rovers during windy seasons (i.e., southern summer (*Ayoub et al.*, 2014; *Baker et al.*, 2018b)). For example, poorly sorted <300-μm sand at El Dorado were observed to migrate about 2 cm over 5 sols (*Sullivan et al.*, 2008), and small ripples in fine sand were observed to migrate by up to 2.8 cm/sol in sand patches at Gale crater (*Baker et al.*, 2018b). Assuming activity during half of the martian year, extrapolated migration rates range from 10 cm to 10 m per martian year (*Baker et al.*, 2018b).

Migration of dark meter-scale ripples, ubiquitous in association with dark dunes (*Bridges et al.*, 2007), has been observed in high-resolution repeat orbital images (e.g., SOM 3). In these images, ripple displacements can be measured manually or in aggregate for larger areas using the Co-registration of Optically Sensed Images and Correlation (COSI-Corr) methodology (*Bridges et al.,* 2013; *Leprince et al.*, 2007). The first unambiguous meter-scale modification of ripples and dune edges was documented in Nili Patera (*Silvestro et al.*, 2010), where superposed decimeter-tall ripples (*Ewing et al.*, 2017; *Lapôtre et al.*, 2018) may migrate up to several meters per year, but average ~0.5 m/yr from larger sampling (*Ayoub et al.,* 2014; *Bridges et al.*, 2012a; *Chojnacki et al.,* 2018; *Preston and Chojnacki*, 2019; *Runyon et al.*, 2017; *Silvestro et al.*, 2013). Ripples are swiftest mid-way up a dune's stoss slope through the dune crest: ~5x faster than ripples at the base of the stoss or in the lee or flanks areas (*Bridges et al.*, 2012a; *Preston and Chojnacki*, 2019; *Roback et al.*, 2019; *Runyon et al.*, 2017). In general a linear relationship between ripple migration rate and ripple elevation on the dune has been demonstrated (*Bridges et al.*, 2012a; *Runyon et al.*, 2017), likely due to streamline compression from dune topography as winds are pushed upslope. Isolated ripple patches not associated with a dune field have the lowest migration rates; such rates are detected using image pairs spanning two or more martian

755 years. These measurements reflect sand flux rates between 0.1–2.3 $m^3 m^{-1} yr^{-1}$, which are
756 typically several factors less than the saltation rate suggested by the migration rate of
757 neighboring dunes (*Ayoub et al.*, 2014; *Bridges et al.*, 2012b; *Roback et al.*, 2019; *Runyon et al.*,
758 2017; *Silvestro et al.*, 2013). Saltation rates also appear higher during the northern hemisphere
759 autumn/winter, which is also when driving winds are likely greatest (*Ayoub et al.*, 2014; *Roback*
760 *et al.*, 2019).
761 The first clear observation of bedform change from orbital data was the gradual
762 disappearance of two small (~1000 m^2) north polar dome dunes and ~85% deflation of a third
763 over a five-year time span (1999–2004) in MOC images (*Bourke et al.*, 2008). Since then,
764 several studies have used various combinations of HiRISE pairs and topography to estimate
765 migration rates and sand fluxes for dunes (*Ayoub et al.*, 2014; *Bridges et al.*, 2012a; 2012b;
766 *Cardinale et al.*, 2020; *Chojnacki et al.*, 2015; 2017; 2018; *Hansen et al.*, 2011; *Runyon et al.*,
767 2017; *Silvestro et al.*, 2013; Figure 8; SOM 2–4, 6). Reported average migration rates are
768 consistently ~0.5 m/yr (±0.4 m/yr, 1σ) for dunes that are ~2–120-m tall (average height 19±14
769 m) (*Chojnacki et al.*, 2019). These reported rates are typically for barchan or barchanoid dune
770 morphologies in uni-directional wind regimes (e.g., SOM 6), but include some instances of
771 linear, dome, and falling dunes. Average crest flux measurements for dune fields ranged between
772 1–18 $m^3 m^{-1} yr^{-1}$ (average across q_{crest} = 7.8±6.4 (1σ) $m^3 m^{-1} yr^{-1}$), where the maximum flux for an
773 individual dune was 35 $m^3 m^{-1} yr^{-1}$ (*Chojnacki et al.*, 2019). These rates and fluxes are relatively
774 variable in terms of geography and timing. For example, the highest sand fluxes documented to
775 date appear to concentrate in three regions: Syrtis Major, Hellespontus Montes, and the north
776 polar erg (*Chojnacki et al.*, 2019). Poleward of 45° S, dunes sites show limited bedform
777 mobility, and southward of 57° S only ripple migration has been detected (i.e., no bulk dune
778 movement) (*Banks et al.*, 2018). Dunes surrounding the north polar layered deposits and residual
779 cap display the greatest migration rates and fluxes: ~50% greater than on average for Mars (11.4
780 vs. 7.8 $m^3 m^{-1} yr^{-1}$) (*Chojnacki et al.*, 2019). These higher values are found in the polar regions
781 despite the limited sediment state caused by autumn/winter CO_2/H_2O ice accumulation that
782 reduces surface interactions with the wind (*Diniega et al.*, 2019a; *Hansen et al.*, 2011; 2015).
783

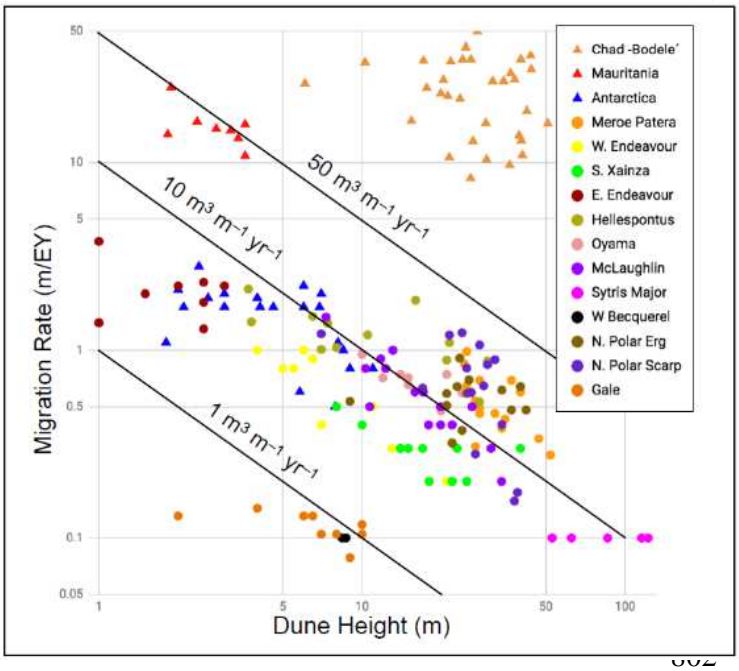

Figure 8. Log-log plot of dune migration rates vs. dune heights for select martian and terrestrial dune fields. Dune rates are averages per site using the longest-baseline HiRISE orthoimages available. Migration rate confidence intervals are typically ±0.1–0.3 m/yr and account for orthoimage registration offsets and human error in manual measurements. The "terrestrial" estimates are from dune field data collected in Chad, Mauritania, and Antarctica (*Bourke et al.*, 2009; *Ould Ahmedou et al.*, 2007; *Vermeesch and Drake*, 2008). Mars dune flux estimates are from earlier work by *Chojnacki et al.* (2017; 2018; 2019).

Aside from many ripples within the southern dune fields, many smaller martian bedforms show no sign of present-day migration; such features may also have superposed craters, debris, and fracturing that indicate a long-term lack of migration and renewal. In particular, with a few newly identified exceptions (*Silvestro et al.*, 2020), TARs appear to be inactive based on morphology and context (*Berman et al.,* 2018). For example, crater age dating indicates certain TAR fields in Schiaparelli crater have been inactive for the last ~100 kyr to ~2 Myr, suggesting that they are relict deposits (*Berman et al.*, 2018). Numerous authors investigating dark ripples or dunes via comparison of HiRISE image pairs have reported on the lack of apparent motion for nearby TARs. However, efforts just may not have used sufficiently long temporal baselines; for example, these investigations typically used images spanning 2–3 martian years for a survey of low sand flux regions (e.g., Valles Marineris, Meridiani) or dune migration (*Banks et al.*, 2015; *Berman et al.*, 2018; *Bridges et al.*, 2012a; *Chojnacki et al.*, 2014a; 2017; *Geissler et al.*, 2012). Using longer baseline images (>4 martian years) and targeting known high flux dunes within McLaughlin crater, several bright-toned TAR-like bedforms showed unambiguous crest displacements *(Silvestro et al.*, 2020). It may be that certain TAR populations within high flux sand corridors are subjected to enough repeated saltation to dislodge their presumably coarser-grained crest areas. Preliminary results suggest mega-ripple and TARs that are migrating today

are doing so with rates and fluxes an order of magnitude lower than those estimated for adjacent sand dunes (*Silvestro et al.*, 2020; SOM 4).

2.2.3 Erosion Rates

We focus here on bulk surface erosion rates that are likely to be primarily driven by aeolian erosion (versus mass wasting, which is discussed in §3, 5), predominantly via sand abrasion (*Laity and Bridges*, 2009). Bulk surface erosion rates have generally been estimated based on the existence, age, and geomorphology of various crater populations along with geologic setting. For example, locations in Gusev crater showed in situ and orbital estimates of 10^{-3}–10^{-5} m/Myr (note that m/Myr is equivalent to μm/yr) (*Golombek et al.*, 2006) and rates of 10^{-2}–10^{-3} m/Myr were estimated for Elysium Planitia based on crater depth degradation and rim erosion (*Sweeney et al.*, 2018). Based on deviations in small-crater counts from expected isochrones, the crater obliteration rate for light-toned sedimentary rocks suggests an average erosion rate of 10^{-1} m/Myr (*Kite and Mayer*, 2017). Younger terrain in Meridiani Planum yielded higher rates 1–10 m/Myr (*Golombek et al.*, 2014), which may be more similar to wind-driven scarp retreat in Gale crater, as suggested by radiogenic and cosmogenic dating of exposed sediments within Aeolis Mons (*Farley et al.*, 2014). (As noted in those studies, terrestrial continental denudation rates for arid regions are still a few (2–5) orders of magnitude higher.)

To quantitatively connect surface abrasion rates to aeolian sand flux rates, the total sand flux (i.e., saltation plus reptation) is needed. This can be estimated from the dune crest fluxes and making some assumptions about the mass loss from impacting sand on the target material. For basalt sand grains hitting basaltic rocks at the impact threshold for Mars, this value of abrasion susceptibility is ~2×10^{-6}, based on laboratory measurements (*Greeley et al.*, 1982) and accounting for the energetics of martian saltation and reptation (*Bridges et al.*, 2012b). Taking the estimated saltation and reptation trajectories for Mars of 0.1–0.5 m (*Kok*, 2010) and interdune sand fluxes, abrasion rates for a range of sloping surfaces (i.e., flat ground to a vertical rock face) can be approximated (a detailed methodology for doing this is explained in *Bridges et al.* (2012b)). Abrasion rates for several sites have been reported (e.g., Nili Patera, Gale crater, Mawrth Vallis, Jezero crater) and range 0.01–1.3 m/Myr for flat ground and 0.3–47 m/Myr for vertical rock faces (*Bridges et al.*, 2012b; *Chojnacki et al.*, 2018; *Farley et al.*, 2014).

2.3 Open questions for martian aeolian landforms and sediment history

Major questions remain open about the age, sources, and amounts of dust and sand on Mars. The few areas where dune sand is traced back to a source involve eroding crater walls or polar layered deposits, where sand appears to be recycled from sandstone or an ancient erg, respectively (e.g., *Chojnacki et al.*, 2014b; *Tirsch et al.,* 2011). On Earth, most sand grains form from chemical and physical erosion of quartz down to a stable grain size (*Krinsley and Smalley*, 1972); Mars instead is predominantly basaltic (*Ehlmann et al.*, 2017; *Greeley and Iverson*, 1985; *Minitti et al.*, 2013; *Yen et al.*, 2005). Models predict that sand-sized grains could be created through explosive volcanic processes (*Edgett and Lancaster*, 1993; *Wilson and Head*, 1994), but the most recent volcanism occurred 2–10 Mya (e.g., *Neukum et al.,* 2004b). Others have proposed that sand grains may form by fragmentation driven by impact and aeolian processes (*Golombek et al.*, 2018; *McGlynn et al.*, 2011). Some have proposed that the general generation and flux of granular material on Mars has declined over time, with the impact, volcanic and chemical weathering processes on an ancient, wet Mars generating the majority of sediment (*Grotzinger and Milliken*, 2012; *McLennan et al.*, 2019). However, it is not currently known if most martian sand has been recycled or if a significant amount is actively forming in the present climate.

Similar questions can be asked about dust. The global dust budget and surface reservoir distribution, as well as the dust lofting rate, present important controls on climate models. It is important to understand not only the present state, but also how dust availability and distribution may have changed through climate cycles (i.e., thousands to millions of years) and climate epochs (i.e., to billions of years).

Observations of a few dune fields suggest that sand is size and compositionally sorted (e.g., *Chojnacki et al.*, 2014b; *Lapôtre et al.*, 2017; *Pan and Rogers*, 2017; *Seelos et al.*, 2014) as it progresses through a transport pathway and aeolian bedforms. Such observations present an interesting feedback question, as grain size can influence evolution/mobility of the bedforms and further grain transport. This also suggests that additional complexity may be needed in models connecting landform morphology to formation history.

Although hypotheses for the growth-limiting mechanism of meter-scale ripples are converging towards an aerodynamic process (e.g., *Duran Vinent et al.*, 2019; *Lapôtre et al.*, 2016; 2021; *Sullivan et al.*, 2020) the nature of their inception mechanism is still being debated

(*Duran Vinent et al.*, 2019; *Sullivan et al.*, 2020). Questions about present-day activity rates (if nonzero) and formative history of such features, and why this diversity of bedforms is found, remain an open area of study. While these questions are about the evolution of landforms, such models are built from sediment flux and saltation layer models, which in turn depend on models of how individual grains are moved along the surface (e.g., the fractional contributions of saltation versus reptation to a wind-driven sand flux)—discussed more in §2.4.

2.4 Open questions for the physics of aeolian processes

Regarding the fundamental physics of aeolian grain transport, terrestrial and laboratory studies form the basis of the majority of information known about the influence of different parameters (summarized in *Pahtz et al.*, 2020). In application of these models towards the martian environment, current threshold models predict minimum wind speeds that align with observed wind speeds on Mars (*Burr et al.*, 2020; *Kok et al.*, 2012; *Swann et al.*, 2020). However, a number of uncertainties in the application of thresholds to natural boundary layers acting over spatially heterogeneous surfaces and bedforms on Mars remain, including: *(1)* the use of idealized surface conditions for threshold model derivation, *(2)* the difficulty in obtaining necessary parameters such as grain size, shape and density on Mars, and *(3)* potential errors in estimating shear velocity from single-height wind speed observations.

Empirical coefficients in Martian threshold models are derived for idealized surface conditions, saltating particles moving over flat beds of cohesionless grains with uniform size distributions. These do not represent the more complex surfaces and bedforms found on Mars, e.g., stoss slopes of dunes, mixed grain size surfaces and bedforms, and coarse-lag deposits. Surfaces and bedforms with mixed grain size distributions, sediment consolidation levels, or coarse lag deposits can act to increase the minimum wind speed required to initiate saltation or become active by a different mode of transport (e.g., saltation vs. rolling particles or reptation).

Uncertainty in threshold predictions also arises from the difficulty in determining grain size, shape, and density comprising aeolian bedforms on Mars. In situ observations from landers and rovers have been successful at determining these characteristics. For example, *Curiosity*'s Mars Hand Lens Imager (MAHLI) determined particle sizes and shapes within ripples throughout Gale crater (*Weitz et al.*, 2018). However, these observations are geographically limited and remote sensing techniques do not have the resolution required to determine grain size and density that are required to predict the threshold for motion.

914 Finally, there is uncertainty in estimating shear stress, or shear velocity, on the surface of
915 Mars. Shear velocity, a surrogate for bed shear stress, can be estimated from single-height wind
916 speed observations using either the covariance of 2D or 3D velocity components or von
917 Karman's Law of the Wall. However, local thermal convection at the surface on Mars induces a
918 dynamically unstable boundary layer (*Fenton and Michaels*, 2010). The instability in the
919 boundary layer, represented by deviations from typical logarithmically distributed velocity
920 fluctuations, is difficult to predict. At present, wind speeds on Mars are observed at a single
921 height (typically ~1.5 m above the surface) and sampled at low frequencies. Thus, we have yet to
922 measure how the boundary layer responds to variations in local convection, or estimate the error
923 associated in low-frequency sampling that can alias shear velocity calculations, in particular
924 when using the covariance derivation. In situ measurements of vertical velocity gradients within
925 unstable boundary layers at the surface of Mars are necessary to reduce error in shear velocity
926 estimation.
927 Unfortunately, testing different sediment transport processes further is not possible with
928 existing rover payloads or from orbit. Additionally, it is difficult to mimic martian conditions,
929 especially over sufficient distances to allow full formation of the saltation layer, within present
930 terrestrial laboratories. As will be discussed in §6, in situ investigations are needed to acquire the
931 high-frequency, high-resolution measurements that can correlate driving environmental
932 conditions (such as wind velocities, including gusts, and surface pressure) with the sediment
933 movement.
934
935 # 3 Seasonal Frost/Ice-formed Landforms
936 The martian atmosphere is ~95% CO_2 and contains trace amounts of water vapor (e.g., on the
937 order of a few tens of precipitable microns). Under typical present-day martian surface
938 conditions, CO_2 and H_2O condenses near ~145 K and ~198 K, respectively (*Ingersoll*, 1970;
939 *James et al.*, 1992). Frost condensation temperatures are reached at virtually all latitudes
940 (*Piqueux et al.*, 2016), although, as on Earth, the exact duration of the period when the
941 environment is sufficiently cold for frost or ice to accumulate (e.g., seconds, to seasons, to
942 astronomical cycles) depends on latitude and local surface and subsurface conditions (e.g., grain
943 size and composition, subsurface water ice content and depth) that influence the local thermal
944 inertia, shadowing due to topography, and atmospheric conditions such as dust opacity (*Putzig*
945 *and Mellon*, 2007).

In this section, we describe the frost and ice types that currently form on the martian surface (§3.1). Sublimation of this diurnal (i.e., only overnight) or seasonal frost/ice is highly energetic and is thought to cause erosion by inducing and enhancing mass wasting (§3.2) or by digging/scouring out material from the surface directly under a subliming ice slab (§3.3).

3.1 Currently formed surface frost/ice types on Mars

Present-day CO_2 and H_2O deposition can be in the form of diurnal frosts, seasonal frosts, or snowfall. As the amount of precipitable water is so limited in the tenuous martian atmosphere, water frost/ice condensation will depend on the local partial pressure of water vapor. In contrast, CO_2 ice requires significantly lower temperatures to condense out of the atmosphere, but it is more abundant than water and thus is not limited by diffusion through the lower atmosphere. Tens to hundreds of micrometer thick diurnal CO_2 frost layers form overnight over a significant fraction of the planet (*Piqueux et al.*, 2016). During current martian winters, as much as a third of atmospheric CO_2 can be deposited onto the surface (*James et al.*, 1992; *Leighton and Murray*, 1966) dramatically redistributing CO_2 and decreasing surface pressures. Accumulated decimeters or thicker depth layers of seasonal CO_2 frost will sinter, forming polycrystalline CO_2 slab ice(s) (*Matsuo and Heki*, 2009) with optical and thermal properties very different from terrestrial water frost and ice. In particular, CO_2 ice is transparent to visible wavelengths but opaque to thermal infrared (*Matsuo and Heki*, 2009). As the surface warms moving towards spring, the accumulated CO_2 and H_2O frost/ice will sublime, but not uniformly. Visible solar radiation can penetrate the CO_2 ice layer and, via a process known as the solid state greenhouse effect (*Matson and Brown*, 1989) because it is analogous to the greenhouse effect in planetary atmospheres but happens in a transparent solid body instead of a gaseous atmosphere, lead to the springtime insolation-induced basal sublimation of the translucent, impermeable slab ice (*Kieffer et al.*, 2006). Defrosting marks will appear first, readily visible in high-resolution images, such as sublimation spots, fans, and dark linear 'flow' features (*Gardin et al.*, 2010; *Kaufmann and Hagermann*, 2017; *Kieffer*, 2007; *Malin and Edgett*, 2001; *Pilorget et al.*, 2011; 2013) and polygonal fracturing of the ice slab (*Piqueux and Christensen*, 2008; *Portyankina et al.*, 2012). In general, sublimation can be very energetic and is thought to be a key driver for the formation of many landforms (as described below). Seasonal frosts and snowfall events have some interannual variability in terms of location and duration, which have begun to be documented in

977 a systematic manner as more complete records of the present-day climate and weather are
978 acquired (*Calvin et al.*, 2015; *Hayne et al.*, 2016; *Piqueux et al.*, 2015b; *Widmer et al.*, 2020).
979 To date, the majority of present-day surface activity connected to surface frost/ice has been
980 hypothesized to be controlled primarily by the deposition and/or sublimation of seasonal CO_2
981 frost/ice. The seasonal frost cap begins to form early in the martian fall, reaches maximal extent
982 (i.e., equatorward reach) at the end of the fall, and sublimes between the end of the winter and
983 into the spring (*Piqueux et al.*, 2015b). CO_2 snowfall is observed to contribute to the seasonal
984 frost accumulation (*Gary-Bicas et al.*, 2020; *Hayne et al.*, 2012; 2014). Seasonal ice sheets reach
985 up to ~2 m in thickness near the poles (*D.E. Smith et al.*, 2001) and fractured ice layers and
986 detached ice blocks have been observed in the mid-latitudes (e.g., *Dundas et al.*, 2012). From
987 orbital observations, patchy seasonal surface deposits of CO_2 frost have been observed as far
988 equatorward as ~42° N (*Widmer et al.*, 2020) and 33° S *(Schorghofer and Edget*t, 2006;
989 *Vincedon et al.*, 2010a). In the north, which is the hemisphere with more water in its polar cap
990 (*Ojha et al.*, 2019) and atmosphere (*M.D. Smith*, 2002), a ring of water ice is annually observed
991 equatorward of the CO_2 seasonal frost cap (*Appéré et al.*, 2011; *Langevin et al.*, 2005; 2007;
992 *Wagstaff et al.*, 2008). H_2O frost has been detected from orbit as far equatorward as 32° N and
993 13° S (*Vincendon et al.*, 2010b), while in situ observations suggest H_2O frost at 48° N with the
994 *Viking 2* lander (*Hart and Jakosky*, 1986; *Svitek and Murray*, 1990; *Wall*, 1981), at 2° S with the
995 MER *Opportunity* (*Landis*, 2007), and at 5° S with *Curiosity* at Gale crater (*Martinez et al.*,
996 2017).
997 Although not yet well characterized through observations or models, it is likely that H_2O and
998 CO_2 frost/ices do not form and evolve independently of each other and that their interplay, and
999 interaction with incorporated atmospheric dust, constitutes an additional control on
1000 geomorphological activity that is not yet well understood. For example, CO_2 ice can serve as a
1001 sink for water vapor (*Houben*, 1997; *Houben et al.*, 1997), and H_2O deposits affect basal
1002 sublimation of CO_2 (*Titus et al.*, 2020). In addition to influencing accumulation and sublimation
1003 timing and rates, mechanical interactions between different types of frost/ice may create another
1004 control on some geomorphological activity. For example, differences in grain sizes between a
1005 surface condensed frost layer and snowfall may enhance wintertime mass-wasting activity
1006 (*Hansen et al.*, 2018; §3.2.2).

Over recent Mars history, Mars' obliquity shifts have also affected the spatial distribution and stability of accumulated seasonal frost/ice. Past multi-annual (up to tens of thousands of years) accumulation of CO_2 ice has formed up to ~1 km thick units within the polar regions (*Phillips et al.*, 2011); similarly, over long periods of time, fluxes of water through the atmosphere can result in the formation of large reservoirs at the poles (*Bierson et al.*, 2016; *Buhler et al.*, 2020; *Manning et al.*, 2019), as well as within middle and equatorial latitudes (*Jakosky et al.*, 2005; *Mellon et al.*, 2004; *Mellon and Jakosky*, 1993; 1995; *Mellon et al.*, 1997). As the orbital parameters change, these water ice reservoirs can become unstable. Landforms created through present-day or recent sublimation of such ice reservoirs are discussed in §4, and study of these units, coupled with studies of present-day frost/ice driven surface activity, is necessary to extend models to past climatic periods and interpret relict landforms (§7.3). (However, discussion of the past formation and preservation of such perennial ices is outside the scope of this review.)

3.2 Seasonal sublimation triggered mass-wasting landforms

3.2.1 Gullies

Based on morphological similarity to terrestrial gullies (i.e., comprising alcove, channel, and apron features), martian gullies were initially hypothesized to be formed through liquid water flow, perhaps through groundwater seepage (*Malin and Edgett*, 2000), but a source for the water was not apparent. Early MOC observations showed signs of defrosting activity in south polar gullies (*Bridges et al.*, 2001; *Hoffman*, 2002) but did not document any significant changes to the frost-free surface. *Malin et al.* (2006) provided the first detailed description of contemporary gully activity, reporting two new digitate light-toned deposits in southern-hemisphere craters. Both deposits were associated with poorly developed gullies and were relatively superficial. *Malin et al.* (2006) suggested that these flows indicated discharge of shallow groundwater, but *Pelletier et al.* (2008) modeled one of the deposits in detail and found that it could be explained by dry granular flow. *Kolb et al.* (2010) carried out similar modeling of additional light-toned deposits without constrained formation ages and found that they too could be reproduced by dry flows.

Subsequent detections of more active flows in gullies along both crater walls and dune slopes (e.g., Figures 4, 9) have led to better constraints on the processes causing activity. *Harrison et al.* (2009), *Diniega et al.* (2010), and *Dundas et al.* (2010) all examined active gullies and reported

1039 weak seasonal constraints favoring cold-season activity for gullies on both sand dunes and other
1040 surfaces. *Harrison et al.* (2009) favored seasonal occurrence of liquid water based on
1041 geomorphological similarities to terrestrial debris flows, while *Diniega et al.* (2010) and *Dundas*
1042 *et al.* (2010) proposed that winter CO_2 frost was driving activity in some fashion. The latter
1043 option was strongly supported when *Dundas et al.* (2012) reported active flows with much
1044 tighter timing constraints that correlated well with observed CO_2 frost, including observations of
1045 creeping flows slowly advancing down frosted channels over a period of weeks, as well as one-
1046 off events producing larger morphologic changes. Expanded observations with more locations
1047 are consistent with these behaviors (*Dundas et al.*, 2015a; 2019a), as is a detailed study of gullies
1048 in a pit near the south pole (*Raack et al.*, 2015; 2020). Morphological changes in gullies can be
1049 extensive (*Dundas et al.*, 2012; 2015a; 2019a).
1050 Gullies located on sand dunes with classic alcove-channel-apron morphology appear to be
1051 more active and have even larger morphological changes, possibly because of the loose substrate
1052 (*Diniega et al.*, 2010; *Dundas et al*., 2012; 2015a; 2019a). These features have been found on
1053 sand dunes through the southern mid-latitudes, many with extensive annual activity (*Dundas et*
1054 *al.*, 2019a). *Pasquon et al.* (2019a; 2019b) documented several styles of CO_2-frost driven activity
1055 that drove changes in channel sinuosity, noting an initial alcove-collapse stage followed by
1056 transport into the lower parts of the gullies.
1057 The details of the processes by which CO_2 frost causes gully activity on rocky or sandy
1058 slopes are not yet well understood. Starting shortly after the discovery of gullies, several frost-
1059 driven processes were proposed. *Hoffman* (2002) suggested gas-lubricated flows initially
1060 triggered by basal sublimation of translucent CO_2 frost and further mobilized by additional
1061 sublimation during transport. *Ishii and Sasaki* (2004) proposed that avalanches of CO_2 frost
1062 could occur, while *Hugenholtz* (2008) suggested that frosted granular flow could operate in
1063 gullies. In the latter process, coatings of frost help to lubricate flow. *Cedillo-Flores et al.* (2011)
1064 showed that sublimating CO_2 frost could effectively fluidize overlying granular material but did
1065 not provide a mechanism for how such frost would be emplaced under regolith. *Pilorget and*
1066 *Forget* (2016) demonstrated that basal sublimation would be effective at generating gas eruptions
1067 in some gullies, and also that CO_2 ice could condense in the regolith pore space under some
1068 conditions, but did not explain the formation of channel morphologies (that study specifically
1069 focused on new channels forming amongst linear gullies (§3.3.1)). *Dundas et al.* (2019a) carried

1070 out calculations that showed the available energy budget was sufficient to generate gas from
1071 entrained CO_2 frost during the flow, providing fluidization, and *de Haas et al.* (2019) provided a
1072 more detailed description of the relevant physics.
1073

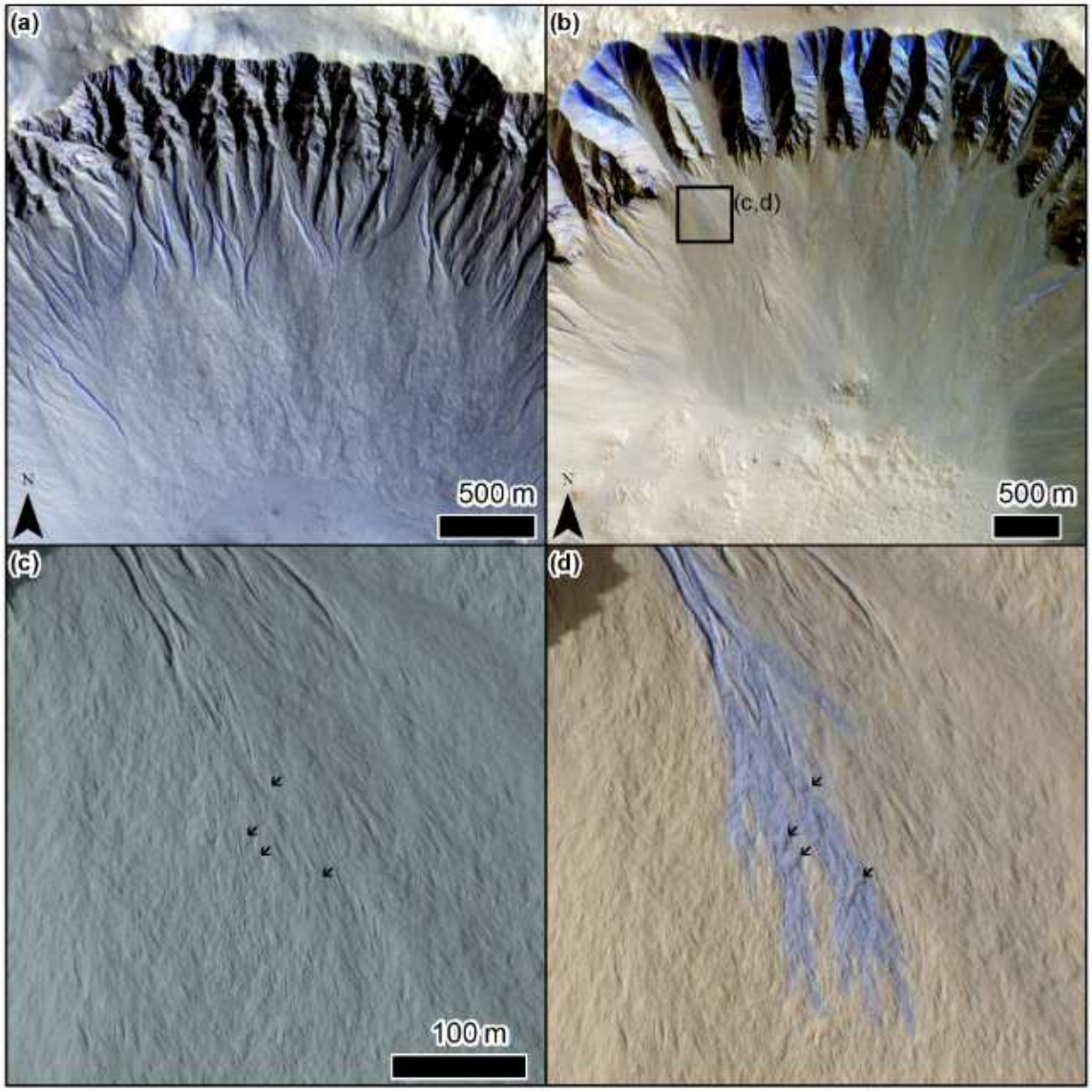

1074
1075 Figure 9. (*a*) Gullies in Galap crater in CaSSIS image MY34_005744_220_1. (*b*) Gullies in Gasa crater
1076 in CaSSIS image MY34_005684_218_1, with black box showing the location of detailed panels (*c*, *d*). (*c*)
1077 Image of a gully fan prior to a depositional event, HiRISE image ESP_012024_1440. (*d*) Image of a gully
1078 fan after a depositional event, HiRISE image ESP_020661_1440. Arrows point to lobate deposits not
1079 visible in previous image. Incidence angles for *(c)* and *(d)* are 57.4 and 57.9°, respectively, so these
1080 changes are not an illumination effect; see *Dundas et al.* (2012) for an animation that provides a blink
1081 comparison. Scale is the same as in (*c*).
1082

3.2.2 Dune alcoves

New 5–40 m wide erosional alcoves are actively forming on dune lee-side slopes in the north polar erg, often connected to a depositional apron (Figure 10); these features are called "dune alcoves" rather than "dune gullies" (§3.2.1), as they generally lack a channel. Newly formed alcove-apron features in the north polar erg were first reported on by *Hansen et al.* (2011), who noted that these features formed annually and were found on ~40% of the dune slopes. In that study, the alcove-aprons were correlated with springtime sublimation activities, such as the appearance of dark spots and flows (*Gardin et al.* (2010); this timing and morphological similarity to dune gullies in the southern mid-latitudes led to the hypothesis that these features were formed through a seasonal-frost driven process— and specifically that springtime sublimation was leading to the alcove formation activity (*Hansen et al.*, 2011). Later studies demonstrated that new alcoves were visible under winter frosts (*Horgan and Bell*, 2012), but were likely forming after the first autumnal frosts, thus moving the timing of alcove formation activity to early autumn (*Diniega et al.*, 2019a*; Hansen et al.*, 2015). This led to a new hypothesis that sublimation of diurnal frosts or interactions between early autumnal surface frosts and snowfalls may initiate this mass wasting (*Diniega et al.*, 2019a; *Hansen et al.*, 2018).

Due to this difference in timing of activity as well as dune alcoves not being reactivated in subsequent Mars years (i.e., once the alcove forms, it fills in due to aeolian sand transport (Figure 10), but does not widen or lengthen during subsequent winters, as many gullies are observed to do), these features appear to be different from gullies, including dune gullies (§3.2.1). The morphologies are also different, as few dune alcoves have a channel connecting them to their depositional aprons (potential exceptions discussed in *Grigsby and Diniega* (2018)).

Subsequent studies have documented that dune alcoves are found within some mid-latitude dune fields (*Diniega et al.*, 2019b). Although a much lower number of overlapping images means timing of formation of these mid-latitude dune alcoves cannot yet be well constrained, these features are all found in dune fields that experience seasonal frost and snowfalls, thus remaining consistent with the polar erg-based hypotheses. However, improved constraints on the environments where dune alcoves form, versus environments where they do not form, remain under study and a formation mechanism model has not yet been developed.

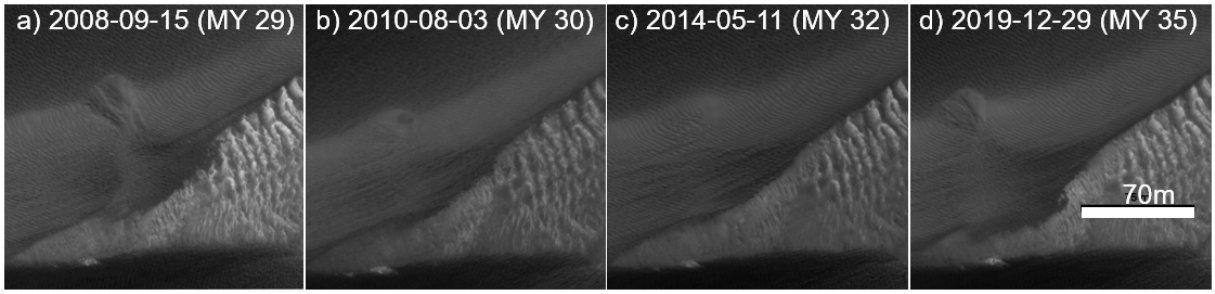

Figure 10. Example dune alcoves forming on a polar dune slope (Tleilax dune field, 83.5°N, 118.5°E). The slope fills in due to aeolian sand transport (*c,d*) and then a new nearby dune alcove forms (*d*). This is the same location as shown in Figure 4; here, all images were acquired at about the same mid-summer period (L_s 127–129°), so illumination conditions are consistent. HiRISE images are (*a*) PSP_010019_2635, (*b*) ESP_018839_2635, (*c*) ESP_036510_2635, and (*d*) ESP_062923_2635. A scale bar is shown in the last image, but absolute distances are approximate as images are not orthorectified. The bright ripples in the interdune region appear immobile over this timescale and can be used to determine relative location. North is up and illumination is from the left.

3.3 Basal sublimation formed landforms

3.3.1 Linear gullies

Martian "linear gullies" were first identified within Russell crater (*Mangold et al.*, 2003) and these decameters to kilometers-long, meters-wide troughs have since been found on a range of sandy slopes (e.g., *Dundas et al.*, 2012; *Pasquon et al.*, 2016; Figure 11). Based on their resemblance to terrestrial rills, these features were originally likened to terrestrial debris flows and proposed to be formed by surface water flow due to meltwater following a period of high obliquity (e.g., *Jouannic et al.*, 2012; *Mangold et al.*, 2003; 2010; *Miyamoto et al.*, 2004) or present-day atmospheric condensates (*Vincendon et al.*, 2010b). However, their terminal morphology (i.e., lack of debris aprons and instead ending abruptly or with pits) and the observation that some linear gully troughs and pits were forming in the present day (*Dundas et al.*, 2012; *Reiss et al.*, 2010) did not support this model.

Diniega et al. (2013) proposed a dry model, with the idea that these features may be similar to boulder-tracks—although lacking a boulder. According to this model, the trough forms due to a block of CO_2 ice rolling or sliding downslope, carving out its path on a sandy surface. Such ice forms within the seasonal frost layer that is observed to be deposited across these mid-latitude slopes each martian winter. As the frost on the dune slopes sublimes, ice remains cold trapped in shaded dune alcoves at the top of the dunes, but eventually may become dislodged, falling onto relatively warm, exposed dark sand. Sublimation at the base of this dry ice block lifts the block

slightly from the sandy surface (in a manner similar to the Leidenfrost effect), allowing it to freely roll or slide down the sandy slope, unencumbered by friction and carving out a trough. Upon stopping, the dry ice block would continue to sublime in situ, digging out a pit that then would be the remaining record after the block disappears. Field experiments with dry ice slabs slid down terrestrial desert dune slopes (*Bourke et al.*, 2016a; 2016b; *Diniega et al.*, 2013) and laboratory experiments that examine interactions between sublimating dry ice blocks and a granular substrate (*McKeown et al.*, 2017) have shown that it is feasible for the "hovercrafting dry ice block" model to broadly produce many of the observed linear gully morphologies. CO_2 ice blocks, up to ~3-m diameter, have also been observed to form and migrate downslope within martian features (e.g., *Dundas et al.*, 2012), and further modeling of interactions between CO_2 ice and sediment support development of this process in the present martian climate (e.g., *Pilorget and Forget*, 2016). However, a refined model of block transport and quantitative understanding of how linear gully morphological characteristics, such as width and sinuosity, relates to formation history has not yet been developed, limiting interpretation of these features. In particular, it is not yet known if the ~10 m-wide troughs seen in Russell crater formed under a past climate when significantly larger blocks of CO_2 may have formed, or if these have widened (albeit slowly) in the present climate due to ice blocks sliding down over many martian winters, with blocks similar to those forming new ~meter-wide troughs (*Dundas et al.*, 2012; *Jouannic et al.*, 2019; *Reiss et al.*, 2010).

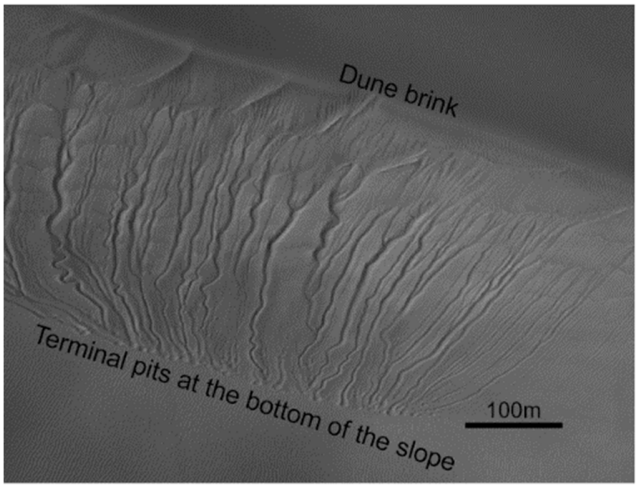

Figure 11. Example of a linear gully cluster on a climbing dune slope (50.2°S, 292.1°E), along the inside of the rim of an unnamed crater. Note the range of sinuosities, trough widths (1-10 m including levees), and pits (2-5 m) even in this one cluster. Image ID: HiRISE ESP_030624_1295, north is up and illumination is from the left.

3.3.2 Araneiforms

Araneiforms (also known as "spiders") are unique surface features that have no Earth analogs. Located primarily on the south polar layered deposits and surroundings (*Piqueux et al.*, 2003; *Schwamb et al.*, 2018), these features are characterized by dendritic, tortuous troughs several meters wide and deep which extend from a central pit and range from <50 m to 1 km in

diameter (Figure 12d). Their specific morphology types range from `fat' to `starburst' (*Hansen et al.*, 2010) and these sub-types tend to cluster non-randomly (*Hao et al.*, 2020).

These features are widely accepted to form via basal sublimation of CO_2 slab ice due to the solid state greenhouse effect *(Matson and Brown*, 1989) (see §3.1 for a longer description). As a consequence of this phenomenon, informally called the "Kieffer model," sublimation at the base of the CO_2 ice leads to a buildup of gas pressure beneath the ice overburden. Eventually this gas pressure exceeds the strength of the ice, causing it to crack or rupture at a weak spot. Pressurized gas rushes towards the vent, emerging as a plume and depositing the entrained material as fans and spots (Figure 12c). The escaping gas entrains particulates from the substrate, gradually eroding troughs *(Kieffer*, 2007; *Kieffer et al.*, 2006; *Piqueux et al.*, 2003).

Repeated venting episodes are believed to build the full extent of araneiforms over thousands of martian years (*Hansen et al.*, 2010; *Piqueux and Christensen*, 2008; *Portyankina et al.*, 2010; *N. Thomas et al.*, 2010). Most araneiform terrains show annual repeating sublimation activity: in spring, dark fans and blotches drape over troughs of araneiforms indicating CO_2 jet activity. As the ice layer continues to sublime, the bright frost is removed and so the dark deposits fade or even completely disappear, and the cycle repeats again in the next spring. However, despite continuous monitoring of araneiform terrains by high-resolution remote sensing, no detection of changes in the topography of large, well-developed araneiforms has been reported over the last 6 martian years. This leads to the question about whether the large araneiforms are currently evolving with a slow erosive process by the sub-ice CO_2 gas flow that modifies the substrate at a rate below current detection limits, or are dormant remnants of some past climate. It also highlights uncertainty in existing estimates of araneiform ages: *Piqueux and Christensen* (2003) estimated that they are at least 10^4 martian years old based on an erosion-rate estimate of ~1 m^3/yr, but *Portyankina et al.* (2017) observed erosion rates of ~8 m^3/yr.

Away from old(er) araneiform terrains, newly forming dendritic troughs have been recently detected with HiRISE (*Portyankina et al.,* 2017). These troughs form in the vicinity of sand dunes and have been observed to grow interannually (Figure 12b). Dendritic troughs are proposed to represent the early stages of araneiform formation (*Portyankina et al.*, 2017). Even smaller-scale (~tens of meters long) dendritic features known as sand furrows annually scour northern hemisphere dune slopes, but these are erased in summer *(Bourke and Cranford*, 2011; *Diniega et al.*, 2019a; Figure 12a). While laboratory experiments have replicated dendritic

patterns on granular substrate via CO_2 sublimation (*Mc Keown et al.*, 2021), the factors that distinguish the apparent disparity in activity, scale, latitudinal distribution and morphology between sand furrows, dendritic troughs and araneiforms have not yet been delineated.

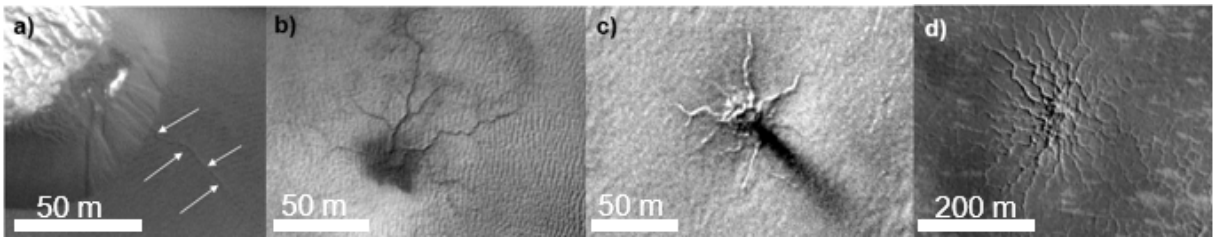

Figure 12. Examples of dendritic troughs, increasing towards right in network-complexity. The first 2 show annually active features: (*a*) dune furrows (extending towards bottom right corner from the dune brink, between arrows) and (*b*) the dendritic features described in *Portyankina et al.* (2017). The furrows disappear before the following year, while the dendritic trough has grown through multiple martian years. The two on the right (*c, d*) are araneiforms, which have not yet been observed to change. HiRISE images are from (*a*) Diniega et al. [2018] and (*b-d*) Portyankina et al. [2017]: ESP_017895_2650, ESP_011842_0980, ESP_023600_1095, and ESP_032009_0985, respectively. (NASA/JPL/UA).

3.4 Open questions for seasonal frost/ice and related landforms

For many of the landforms discussed above, observations for the timing and locations of activity implicate some form of seasonal frost/ice as a driver, and it is generally thought that the energy generated through frost/ice sublimation are a key control. However, models of frost formation and sublimation have not yet been quantitatively connected to sediment fluxes or erosion rates, and thus it is not known exactly what form(s) and amount of frost/ice may be needed to induce landform creation, evolution, or modification. Terrestrial analog studies are often used to provide a starting model (with an analog chosen based on similar geomorphology), but recent studies demonstrating that CO_2 frost/ice is a major geomorphic agent suggests that there are limits in how far Earth-based (often liquid water controlled) models can be applied. The sublimation-dominant dynamics of CO_2 frost and ice, and even H_2O when exposed under Mars pressure conditions (e.g., *Herny et al.*, 2019; *Massé et al.*, 2016; *Raack et al.*, 2017), have no terrestrial analog.

Generation of landform evolution models are hampered by lack of knowledge about the behavior and properties of the martian seasonal frost/ice layer, including how this layer evolves through the winter. Passively sensing orbital instruments generally cannot observe during the period of interest due to polar night; additionally, as the surface first reaches CO_2 condensation

temperatures in the autumn, an atmospheric haze (i.e., the polar hood) obscures visible images. No in situ measurements of the seasonal CO_2 frost layer have yet been collected due to technical challenges in having a spacecraft survive through the winter (*ICE-SAG*, 2019). Laboratory experiments have begun to look at CO_2 frost/ice formation (e.g., *Portyankina et al.*, 2019), as well as at how both H_2O and CO_2 sublimation may interact with granular materials (e.g., *Chinnery et al.*, 2018; *Herny et al.*, 2019; *Kaufmann and Hagermann*, 2017; *Massé et al.*, 2016; *Mc Keown et al.*, 2017; 2021; *Pommerol et al.,* 2019; *Portyankina et al.*, 2019; *Raack et al.*, 2017; *Sylvest et al.*, 2016; 2019; *Yoldi et al.*, 2021). By necessity due to present lab capabilities, such experiments are small-scale and simplified in terms of the variables incorporated. Eventually such experiments will also need to consider the interactions between varying amounts of different types of frost (e.g., fine-grained CO_2 snowfall over or under a layer of surface frost, or how H_2O and CO_2 surface frost may interlayer and affect optical and mechanical properties of the full frost layer). Models are also needed to scale laboratory results to natural martian conditions and to extrapolate to past environmental conditions, as well as observation of present Mars surface and atmospheric conditions to constrain and refine such models.

Finally, martian landforms with similar morphologies are often studied in aggregate, with active examples treated as analogs for similar-appearing landforms not (yet) observed to be active. In such studies, a common question is if much larger and/or more complex features that have not yet been observed to be active are active at very slow rates or if they are instead records of a past, more intense frost environment. Older records may evolve, possibly via a process continuing through shifting climate conditions, or via process(es) different from that involved in initial formation. Additionally, just as in application of comparative geomorphology between the Earth and Mars, it is possible that similar appearing morphologies on Mars may form through different processes (i.e., the principle of equifinality).

4 Long-term sublimation of ices

In the present martian climate, water ice is found in the polar caps (§4.1) and in the subsurface ($4.2–4). For all of this ice, connection to the atmosphere allows sublimation of the ice and specific geomorphologies have been tied to this volatile transport (§4.1, 4.3–4). If the rate of sublimation can be determined from the observed activity or geomorphology, the absolute ages and stability of the ice deposits can be estimated—yielding environmental constraints on recent past climates, including variations in ice formation and stability under different obliquities

(see §4.2.1). Alternatively, if the ages and sizes of past ice reservoirs can be estimated, this can yield bounds on the rate at which water ice is subliming and escaping through the regolith.

Interpreting the geological and climatological history reflected in subsurface water ice deposits requires comparison between two types of analysis: model predictions of water ice stability (as a function of depth, latitude, and subsurface thermophysical properties: §4.2.1) and observational evidence of where water ice is or was present (§4.2.2, 4.3–4). When these two lines of investigation are consistent, this provides credence to the applied models and environmental parameters. When these two lines of investigation differ, this leads to either focused questions about the models and/or assumed environmental parameters or constraints on the age of geomorphic features and preservation mechanisms (i.e., if ice may have been present in the past, but no longer exists).

4.1 Polar surface landforms

4.1.1 South Polar Residual Cap

The South Polar Residual Cap (SPRC) is a <10-m-thick layer of CO_2 ice overlying a layer of H_2O ice (*Bibring et al.*, 2004; *Byrne and Ingersoll*, 2003b; *Titus et al.*, 2003) that covers 7.9×10^9 m^2 (*P.C. Thomas et al.*, 2016) offset slightly west from the south pole, potentially due to broad-scale topography modulation of south polar circulation (*Colaprete et al.*, 2005). The CO_2 ice is incised into discrete mesas by ubiquitous sublimation pits that annually enlarge in diameter by meters per year (dubbed "swiss cheese terrain": *Byrne and Ingersoll*, 2003b; *Malin et al.*, 2001; *P.C. Thomas et al.*, 2005) and manifests in a spectacular variety of planform shapes (Figure 13; *P.C. Thomas et al.*, 2016). This annual pit enlargement led to the initial hypothesis that the SPRC is only a few hundred years old, perhaps indicating that its existence is evidence of recent climate change (*Byrne and Ingersoll*, 2003a*; Malin et al.*, 2001).

Continued cataloguing and documentation of the SPRC's diverse landforms (*P.C. Thomas et al.*, 2005; 2009; 2013) culminated in a comprehensive map of its morphology and refined estimates of its mass balance (*P.C. Thomas et al.*, 2016), including the revelation that some regions show evidence of net local and regional accumulation over the recent past (*Buhler et al.*, 2017; *P.C. Thomas et al.*, 2016). Importantly, observations indicate that widespread net annual vertical accumulation may offset local horizontal pit wall ablation, leading to net mass equilibrium with a complete turnover in material every ~100 martian years (*P.C. Thomas et al.*, 2016). Mass equilibrium is consistent with the observation that Mars' mean annual pressure is

the same to within ~10 Pa between *Viking* lander measurements and the present day (*Haberle et al.*, 2014) and SPRC landform modeling (*Byrne et al.*, 2015). Further refinement of the SPRC's annual mass balance will require observations with higher vertical accuracy and a longer baseline (*Buhler et al.*, 2018; *P.C. Thomas et al.*, 2016).

There are four broad categories of SPRC pit morphologies: circular and heart-shaped pits, linear troughs, and moats (Figure 13; *P.C. Thomas et al.*, 2016). Thus far, quantitative numerical morphological modeling can only produce circular pits (*Byrne et al.*, 2015). However, a conceptual model based upon observation indicates that all four main types of morphologies develop via the interplay of wintertime accumulation and summertime ablation (*Buhler et al.*, 2017). Aeolian reworking (*P.C. Thomas et al.*, 2020) and dust storms (*Becerra et al.*, 2015; *Buhler et al.*, 2017) may also influence morphologic development and mass balance. Future maturation of numerical landform models will be essential for quantifying the mass balance of the SPRC under orbital (i.e., polar insolation) conditions different from the modern day.

In the conceptual model of morphologic development (Figure 13; *Buhler et al.*, 2017), summertime sunlight causes internal sublimation of the SPRC, leading to the collapse of its surface, creating fractures. The roughness caused by fracturing leads to enhanced local sublimation, forming nascent pits. Two types of nascent pits form: circular, where a fracture widens uniformly at a point, and semicircular, where one side of the fracture falls lower, forming a steep scarp and a smooth ramp. The circular pits grow larger and stay circular. The semicircular pits grow into either heart-shaped pits or linear troughs with scrolled edges. The intersection of growing scarps and slopes can create geometries where moats form.

Ablating pit walls typically leave behind an extended debris ramp of blocky, vermiform material with a lower albedo relative to the smooth-topped CO_2 mesas (*P.C. Thomas et al.*, 2020). In some regions where the surface of the CO_2 ice reaches a critical roughness, the morphology degrades into extensive (>1 km diameter) vermiform debris fields that ablate over the course of typically tens of years until the underlying H_2O ice is exposed (*P.C. Thomas et al.*, 2020). Within a few years, fresh seasonal CO_2 ice survives the summer where the H_2O ice was exposed, restarting the growth of a new, smooth-topped perennial CO_2 ice mesa.

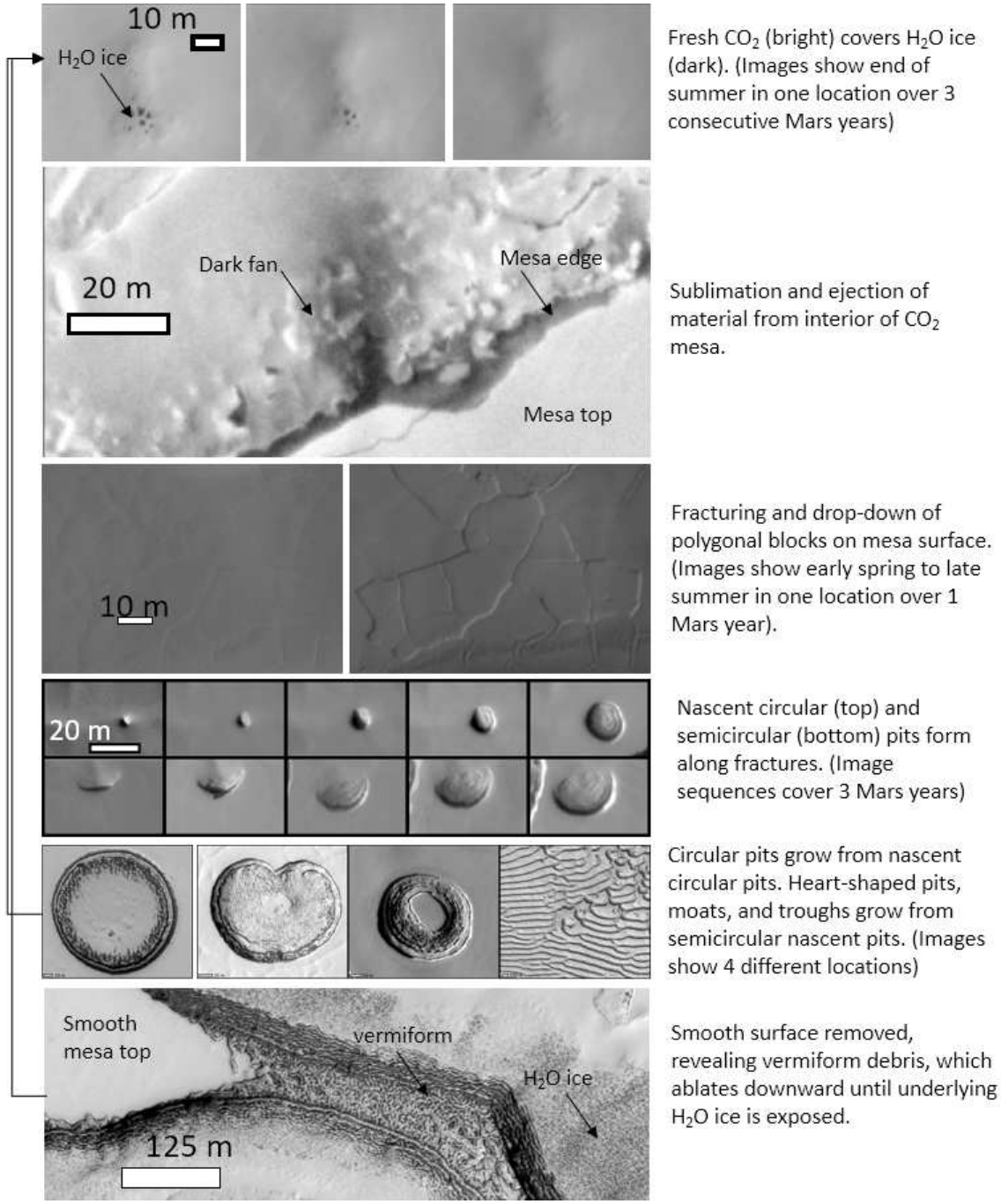

Figure 13. Cycle of CO_2 deposition and ablation in the South Polar Residual Cap (SPRC). Seasonal CO_2 deposits on exposed H_2O ice, survives summer, accumulates year-over-year to become perennial SPRC CO_2. Sunlight penetrates and heats CO_2 within mesa, causing material loss and fracturing of the mesa surface. Nascent pits form along fractures. Pits that are initially circular in shape grow into larger circular pits. Pits that are initially semicircular in shape develop into heart-shaped pits, moats, or troughs, depending on local sublimation and accumulation conditions. Horizontal pit ablation exposes underlying H_2O ice. Where the mesa surface is sufficiently damaged, vermiform terrain develops, which ablates downward until H_2O ice is exposed. Then the cycle repeats. Adapted from *Buhler et al.* (2017).

4.1.2 Massive CO_2 Ice Deposit and its capping H_2O ice layer

Exposed beneath the SPRC and covering the recently discovered Massive CO_2 Ice Deposit (MCID; *Phillips et al.*, 2011; *Putzig et al.*, 2018) is a <20-m-thick layer of H_2O ice (Figure 14c). This H_2O ice layer hosts 1- to 100-km-scale circular, scalloped, and trough depressions with depths up to ~100 m, which likely form due to sublimation and collapse of the underlying MCID (Figure 14; *Phillips et al.*, 2011). Viscous flow of the MCID likely also shapes the topography of the H_2O ice layer *(Cross et al.*, 2020; *I.B. Smith et al.*, 2016).

The H_2O ice layer is heavily fractured, which may derive from volumetric collapse due to sublimation of the underlying MCID (Figure 14; *Buhler et al.*, 2020; *Phillips et al.*, 2011) or thermal expansion (*Bierson et al.*, 2016). Material exchange between the MCID and the atmosphere through this H_2O ice layer likely keeps the SPRC in mass balance over obliquity cycles (*Buhler et al.*, 2020). Based on models, the morphology of the H_2O ice layer may be changing at ~1 mm/yr rates (*Buhler et al.,* 2020; *Jakosky et al.*, 1990) and hold important clues to whether this H_2O ice layer is permeable to CO_2 gas. Because the permeability of the H_2O ice layer is debated (*Manning et al.*, 2019), continued study of the morphology and thermal behavior of this H_2O ice layer is important for understanding the long-term (>10^4 yr) behavior of Mars' global atmospheric pressure and climate.

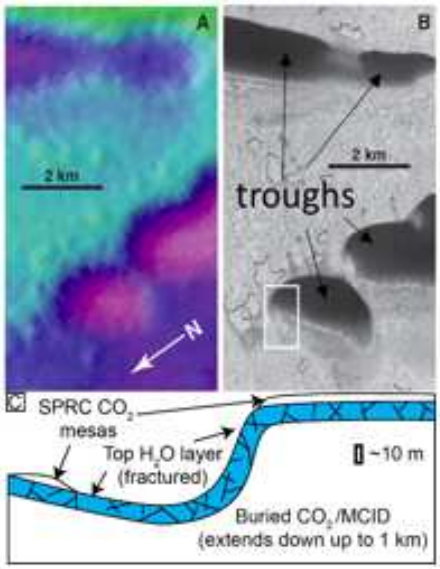

Figure 14. Depressions in the H_2O ice layer beneath the SPRC near 87° S, 268° E. (*A*) MOLA topography, ~75 m elevation range from pink (low) to green (high). (*B*) Context Camera image of the same location. H_2O ice (dark) is exposed in the troughs through windows in SPRC CO_2 ice mesas (bright). (*C*) Schematic cross section of SPRC, H_2O ice layer, and the MCID, illustrating proposed layering. A and B modified from *Phillips et al.* (2011).

4.1.3 North Polar hummocky H_2O ice surface

The surface of the perennial North Polar Residual Cap (NPRC) is primarily H_2O ice, as opposed to the CO_2 ice deposits in the south (*P.C. Thomas et al.*, 2000). The H_2O ice has a rough, hummocky texture of ~10 m-scale semi-regular depressions and mounds (*Nguyen et al.*, 2020; *Parra et al.*, 2017; *Russell et al.*, 2019). Although observations of changes within the polar region indicates there

1380 are seasonal and interannual periods and locations of both net deposition and ablation (e.g.,
1381 *Brown et al.*, 2016; *Calvin et al.*, 2015), other observations have been proposed to indicate that
1382 the current NPRC surface is underdoing net, long-term ablation. For example, large-grained ice
1383 dominates the NPRC at the end of northern summer, possibly implying exhumation of older,
1384 sintered ice (*Langevin et al.*, 2005); however, the ice also has a low dust content, indicating a
1385 lack of the dust lag that might be expected if the ice were ablating (*Langevin et al.*, 2005).
1386 Another example is that *Milkovich et al.* (2012) observed that the wavelength of the hummocky
1387 texture has a positive correlation with elevation and latitude, which they interpreted as indicating
1388 the formation of the hummocky texture via ablation. However, modeling by *Wilcoski and Hayne*
1389 (2020) indicates that hummocks would form in both ablational and depositional settings and,
1390 further, that hummock wavelength correlates primarily with age regardless of net ablation or
1391 deposition; they find that the typically observed ~10 m hummock wavelengths are reached after
1392 ~1 kyr. This timescale is consistent with ~1.5 kyr ages derived from cratering statistics (*Landis et*
1393 *al.*, 2016). Ablation and deposition of H_2O ice also modify craters on the NPRC, with the current
1394 crater population being estimated to have accumulated within the last ~20 kyr and ice
1395 accumulation rates within craters of ~3–4 mm/yr (*Banks et al.*, 2010).
1396 Wind is also likely a driver for evolving geomorphology of icy features on the NPRC
1397 because it can influence volatile fluxes at the surface, vapor transport, and distribution of both
1398 CO_2 and H_2O ice. However, most of these processes driven by both wind and sublimation are not
1399 directly observable due to very slow rates. Large-scale features like the chasmae/spiral troughs in
1400 the NPRC are thought to have formed into their present state over millions of years of erosion by
1401 katabatic winds and asymmetric insolation/sublimation (e.g., *Bramson et al.*, 2019; *Howard*,
1402 2000; *Smith and Holt*, 2010). Smaller-scale periodicities in the landscape may be related to
1403 sublimation dynamics of perennial ice layers interacting with the winds over thousands of years
1404 (e.g., *Bordiec et al.*, 2020; *Herny et al.*, 2014; *Howard*, 2000; *Nguyen et al.*, 2020).
1405 Because the NPRC is the uppermost layer of the NPLD (Tanaka et al., 2005), further study of
1406 NPRC surface morphology evolution will be important for understanding how layers
1407 accumulated in the NPLD, as well as how structure of the layers may record aeolian and
1408 sublimation interactions when that layer of material was exposed on the surface, and how to
1409 interpret the climate under which those layers formed (*I.B. Smith et al.*, 2020). The layers within
1410 the NPLD (and in the Southern Polar Layered Deposits (SPLD)) are of high interest for Mars

polar and climate studies because they are thought to be analogous to the layers found within terrestrial ice cores and thus record martian climate cycling (*I.B. Smith et al.*, 2020).

4.2 Present/recent subsurface water ice

4.2.1 Present-day water ice stability

The fundamental principles controlling subsurface H_2O ice stability have been understood for some time (e.g., *Smoluchowski*, 1968). Given some water vapor content in the atmosphere, ice will be deposited in locations that are below the frost point temperature and will sublime at locations that are warmer. Integrated over the course of a martian year, ice is stable at locations where the average water vapor pressure over ice is less than or equal to that in the atmosphere; these locations will also experience net deposition. At equatorial latitudes under current conditions, temperatures are too warm for ice to be stable, and ice does not accumulate. At middle to high latitudes, peak surface temperatures may still be high, but annual and seasonal variations are damped in the subsurface. The equilibrium water vapor pressure is nonlinearly dependent on temperature, which allows ice to become stable in the shallow subsurface, at a depth that becomes shallower with increasing latitude.

The development of increasingly sophisticated maps of the distribution of stable ice, based on the above framework, is summarized by *Mellon et al.* (2004). Recent ice stability maps have also been produced by *Chamberlain and Boynton* (2007), *Schorghofer and Aharonson* (2005), and *Steele et al.* (2017). Broadly, these all place the present-day stability boundary near 45–60° latitude, and show similar longitudinal variations correlated with surface albedo and thermal inertia. Differences in ice stability predictions are largely due to assumptions of near-surface atmospheric water vapor content and past atmospheric conditions.

Mars' orbit varies over time, leading to H_2O ice sublimation and deposition as the global ice stability field evolves in response. *Dundas et al.* (2014) found that ice newly exposed by fresh impact craters persisted for longer than expected, given the currently measured atmospheric water vapor column. Their observations indicated that either the lowest-latitude ice has not equilibrated with the current climate or that the ice is stabilized by local factors, such as enhanced near-surface water vapor concentration. Remnant out-of-equilibrium ice that was deposited recently (within ~1 Ma) provides one possible explanation for the low-latitude icy craters (*Schorghofer and Forget*, 2012). Similar modeling by *Bramson et al.* (2017) concluded that such ice could be considerably older (>10s Ma) than estimated by *Schorghofer and Forget*

(2012) if the ice started sufficiently thick and has also been protected by thick lag deposits built up by dust and lithic debris released from the sublimating ice.

The current solutions for Mars' orbital variations (*Laskar et al.*, 2004) indicate that ~4 Ma, Mars entered a low obliquity epoch in which mid-latitude ice has generally been less stable and polar ice has been more stable. Correspondingly, modeling and observations indicate net transport of ice from the middle latitudes to the poles over this timeframe (e.g., *Levrard et al.*, 2007; *I.B. Smith et al.*, 2016). However, higher frequency (~50 to 100s of kyr) periodicities in Mars' orbital parameters (particularly obliquity) likely generate many excursions away from the long-term average conditions. Therefore, the spatial distribution of ice deposition and sublimation has likely been very dynamic over ~50 to 100 kyr timescales. Understanding this dynamic movement of ice is essential to deciphering the evolution of icy terrains. The modeling described above shows that the current distribution and stability state of mid-latitude ice could place important constraints on Mars' recent past climate. Such model predictions can be coupled with observations of landforms (such as sublimation thermokarst, patterned ground, and viscous flow features) to improve interpretation of such landforms or to test the climate condition assumptions.

4.2.2 Present-day water ice distribution

Presently, exposed water ice is only stable on the surface at the poles; it is stable at lower latitudes when buried in the subsurface under an insulating, desiccated coating of dust and/or regolith. Data from the Mars Odyssey Neutron Spectrometer show the near subsurface (within the upper meter) at middle and high latitudes to be hydrogen rich, which has been attributed to the presence of water ice (*Boynton et al.*, 2002; *Pathare et al.*, 2018). As discussed in §4.3–4.4, numerous geomorphological features, including glacial and viscous flow features, thermal contraction polygons, and ice-loss (also referred to as thermokarstic) terrains, suggest a recent and/or present-day ice-rich subsurface across most of the mid-latitude plains. Thermal analysis indicates widespread water ice at latitudes as low as 35°N/45°S, with high lateral ice depth variability—sometimes buried only a few centimeters below sand-like material—and correlated with putatively periglacial features (*Piqueux et al.*, 2019).

Due to warm temperatures at the equator, in general, the ice must be buried at greater depth for increasingly-equatorward locations (e.g., *Fanale et al.*, 1986; *Leighton and Murray*, 1966;

Paige, 1992). For example, the Phoenix lander excavated nearly pure water ice in the upper centimeters of the surface at 68°N (*P.H. Smith et al.*, 2009). Recently-discovered scarps near ~55° latitude in both the northern and the southern hemispheres expose thick, massive ice that appears to extend to within a meter of the surface in high-resolution images (*Dundas et al.*, 2018). These slopes can be several kilometers long and over 100 m tall. Bare ice at these locations likely are actively subliming; *Dundas et al.* (2018) observed boulders falling from one scarp and estimated that the sublimation rate was on the order of millimeters per year. Additionally, H_2O ice spectral features at a second scarp weakened over the course of the summer, suggesting the gradual accumulation of a thin sublimation lag of dust. This ice loss results in ongoing slope retreat and the growth of depressions, which are morphologically distinct from the thermokarst features discussed below (§4.3), likely because a bare ice surface is maintained in these landforms (*Dundas et al.*, 2018).

Recent (<15 years old) impact craters have exposed and excavated nearly-pure water ice (likely >90% ice by volume) within a meter of the surface as close to the equator as 39°N (*Byrne et al.*, 2009; *Dundas et al.*, 2014). The appearance of these exposures slowly fades over time as the exposed ice sublimes (*Dundas and Byrne*, 2010). Some of the ice remains distinctive in color for several martian years (*Dundas et al.*, 2014), indicating clean ice (>90% water ice by volume) with a low lithic content.

Ice is not expected to be stable near the equator at any depth, though the most equatorward boundary of subsurface mid-latitude ice is still an outstanding question and unstable, sublimating ice may exist. Recent efforts have focused on integrating numerous datasets and techniques to constrain the distribution of mid-latitude ice, especially from the perspective of its utilization as an in situ resource for crewed missions, and include studies across swaths of the northern plains regions (*Orgel et al.*, 2019; *Ramsdale et al.*, 2019; *Sejourne et al.*, 2019) as well The Mars SWIM (Subsurface Water Ice Mapping) Project (swim.psi.edu). So far, the areas found to be most consistent with abundant water ice occur poleward of ~40ºN, in the northern plains region of Arcadia Planitia, where widespread ground ice was previously inferred in radar sounding and geomorphic crater studies (*Bramson et al.*, 2015; *Viola et al.*, 2015), and within an extensive network of debris-covered glaciers in the Deuteronilus Mensae region (*Petersen et al.*, 2018). This is generally more poleward than the regions focused on by human exploration planners, due to other constraints on human access and operations (e.g., *ICE-WG*, 2015).

4.3 Sublimation thermokarst

Candidate thermokarstic landscapes were identified in images dating back to the Mariner and Viking missions (*Anderson et al.*, 1973; *Costard and Kargel*, 1995; *Sharp*, 1973). These landforms result from surface collapse following loss of subsurface ice, leading to rimless depressions that are often hundreds of meters in size, and meters to tens of meters deep. Scalloped features (e.g., *Dundas et al.*, 2015b; *Lefort et al.*, 2009; 2010; *Morgenstern et al.*, 2007; *Séjourné et al.*, 2011; 2012; *Soare et al.*, 2007; 2008; 2011; *Ulrich et al.*, 2010; *Zanetti et al.*, 2010) and expanded craters (e.g., *Dundas et al.*, 2015b; *Viola et al.*, 2015; *Viola and McEwen*, 2018) are considered to be some of the most iconic examples of ice loss features (Figure 15). Initial interpretations included formation via melting akin to terrestrial thermokarst and alases (*Soare et al.*, 2007; 2008; 2011), but the present general consensus is that these are formed via sublimation.

Given the importance of temperature on ice stability, evolution of the terrain often proceeds through enhanced retreat of the warmer slopes. Under the present obliquity those are equator-facing. This leads to asymmetric landforms, with scalloped terrains often being elongated in the direction of retreat and exhibiting shallower slopes on the equatorward-facing slopes. It has been debated whether the scalloped depressions form primarily via retreat of the pole-facing slope at high obliquity (*Séjourné et al.*, 2011; *Ulrich et al.*, 2010) or retreat of the equator-facing slope under conditions similar to the present (*Lefort et al.*, 2009; *Morgenstern et al.*, 2007; *Zanetti et al.*, 2010). More complicated landscapes can form through the merging of the features, and the intervening terrain between collapse features is generally thought to retain the ice-rich subsurface unit.

Numerical landscape evolution modeling (*Dundas*, 2017; *Dundas et al.*, 2015b) shows that standard martian ice-stability theory (§4.1) can produce both scalloped-depression and expanded-crater morphologies via sublimation. The model is driven by surface topography and a high subsurface ice content, which produce uneven sublimation and an evolving landform. In the model, retreat of both pole- and equator-facing slopes occur, although the latter appears to be most important. The subsurface ice loss is triggered by some local disturbance (such as an impact, in the case of expanded craters). Modeling of the process suggests that these landforms may take 10^4–10^5 years or more to form, though the development of a sublimation lag will eventually help preserve these landforms from additional ice loss (*Dundas et al.*, 2015b).

These landforms likely develop gradually over tens to hundreds of thousands of years (*Dundas*, 2017; *Dundas et al.*, 2015b) since the surface debris slows sublimation and protects the ice from high peak temperatures. As such, landform evolution is unlikely to be occurring at scales that are observable from orbit, unless slow ice loss occasionally triggers larger mass wasting events. However, given the likelihood of out-of-equilibrium ice (§4.1), it is likely that at least some of these sublimation-thermokarst features are evolving at present. It is even possible that this could occur in ice that is generally in equilibrium, since the process will work on any slope that is locally out of equilibrium.

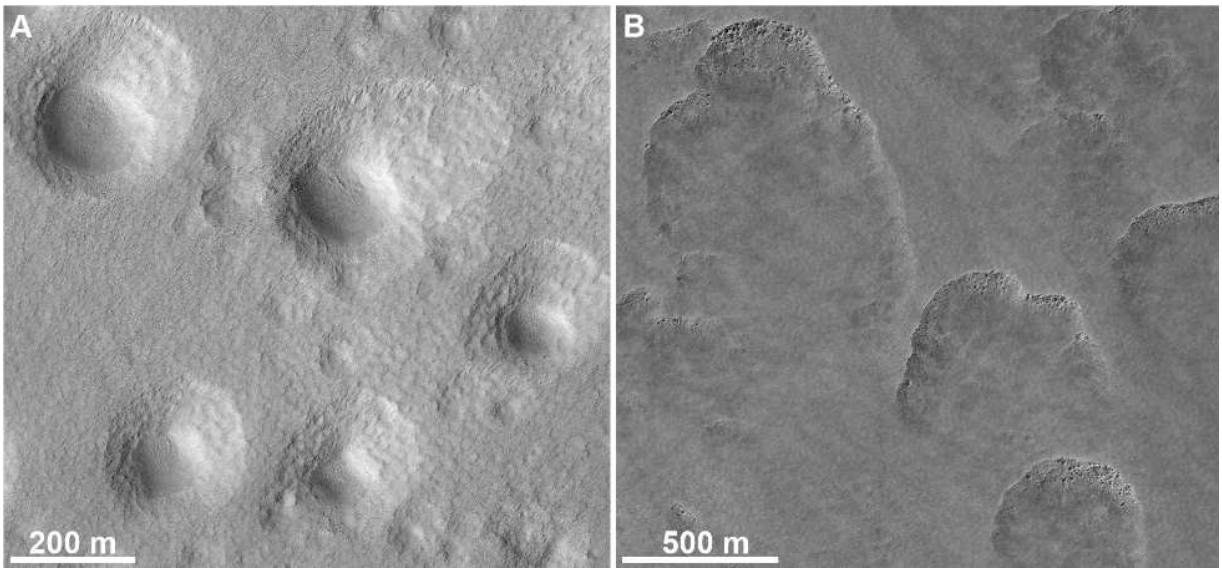

Figure 15. (*A*) Expanded secondary craters on the northern plains. Note funnel shape suggesting widening and shallowing of the rim. HiRISE image ESP_045303_2320. (*B*) Scalloped depressions south of the Hellas basin (58.1° S, 74.0° E). Note the steep pole-facing slopes. HiRISE image ESP_049581_1215. In both images, illumination is from the left and north is up.

4.4 Patterned Ground

Polygonally patterned ground, containing polygons with a wide large range of diameters (meters to tens of kilometers), is one of the most common and, based on superposition, youngest landforms on Mars. Polygonally patterned ground is either sorted (with surface patterns defined by rock fragments) or unsorted landforms (with surface patterns defined by thermal contraction cracks without sediment motion) (*French*, 2007). On Earth, sorted patterned ground is most commonly found in fine-grained sediments overlain by coarser rock fragments because these are the most susceptible to frost heave and sorting as a function of grain size during freeze-thaw cycling (*Kessler and Werner*, 2003). In addition to the polygons, stripes, piles, and other

morphologies found on Earth are also found on Mars, and with transitions between them occurring in the same way as on Earth, lending support for the "convection" model that is freeze-thaw sorting (e.g., *Gallagher and Balme*, 2011; *Gallagher et al.*, 2011; *Soare et al.*, 2016), although such processes can also occur on Earth without freeze-thaw (e.g., *Sletten et al.*, 2003). The limit of HiRISE resolution (Table 1) necessitates that all clasts used to define sorted patterned ground consists of boulder-sized or larger sediments. *Soare et al.* (2019) also used locality with potential pingos in such feature identification.

Non-sorted polygonally patterned ground (thermal contraction crack polygons) are widespread on Mars and dominate surfaces poleward of ~30-40˚ latitude (*Levy et al.*, 2009b; *Mangold*, 2005) where ground ice is abundant (*Boynton et al.*, 2002) and where thawed active layers (portions of the soil column that seasonally freeze and thaw) have been rare to absent on flat-lying surfaces over at least the past ~5 Ma (*Kreslavsky et al.*, 2008). Thermal contraction crack polygons on Mars are overwhelmingly high-centered features with low bounding troughs, although examples of low-centered polygons with elevated shoulders occur in a few locations (Figure 16) (*Soare et al.*, 2014; 2018). The more common high-centered morphology indicates that either excess ground ice has escaped via sublimation along the fracture traces, and/or that infilling of fractures by fines is slow compared to subsurface ice loss. Alternatively, the center might be deformed upwards by pressures created by aggrading sand wedges (e.g., *Sletten et al.*, 2003).

Thermal contraction cracks can form under modern martian climate conditions (*Mellon*, 1997), suggesting that polygons are actively forming and expanding locations where ice-rich permafrost and/or buried ice is present (*Mellon et al.*, 2008). Continued formation and growth of thermal contraction crack polygons is consistent with observations that polygon fracture networks crosscut many young deposits on Mars, including gully fans (*Levy et al.*, 2010) (Figure 16). In many locations, ice-rich mantling deposits (e.g., *Head et al.*, 2003) are extensively fractured, with polygon troughs cross-cutting almost all but the most recent impact craters (*Byrne et al.*, 2009; *Levy et al.*, 2010), suggesting that mantling units may have crater retention ages of 10-100 kyr.

While there is little debate about the origin and current activity of unsorted patterned ground on Mars, the widespread existence and mechanism of formation for sorted patterned ground are both topics of considerable debate, particularly as to whether freeze-thaw is necessary for its

formation. Potential sorted patterned ground consists of three main groups: high-latitude boulders concentrated in thermal contraction crack troughs (*Levy et al.*, 2009b; *Mellon et al.*, 2008; *Orloff et al.*, 2011), clasts arranged in boulder halos (*Barrett et al.*, 2017; *Levy et al.*, 2018), and low-latitude albedo networks (*Balme et al.*, 2009). Boulders may be sorted into polygon troughs at high latitude via slumping of over-steepened trough shoulders (*Levy et al., 2010; Mellon et al.*, 2008), seasonal frost-related locking and sliding mechanisms (*Orloff et al.*, 2013), or differential inflation of soil profiles at polygon troughs vs. centers (*Levy et al.*, 2018). At middle latitudes where boulders are present in rock rings called boulder halos, boulders commonly cluster in beaded networks (Figure 16), some of which are confined to polygon troughs and some of which are not, leading (*Barrett et al.*, 2017) to interpret these sites as possible evidence of freeze-thaw-driven sorting under near-recent climate conditions. Finally, equatorial examples of potential clastic networks have been identified near Cerberus Fossae (*Balme et al.*, 2009). These occur in the absence of thermal contraction crack polygons and have been interpreted as evidence of relict freeze-thaw heaving mechanisms. A lack of meter-scale or larger boulders in these deposits (Figure 16) makes these deposits less comparable to the sorted clasts observed in the other two examples, and their proximity to volcanic deposits associated with Cerberus Fossae outflow raises the possibility that they are features of volcanic origin.

On Earth, sorted patterned ground can form on timescales of years to millennia (*Hallet*, 2013), while unsorted patterned ground typically matures over millennial to million-year timescales (*Levy et al.*, 2006; *Marchant et al.*, 2002; *Sletten et al.*, 2003). Rates of thermal contraction crack wedge expansion typically are on the order of millimeters per year, challenging efforts to detect change in martian patterned ground. However, it is likely that patterned ground formation and evolution—especially thermal contraction crack fracturing and wedge growth are occurring on modern Mars and are actively working to resurface middle- and high-latitude landscapes.

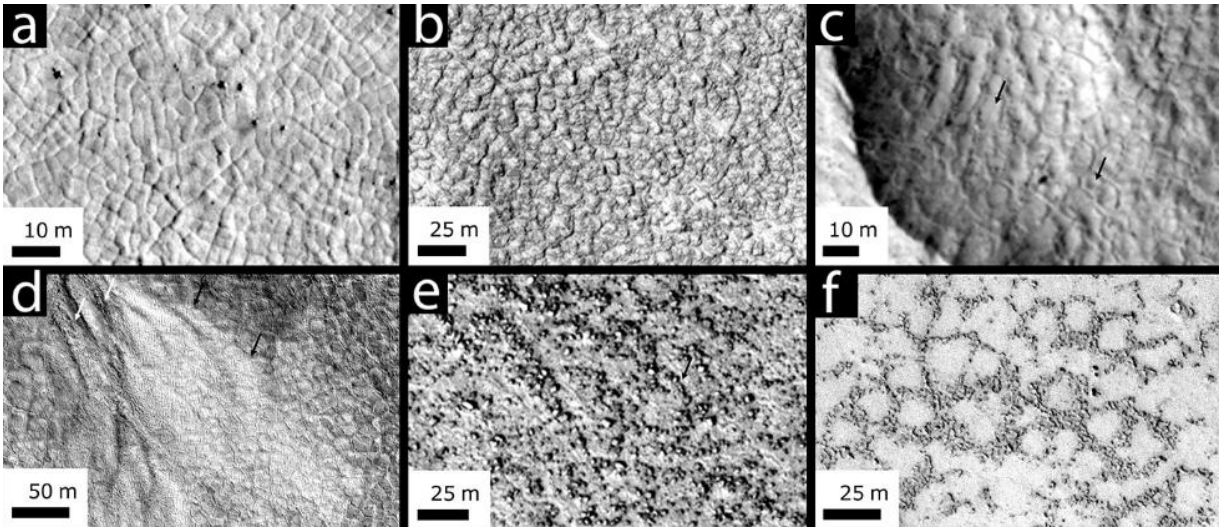

Figure 16. Polygonally patterned ground on Mars. (*a*) High-centered, unsorted patterned ground. Portion of HiRISE image PSP_001474_2520. (*b*) High-centered, unsorted patterned ground. Portion of HiRISE image PSP_003217_1355. (*c*) Example of low-center / raised-rim unsorted patterned ground. Arrows point to low-centered polygons. Portion of HiRISE image PSP_002175_2210. (*d*) Bright gully fan material (black arrows) emerging from a gully channel (white arrows) that has been crosscut by underlying thermal contraction cracks. Portion of HiRISE image PSP_001846_2390. (*e*) Candidate sorted patterned ground. Portion of HiRISE image ESP_017580_2460. (*f*) Candidate low-latitude, sorted patterned ground. Portion of HiRISE image PSP_004072_1845.

4.5 Open questions for long-term sublimation of ice

A primary goal of Mars polar science investigations is to unlock the climate history stored in Mars' polar deposits (*I.B. Smith et al.*, 2020). Improved estimates of the modern annual polar CO_2 and H_2O ice and nonvolatile mass balance, coupled with a better understanding of the annual reworking of the SPRC and NPRC surface, will be essential to interpreting the climatic conditions encoded in layers of the NPLD and SPLD. Improved observational resolution, cadence, and baseline of observations as well as development of physics-based numerical simulations that are capable of reproducing morphologic observations of polar landforms will both be critical to this endeavor. Additionally, the net annual mass flux of polar material remains poorly constrained. Improved measurement of atmospheric transport of volatiles and dust as well as observation and modeling of surface morphology (including its evolution), seasonal frost layer evolution (§3.4), and thermal cycles of the surfaces of the SPRC and NPRC will greatly enhance our understanding of the current net annual polar mass balance.

Outside of the polar region, a global map of where ice is presently found in the subsurface (and at what depth) along with the structure, volume, and purity of that ice is needed. This is of

particular interest for understanding where ice is currently aggrading or sublimating. Improved knowledge of the near-surface water vapor concentration is also needed to understand the equilibrium distribution of ice (i.e., where it "should" be). Phoenix measurements suggest a stronger atmosphere-regolith interchange in the martian arctic than at lower latitudes (*Fischer et al.*, 2019) and orbital column measurements are challenged by possible near-surface concentration of vapor (*Tamppari and Lemmon*, 2020; *Tamppari et al.*, 2010). Also needed is characterization of the surface materials over this ice—especially its depth and bulk thermoconductive properties. More refined information about the structure of the lag (and variations in its thermoconductive properties) would provide additional constraints for development and testing of models related to the preservation of ice (Figure 17). In particular, an understanding of the impact of the dust component of lags would contribute to estimates of dust accumulation through recent martian history, feeding new constraints into studies of present and past climates, how dust can influence ice layer evolution and accumulation, and sediment transport pathways and reservoir amounts.

Generally, improved measurements of the thermoconductive, mechanical, and compositional properties of regolith where discussed geomorphologies and/or ground ice are found would enable improved modeling and laboratory investigations of the processes discussed here. Improved process models would in turn enable improved interpretation of these landforms, regarding their formative environments and ages. In general, global identification of these geomorphological features is complete (or can be completed) down to the decameters-scale within global CTX imagery; higher resolution images are needed to map polygons and other smaller morphologies.

Addressing these open science questions would also contribute towards high-priority human exploration questions regarding in situ resource utilization (ISRU). Water ice deposits within a few meters of the surface are of high interest for human and fuel needs, and regolith (including sublimation lag deposits) properties would feed into mining and operations designs.

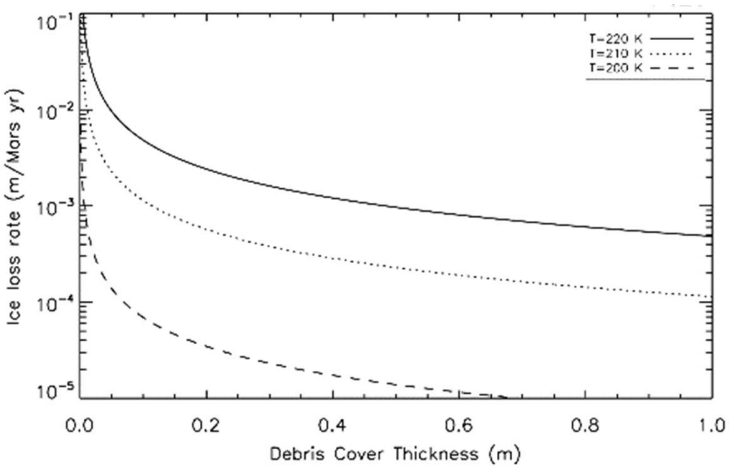

Figure 17. Retreat rate of ice under lags of varying thickness at T=200, 210, and 220 K, assuming background atmospheric water vapor with a frost point of 198.5 K.

Calculation follows *Hudson et al.* (2007).

5 Mass-wasting aided landforms

In addition to the wind- and frost-driven features discussed above that involve mass wasting (§3.2: gullies, dune alcoves) and gravity-driven transport (§3.3: linear gullies), here we discuss two additional examples of observed downslope movement of materials. For these two cases, a suite of processes may be involved in initiation and enhancement of the transport; gravity is the only well-established driver. Recurring slope lineae (§5.1) were originally proposed to be driven by liquid water, but, as is discussed, the initiation mechanism for the formation of these features is not yet conclusively established and current observations may be more consistent with a dry mass-wasting mechanism. Avalanches and rockfalls (§5.2) both obviously occur due to gravity, with initiation mechanisms potentially related to thermal stresses and, from at least icy slopes, sublimation.

5.1 Recurring Slope Lineae (RSL)

Recurring slope lineae (RSL; Figure 18; SOM 7) are relatively dark linear markings on steep slopes with low albedos (indicating relatively little coverage by bright dust), typically originating at bedrock outcrops *(McEwen et al.*, 2011; 2014). Individual lineae are up to a few meters wide and up to 1.5 km long. The lineae grow incrementally or gradually over several months, usually during the warmest time of year, then fade (and typically disappear) when inactive. RSL recur in multiple martian years (by definition) over the same slopes, but not necessarily every year and not necessarily at the exact same locations. RSL often follow pristine small gullies or channels. Hundreds of individual lineae may be present over a local slope, and thousands are captured in single HiRISE images in some cases. A confirmed site (each HiRISE image sequence is considered a site) is where repeat images show incremental growth and fading, repeated over multiple martian years. A candidate site has similar-looking features in the same settings and seasons as typical RSL, but repeat imaging of the site is insufficient to document growth, fading, and recurrence. There were at least 98 confirmed and 650 candidate sites prior to MY34 (*Stillman*, 2018) (Figure 2).

RSL are common in *(1)* the southern middle latitudes (-60° to -30° latitude) where they are most active in southern summer on generally equator-facing (including east- and west-facing) slopes; *(2)* the equatorial regions where activity is usually coincident with the local slope receiving peak insolation; and *(3)* in Acidalia/Chryse Planitia and other northern middle latitudes with activity in northern spring and summer (*McEwen et al.*, 2011; 2014; *Stillman*, 2018; *Stillman and Grimm*, 2018; *Stillman et al.*, 2014; 2016; 2017). However, exceptions to these timing patterns do occur (*Dundas*, 2020a; *Ojha et al.*, 2014).

Figure 18. Hundreds of RSL present on the northwest-facing slope of a 935 m diameter simple impact crater, imaged at L_s 313° (southern summer) of MY34, located at 47.3° S, 1.3° E. Black arrows point at the lowermost tips of a few lineae, which begin near the crater rim. The full HiRISE image shows hundreds of dust devil tracks, indicating fresh dust deposition during the MY34 planet-encircling dust event (PEDE) in southern spring. Color composed of infrared, red, and blue-green bandpasses, stretched to increase contrast. North is up and illumination is from the northwest (upper left). ESP_058208_1325.

Many publications have favored wet models for RSL activity (e.g., *Chevrier and Rivera-Valentin*, 2012; *Grimm et al.*, 2014; *Huber et al.*, 2020; *Levy,* 2012; *McEwen et al.*, 2011; 2014; *Ojha et al.*, 2013; 2014; 2015; *Stillman*, 2018; *Stillman and Grimm*, 2018; *Stillman et al.*, 2014; 2016; 2017; *Wang et al.*, 2019). The darkening and gradual growth resembles seeping water, and the fading could be explained by drying. RSL appearance and temporal behavior are similar to that of water tracks in Antarctica (*Dickson et al.*, 2013; *Levy*, 2012). The surface temperatures corresponding to RSL activity are above the freezing points for salty solutions, which can be as low as nearly 200 K (e.g., *Möhlmann and Thomsen*, 2011). However, explaining the source of sufficient water for seepage is extremely difficult in the present-day martian environment (e.g.,

Dundas et al., 2017, and references therein). Evidence for water playing some role in RSL from detection of rare hydrated salts (*Ojha et al.*, 2015) now appears to be a data processing artefact (*Leask et al.*, 2018; *Vincendon et al.*, 2019). Deep groundwater may persist in Mars and might occasionally reach the surface (*Abotalib and Heggy*, 2019; *Stillman et al.*, 2016), but RSL are found over a wide range of elevations and settings not consistent with natural groundwater discharge, including the tops of isolated peaks and ridges (*Chojnacki et al.*, 2016). Highly deliquescent salts are known to exist on Mars and may temporarily trap atmospheric water in extremely small quantities, perhaps sufficient to darken the surface (*Heinz et al.*, 2016), but not sufficient for seepage down slopes (*Gough et al.*, 2019a; 2019b). Some workers have speculated that small quantities of water could trigger granular flows (*Dundas et al.*, 2017; *McEwen,* 2018; *Wang et al.*, 2019). Relatively small quantities of boiling water may trigger granular flows (*Herny et al.*, 2019; *Massé et al.*, 2016; *Raack et al.,* 2017), but these quantities are far more than can be supplied by the martian atmosphere with a typical water column abundance of 10 precipitable microns (*M.D. Smith*, 2008). Other hypotheses are that mass wasting may occur when damp surface materials dehydrate (*Schorghofer et al.*, 2002) or from migration of subsurface brines (*Bishop et al.*, 2020). Surface frost (CO_2 and H_2O) forms in only some RSL source regions and will sublime before RSL typically become active (*Schorghofer et al.*, 2019).

Some recent papers have favored dry RSL models. *Edwards and Piqueux* (2016) found that the thermal signature of RSL-bearing slopes at Garni crater was consistent with <3% water, although *Stillman et al.* (2017) pointed out that none of the thermal observations were synchronous with observations of sufficient coverage by lineae to enable thermal detection. *Schmidt et al.* (2017) suggested that RSL could operate via granular flows driven by a Knudsen-pump gas-flow mechanism enhanced by distinct shadowing. *Dundas et al.* (2017) found that RSL terminate on slopes matching the dynamic angle of repose for dry sand. *Tebolt et al.* (2020) reported RSL that terminate on lower slopes, but *Dundas* (2020a) noted that some of their reported locations do not correspond to RSL. *Stillman et al.* (2020) concluded that the slopes in Garni crater were consistent with granular flows within slope errors; *Munaretto et al.* (2020) reached the same conclusion about RSL in Hale crater. *Schaefer et al.* (2019) reported evidence, including relative albedo analysis that RSL in Tivat crater fade similarly to boulder and dust devil tracks, potentially due to dust removal from the larger region, and proposed that RSL are dry features that mobilize dust. *Vincendon et al.* (2019) also proposed that RSL are due to dust

removal based on relationships between RSL and aeolian activity. *Dundas* (2020a) proposed that RSL are grainflows where sand is seasonally replenished by the uphill migration of ripples, most of which are smaller than the 25-30 cm/pixel scale of HiRISE. Following the MY34 planet-encircling dust event (PEDE) in 2018, there was a pronounced increase in RSL activity (>5x the activity in other years), showing a close connection to recent atmospheric deposition of dust (*McEwen et al.*, 2019; 2021). Dust lifting activity (also forming dust devils) may directly cause RSL formation on steep slopes, and/or dust storms may correlate with some other factor, such as sand transport, that facilitates later RSL activity (*Dundas*, 2020a).

5.2 Avalanches/block falls from rocky and icy slopes

Both individual fragments and clouds of material have been mobilized down steep slopes and cliffs of both rock and ice on Mars. Rocks tumbling down hillslopes leave bounce and roll-marks in their wake, whose distribution around impact craters has been used to infer that thermal stress is a necessary pre-conditioning factor for their release (*Tesson et al.*, 2020). Other studies have used the presence of these rockfall tracks as evidence of seismic activity on Mars (*Roberts et al.,* 2012; *Brown and Roberts*, 2019; *Senthil Kumar et al.*, 2019). Rocks have also been observed to move downslope without leaving a visible track on the surface, in a manner that suggests an independent rock-transport process (*Dundas et al.*, 2019b; *Raack et al.*, 2020). Precise timing data are often lacking and sometimes contradictory, therefore further work is needed to investigate connections between rock breakdown and frost accumulation/sublimation or other seasonal effects.

Avalanches and blocks (Figure 19) have been observed to descend from the steep scarps of the northern polar ice cap of Mars (*Fanara et al.*, 2020a; 2020b*; Herkenhoff et al.*, 2007; *Russell et al.*, 2008;). These appear to be two separate categories of mass movement because the avalanches are rarely associated with mobilized blocks and spectral evidence suggests they could simply be mobilizing the surface seasonal frost deposits (*Pommerol et al.*, 2013). Avalanches observable at the time of day of HiRISE observations occur exclusively in early spring (*Russell et al.*, 2014). Some scarps appear to be more active than the others, hinting at the importance of some type of localized conditions such as near-surface winds or sun exposure (*Russell et al.*, 2014). However, it is still an open question regarding whether the origin of these avalanches is caused by the thermal stresses in the scarp, sublimation of the seasonal CO_2 deposits, the wind, or a yet-identified process (*Becerra et al.*, 2020; *Byrne et al.*, 2017). Conversely, the fallen

blocks of ice are thought to be detached by thermal stresses on these exposed locations and were thought to potentially balance the deformation of the scarps via viscous deformation (*Sori et al.*, 2016). However, the fallen blocks at one well-studied north polar site account for a minimum average scarp retreat rate of ~0.2 m/kyr, which does not balance the published 0.01–1 m/yr viscous flow rates, suggesting that either viscous flow rates are lower than modeled or that additional processes act to maintain the scarps' steepness (*Fanara et al.*, 2020a). The activity of both the blocks and avalanches are important to understand because they give us insight into the mass balance of the polar cap and the climate record exposed at these steep scarps.

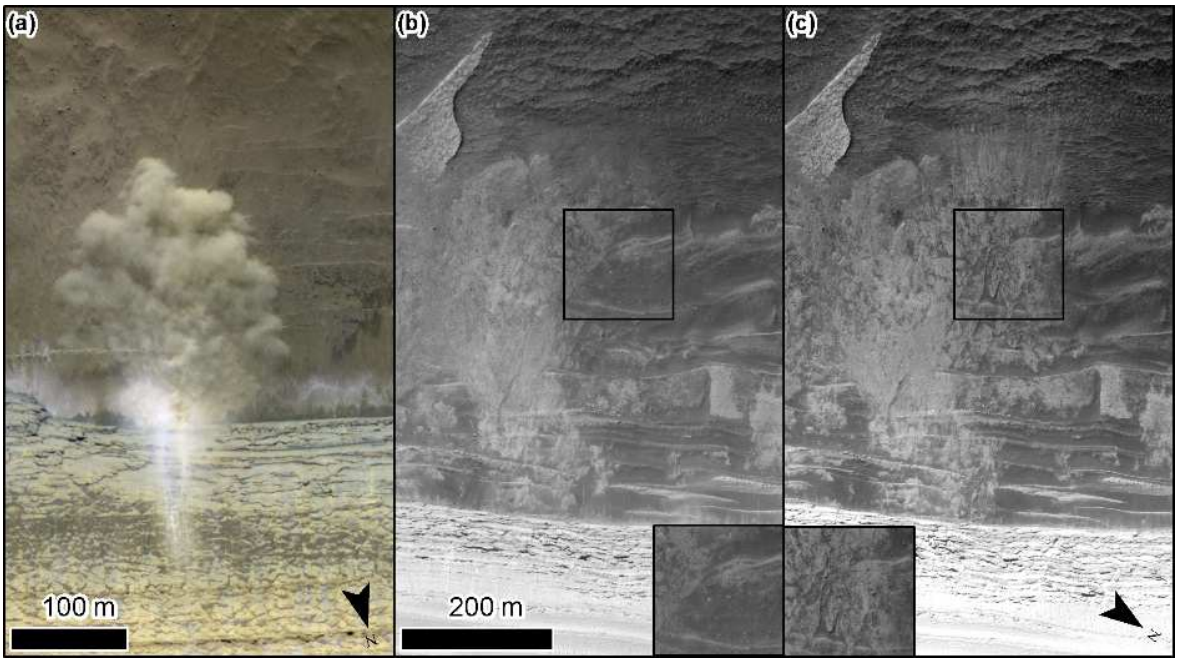

Figure 19: (*a*) Polar avalanche in enhanced-color HiRISE image ESP_016228_2650. (*b*) "Before" HiRISE image ESP_027750_2640 and (*c*) "after" HiRISE image ESP_036888 _2640 showing a blockfall with insets showing detail of the blocks and other changes between the images. The scalebar and north arrow apply to both (*b*) and (*c*) panels.

5.3 Open questions for these mass-wasting aided landforms

In general, with these mass-wasting landforms, we do not yet definitively understand the suite of processes involved and thus cannot interpret the observed landforms and activity as markers of specific environmental conditions. Volatiles, thermal cycling, aeolian processes, and/or seismicity are often invoked as drivers for initiation of the downslope transport of materials, and determining specifically (and preferably, quantitatively) what causes the activity would be useful because then these features can be used as a proxy indicator of their initiation

mechanism. Additionally, understanding the role of volatiles in rock breakdown and mobilization is important for constraining long-term erosion rates on Mars and interpreting the degradation state of landforms (e.g., relative dating of fan surfaces in gullies).

In particular, RSL represent the latest in a series of surface features interpreted as evidence for flowing water on Mars today, given the clear preference for warmer slopes and the temporal behavior mimicking that of seasonal seeps of water on Earth. Although further observations and analyses have led to difficulties with every proposed water-driven model, given the planetary protection significance of potential water on Mars today, there is large interest in further measurements to conclusively determine the formation mechanism for these features (*ICE-SAG*, 2019; *McEwen*, 2018; *NEX-SAG*, 2015). At present, RSL sites have been classified as potential sites where terrestrial microbes might flourish (denoted "unknown special regions": *Rummel et al.*, 2014; *Kminek et al.*, 2017) and thus areas that spacecraft must avoid unless they can achieve very high levels of sterilization; for example, the presence of RSL was used to rule out candidate landing sites for the Mars 2020 rover (*Grant et al.*, 2018). If RSL are dry or only transiently wet at very cold temperatures, then this restriction on future Mars exploration could be lifted (*McEwen*, 2018), but recent work suggests that putative deliquescent RSL sites could be habitable (*Maus et al.*, 2020).

6 Summary of the measurements needed to answer remaining questions

The general aim of geomorphic studies is to connect quantitatively the observed landforms to their formative environmental drivers, via models of the active process(es). For the landforms and surface activity we have described, advances generally require additional information about the specific environmental drivers for formation and subsequent modification and/or evolution. For example, additional information about environmental drivers is needed to progress our knowledge of araneiform activity (§3). Both surface properties in araneiform-forming regions as well as time-resolved global atmospheric conditions and dynamics (including winds, clouds, and dust content) are needed to determine how and where CO_2 ice accumulates and evolves seasonally, which is essential information for constraining models of CO_2 basal sublimation and thus the scale of eruptive vents and basal erosion in araneiform terrain. Such information, combined with observations of the growth of the seasonal ice cap, would also allow for tests of

predictions of where CO_2 ice is of sufficient thickness and strength for the formation and growth of araneiforms—in the present climate or during a recent past climate.

Information needed to address the open questions outlined in previous sections (§2.3, 2.4, 3.4, 4.5, 5.3) can be gathered through a few complementary study types:

With observational data:

1) Mapping where the landforms exist and/or are active, and where they are not
2) Geomorphological measurement of the landform and its activity
3) Characterization of the timing of activity (e.g., in season, in time of day, in event duration, and identification of interannual variation)
4) Characterization of the surface (and potentially subsurface) and atmospheric environment where and when the activity occurs

With laboratory, terrestrial field analog, and physics modeling studies:

5) Identification of possible environmental drivers and investigation of scaling relationships, temporal evolution rates, and interactions between materials

Table 3 summarizes which of these areas are most needed for studies of the martian surface activities discussed above.

To acquire the observational data related to mapping and timing, continued high-resolution orbital imagery is key. The advent of HiRISE-type imaging demonstrated that the martian surface is active in the present climate, yielding a paradigm shift from the view that most of the interesting martian geologic activity occurred in the ancient past (i.e., during the Noachian and Hesperian). Continued repeat imaging of the surface with similar sub-meter resolution and illumination will enable identification of yet more surface changes, including those with slower activity rates, and potentially tie activity timing to specific seasons. Additionally, increased spatial coverage will enhance mapping studies; HiRISE has so far imaged only ~2% of Mars' surface. To aid image comparison and identification of geomorphic changes, MRO's current orbit is sun-synchronous (i.e., observations recur at specific local solar times of 3 a.m. and 3 p.m.). The ability to observe the surface at different times of day is also critical because some active processes on Mars may only occur during a specific time-of-day. Spacecraft in other orbits can view different times of day, but with other constraints such as the changing viewing conditions making change detection analysis more difficult. For example, a spacecraft in a circular orbit with inclination of 75° would drift through all times of day, ~3x per season *(NEX-*

SAG, 2015). Currently, MEx and TGO are both in elliptical orbits and can view the surface during different times of day, albeit with visible imagery at lower resolution than HiRISE. Alternatively, in situ observations can provide high-resolution and high-frequency observations throughout a Mars day, at the location of the sensors. Correlation of observations acquired by different spacecraft enables a powerful confluence of high temporal and spatial resolution information within regional/global coverage, as well as imagery over a range of wavelengths.

An additional benefit to continuation of global imaging is that interannual variations in surface activity can be tracked, yielding another way to constrain environmental drivers. In particular, observations of activity before and after the 2018 PEDE have shown that the redistribution of dust and related atmospheric effects have increased the frequency of some surface changes, such as RSL formation (*McEwen et al.*, 2021), suggesting that these activities may involve more dust than was originally hypothesized. The extensive dust activity also altered the seasonal frost cap formation/sublimation cycle and related landform activity (e.g., *Calvin and Seelos*, 2019; *Hansen et al.*, 2020).

To connect the landforms to environmental controls, we also need measurements of the environment where these landforms and activity are found. Coupling surface and subsurface compositional, thermophysical, and structural measurements with meteorological conditions over sites where a specific landform and/or activity is observed allows for a holistic analysis of the full system. From orbit, globally distributed (if not with global coverage) compositional and thermophysical information has been gleaned from spectral images through the near-infrared to thermal wavelengths. However, these datasets are limited to spatial resolutions much coarser than the scale of the activity: many are 100 m/pixel or coarser, the best is CRISM with ~20 m/pixel (*Murchie et al.*, 2007). Furthermore, many spectral datasets are only sensitive to surface exposures, so a thin layer of dust is enough to obscure the surface materials. In such areas, geologic unit mapping can provide some constraints, based on extrapolation from visible outcrops, topography, and radar analysis. In situ compositional data, as collected by the Mars rovers and landers, allow for much more detailed measurement of surface and near-subsurface properties. Coupling the in situ data with the global perspective provided through orbital observations has been key to constraining some of the interpolative analysis.

Such analysis will also be important for studies of meteorological conditions, with orbital data providing a look at global circulation and atmospheric features such as clouds. However,

existing in situ aeolian and other meteorological data are insufficient to robustly answer surface-atmosphere interaction questions because no dedicated sediment sensors were included in past missions and the meteorological instruments flown were not well accommodated and were not designed to be part of a comprehensive aeolian/meteorological experiment (*ICE-SAG*, 2019; *MEPAG*, 2020). In situ monitoring of surface atmosphere exchanges would provide key new information for constraining volatile and sediment flux models under Mars conditions (Table 4).

Table 3. A high-level summary of the types of data currently thought to be needed to advance studies of these features. As hypotheses evolve, definition of the next-needed data would likely change; in all cases more or new data could prompt unexpected new questions or analyses. The numbers/headers for the columns are discussed at the start of this section. Note that columns #1-4 are more focused on spacecraft-acquired observational data, and #5 is more focused on laboratory, terrestrial field analog, and physics modeling studies. Color coding: (Green) Extensive analysis exists or future analysis of existing data types and coverage would be sufficient to assess the broad questions; (Blue) The existing data type(s) are sufficient but increased spatial and/or temporal coverage is needed to address the broad questions, (Purple) New types of data/investigations are needed to address the broad questions.

	1: mapping	2: geomorphology	3: timing	4: environment	5: drivers/ interactions
Decimeter-scale ripples	B	G	B	P	B
Meter-scale ripples	G	B	B	P	P
Decameter-scale ripples	B	B	B	P	P
Dunes	B	G	B	P	B
Gullies	G	G	G	P	P
Dune alcoves	B	G	B	B	P
Linear gullies	B	G	G	B	B
Araneiforms	B	G	G	P	B
SPRC	G	B	B	B	B
H_2O ice layers within the MCID	G	G	G	B	P
MCID	P	G	P	P	P
Northern cap	G	G	G	P	P
Sublimation thermokarst	G	G	P	P	B
Ice Scarps	G	G	B	P	B
Patterned Ground	G	G	P	B	G
RSL	G	P	B	P	P
Avalanches	B	B	P	P	B

from rocky slopes					
Avalanches from icy slopes	G	G	B	B	B
Fallen blocks from icy slopes	G	G	G	B	B

Table 4. Some of the Mars in situ aeolian and meteorological concurrently-collected information needed to fill critical gaps in surface-atmosphere interaction and landform formation models (compiled from recent Mars community discussions and reports such as *ICE-SAG*, 2019; *MEPAG*, 2020).

Science Investigation		**In situ Measurements**
Responses Measure the surface-atmosphere fluxes of sand, dust, volatiles, heat, and momentum.	Volatiles	Absolute concentration in the atmosphere
	Dust	Local surface dust erosion and deposition rates
		Lofted dust flux and grain sizes
	Sand	Surface sand erosion and deposition rates
		Saltation profile: Number, sizes, and velocities of grains in motion, as a function of height
		Reptation flux rates and grain sizes involved
		Creep flux rates and grain sizes involved
	Heat	Temperature profile
		Net downwelling and upwelling radiation
	Momentum	Horizontal wind measurements from at least three heights – to derive surface shear stress; of frequency to determine "average" velocities and the gust velocity distribution (or 3D wind measurements)
Drivers Determine the controls on mechanisms that lead to sediment, volatiles, and heat being moved from the surface into the atmosphere and transported.	Meteorological Controls (+ winds, above)	Atmospheric temperature and pressure – to derive atmospheric density
		Atmospheric composition (including trace gases/humidity)
		Surface pressure and temperature
		Turbulence (i.e., high-frequency 3D wind measurements)
		Vortices/dust devils: number/frequency, surface shear stress, and amount of dust carried
		Overhead clouds, coverage, characteristics, and altitude
		Atmospheric electric field and electric conductivity
	Surface Controls	Grain size distribution on the nearby surface
		Surface grain properties (e.g., angularity, composition, electrostatics)
		Local surface topography, geologic-type (e.g., bedrock exposure, dust cover), and surface roughness elements
		Local surface mechanical and thermoconductive properties (e.g., cohesion, thermal inertia)

7 Mars as a "natural laboratory" for comparative planetology studies

As discussed above, Mars is the only body outside of the Earth-Moon system where we have acquired sufficient data (in time/space/type) to observe present-day activity and to investigate processes within a measured environmental and geological "system." In particular, repeat high-resolution observations have yielded many examples of present-day surface activity and these changes have or could be studied in enough detail to suggest the driving process(es) and/or influential environmental conditions. Furthermore, decades of previous work have yielded ample geologic and atmospheric contextual information and models that will greatly enhance incorporation of the broader geologic and atmospheric/climatological context within process-focused investigations. Timely acquisition of new data needed to fully constrain and calibrate a process model (§6) may also be possible because commercial and international interest in sending spacecraft (and humans) to Mars, along with Mars' relatively close proximity to Earth, suggest that access opportunities should exist for sending new spacecraft and instruments to Mars over the next decade. This may be especially true for small spacecraft that do not need a dedicated launch vehicle—which may be sufficient for targeted environmental monitoring studies.

Furthermore, Mars' atmospheric, surface, and planetary conditions are different enough from Earth's to test and stretch terrestrial study-based models, but similar enough that the terrestrial models are a reasonable starting point. As will be described, Mars' conditions often have values between those on Earth and other planetary bodies, such as Kuiper Belt Objects (KBOs) or the Moon. Mars' surface activity in modern times and through the last few billions of years can, thus, serve as a valuable and unique comparative planetology experiment for both *(1)* processes active on Earth, but under very different conditions (e.g., aeolian processes within a low density atmosphere or with much higher obliquity), and *(2)* processes not active on Earth but that are active on other planetary bodies (e.g., sublimation-dominated frost dynamics; or records of active processes without complications from recent extensive fluvial or biological activity) (also discussed in *Lapôtre et al.*, 2020).

In the following sections, we describe how Mars serves as a great (perhaps the current best) comparative planetology basis for studies of *(1)* aeolian surface processes and meteorological dynamics, *(2)* sublimation-driven geomorphic dynamics, and *(3)* planetary bodies with variable-density atmospheres. Although not covered in this review, we note that, at Mars, one can also

study both the above individual phenomena and interactions between them. There are also many additional study areas where Mars serves well as a non-Earth comparison point or extraterrestrial "laboratory" for testing and refining models, such as impact cratering rates and processes, habitability/life evolution, atmospheric dynamics, and polar/ice climate records (e.g., *Lapôtre et al.*, 2020; *I.B. Smith et al.*, 2020).

7.1 Aeolian surface processes and meteorological dynamics

Aeolian sand and dust are known to significantly influence landscape evolution and climate across the Solar System. In addition to the aeolian landforms and dynamics studied on Earth and Mars (§2):

- A few dune fields (*Greeley et al.*, 1995; *Weitz et al.*, 1994; Figure 20e), many wind streaks, and a few potential yardangs (*Greeley et al.*, 1995) have been identified on Venus, under an atmosphere 9× thicker than Earth's.
- On Saturn's moon Titan, sand produced from photochemical organic aerosols and water ice has formed vast dunes and sand seas (*Barnes et al.*, 2015; *Lorenz et al.*, 2006; *Radebaugh et al.*, 2008; Figure 20c); dust storms may also occur during equinox (*Jackson et al.*, 2020), similar to those observed on Mars (*P. Thomas and Gierasch*, 1985).
- Even on comets (*N. Thomas et al.*, 2015; Figure 20i) and icy worlds, such as Pluto (*Telfer et al.*, 2018; Figure 20a), aeolian processes within a transient, rarified atmosphere appear to have formed bedforms.

Interpretations of these landforms and processes have generally relied upon models of sediment fluxes and transport dynamics (i.e., saltation and reputation rates and profiles) derived primarily from terrestrial field and laboratory experiments, with scaling applied based on specific planetary conditions. This has led to new tests of bedform evolution models (e.g., *Claudin and Andreotti*, 2006; *Duran Vinent* et al., 2019; *Kok*, 2010; *Kok et al.*, 2012; *Parteli and Herrmann*, 2007; *Sullivan and Kok*, 2017; *Sullivan et al.*, 2020; *Vaz et al.*, 2017) and proposal of a new scaling relationship to predict ripple equilibrium wavelength (e.g., *Lapôtre et al.*, 2016; 2017; 2018; 2021) after Earth conditions-based model predictions were found to be inconsistent with bedforms observed on another planet.

Further study of martian aeolian and other meteorological systems, and how conditions drive surface activity, will enable more detailed testing and refinement of surface-atmosphere

interaction process models. In particular, in situ "field" measurements of martian atmospheric boundary layer dynamics driving sand/dust and volatile transport would provide novel calibration data for models and wind-tunnel experiments within an environment with a substantially lower impact threshold than fluid threshold (*Kok*, 2010). Such "ground truth" is needed to advance a cross-planet model to describe sand and dust lofting and transport, including helping to discriminate between models such as fluid-dominated (e.g,, *Bagnold*, 1941; *Shao and Lu*, 2000) or impact-dominated (e.g., *Kok and Renno*, 2009; *Sullivan and Kok*, 2017) transport or coarse grain motion via direct-drag or impact-driven creep (e.g., *Baker et al*., 2018a, *Silvestro et al.*, 2020).

Another model presently untested under extraterrestrial conditions is the one used to estimate turbulent eddy fluxes (which result in the exchange of energy, momentum, and quantities like dust, water, and other chemical species between the surface and atmosphere). On Earth, turbulent fluxes can be directly calculated from correlated, high frequency measurements of the 3D wind components and the quantity of interest; such fluxes are also related to large-scale (and more easily measured) quantities such as the vertical gradient of temperature and of the horizontal wind (i.e., the wind shear) (*Businger and Yaglom*, 1971; *Businger et al.*, 1967; *Monin and Obukhov*, 1954), with ample testing and calibration of the physical model through terrestrial field and laboratory studies. These relationships are assumed in planetary studies but have never been shown to extend to those environments despite generally being far outside of terrestrial conditions (e.g., Mars has an extremely stable nocturnal inversion and unstable afternoon convective layer). New in situ martian meteorological measurements would enable validation and calibration of this theory within a wider range of atmospheric conditions.

Mars is already used as the comparative planetology basis for some studies, due to its low atmospheric density. For example, the threshold curve under low-density gas conditions derived for Mars analog conditions in the MARSWIT (*Greeley and Iversen*, 1985) has also been used to model aeolian-type transport resulting from jetting on comets (*Cheng et al.*, 2013). Dune-like patterns on the surface of comet 67P/Churyumov-Gerasimenko (*N. Thomas et al.*, 2015) have been suggested to result from thermal winds, although the process involves outgassing from cometary jets feeding a rarefied atmosphere rather than from atmospherically driven winds as on the surfaces of Mars and Titan (*Jia et al.*, 2017). In imaging data from the New Horizons mission, Pluto was shown to have 0.4–1 km-wavelength bedform-like morphologies (*Stern et al.*,

2015). Proposed to be aeolian dunes (*Telfer et al.*, 2018), a minimum wind shear required for saltation was estimated based on work performed in the MARSWIT that separated Reynolds number and interparticle cohesion effects (*Iversen and White*, 1982). The important point of analogy here is the substantially lower impact threshold than fluid threshold, as discussed in §2.2.1.

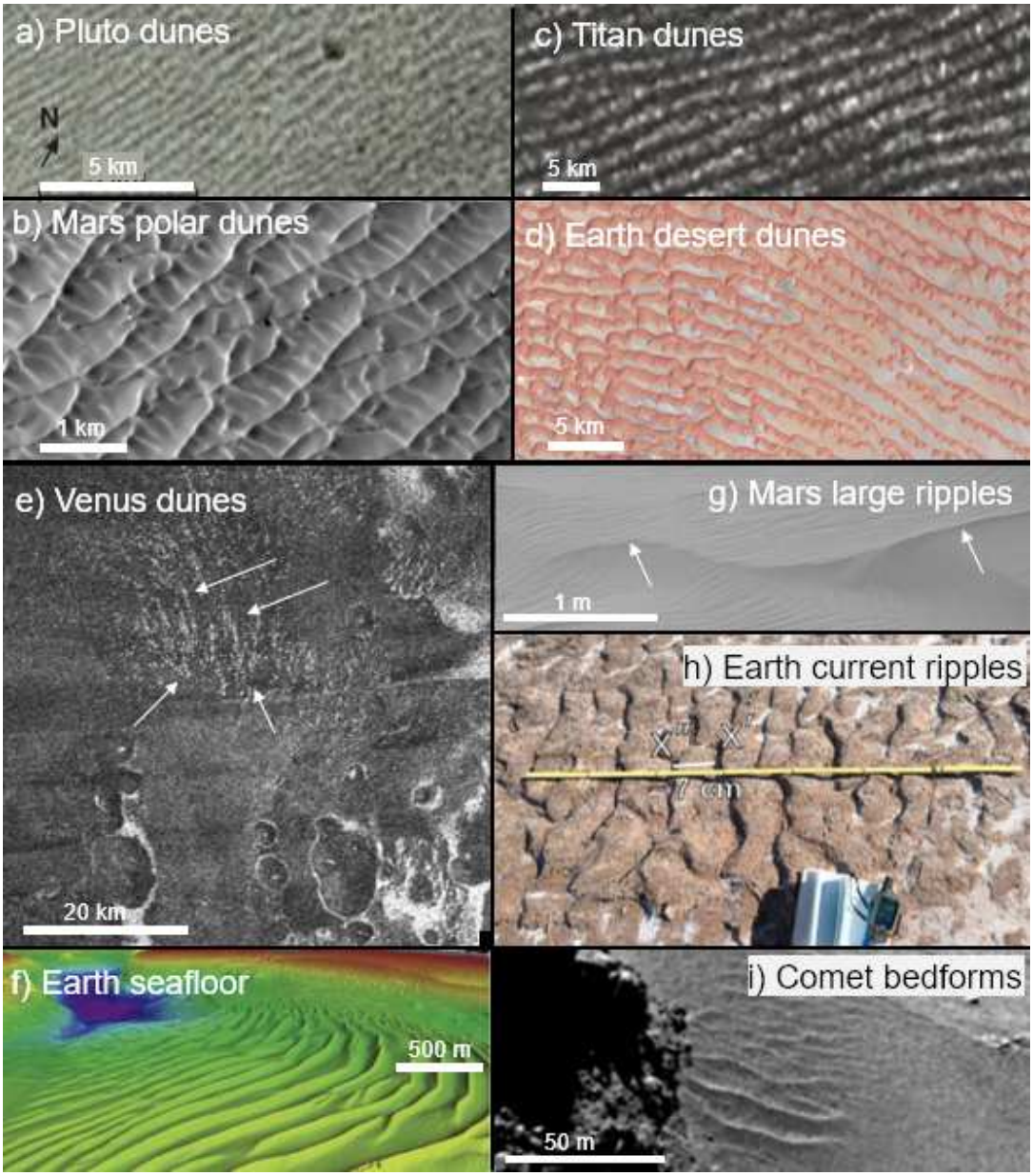

Figure 20. Examples of bedforms on different planetary bodies: (*a-d*) Planetary features with remarkable geomorphic similarities, leading to hypotheses of aeolian dune fields. (*e-j*) Examples from the diverse suite of bedforms found on other bodies, which may be more analogous to terrestrial subaqueous bedforms than subaerial ones (proposed terrestrial analogs are shown in (*f*

and *h*), for Venus and Mars/comet, respectively). Rough scale bars are included, but distances are not exact because images are generally not orthorectified. Images were selected/adapted based on: (*a*) *Telfer et al.*, 2018: New Horizons color-composite MVIC images, (*b*) *Diniega et al.*, 2017: HiRISE image PSP_007115_2600, (*c*) *Radebaugh et al.*, 2010: Cassini synthetic aperture radar (SAR) image, (*d*) Landsat image of Rub' al Khali in the Arabian peninsula (https://earthobservatory.nasa.gov/blogs/earthmatters/2012/11/02/dune-gallery/), (*e*) *Diniega et al.*, 2017: Magellan SAR image of Menat Undae dune field/NASA Photojournal PIA00483, (*f*) *Neakrase et al.*, 2017: sand waves in San Francisco Bight (from Fig. 6), (*g, h*) *Lapôtre et al.*, 2018: MSL Mastcam image acquired in Sol 1221, image of current ripples from dry riverbed in Death Valley, CA (from Fig. 2), (*i*) *Thomas et al.*, 2015: Rosetta image NAC_2014-09-18T00.33.01.377Z_ID10_1397549800_F22.

7.2 Sublimation-driven geomorphic dynamics

As discussed above, each martian fall/winter CO_2 frost and ice are deposited in a thick seasonal layer and in the winter/spring hemisphere this layer sublimes. Mars has lower gravity and a lower pressure and temperature environment than Earth, causing sublimation processes to differ from terrestrial analogs, including laboratory analogs. Mars' atmosphere is in vapor equilibrium with surface CO_2 frost/ice (*Leighton and Murray*, 1966), thus Mars has an environment closer to those of Triton, Pluto, and possibly other Kuiper Belt Objects (*Ingersoll*, 1990; *Owen et al.*, 1993), rather than terrestrial and laboratory analogs. For example, no large-scale sublimation dynamics naturally occur on Earth, and within laboratory studies we cannot replicate low gravity over timescales relevant for sublimation.

Sublimation is thought to be the main-driver forming a range of depressions or pits on Mars, including SPRC pitting (§4.1.1), icy scarps (§4.3.1), and scalloped depressions (§4.3). Sublimation has also been linked to the formation of other (non-active) depressions which have not been discussed above, including pitted terrain in and around impact craters (*Boyce et al.*, 2012; *Tornabene et al.*, 2012), crenulated and labyrinthine pitted surfaces of martian glaciers (e.g. *Levy et al.*, 2009a*; Mangold*, 2003), and dissected latitude dependent mantle (*Milliken et al.*, 2003; *Mustard et al.*, 2001; *Soare et al.*, 2017). These different features are proposed to form due to sublimation from volatile reservoirs of different sizes/forms/ages, and vastly different sublimation rates. Thus, studies of these features on Mars enable discrimination between different proposed models and identification of key geomorphological or environmental signatures for separating features that likely formed through slightly different processes, within different environments, and/or over very different timescales.

Mangold (2011) provides a detailed review of sublimation landforms in the Solar System, and here we add new results with the additional perspective of using Mars as an analog. Some sublimation-generated depressions on Mars that have already been compared to depressions on the surfaces of other bodies in the Solar System include the following:

- Hollows on Mercury (e.g., *Blewett et al.*, 2011; *R.J. Thomas et al.*, 2014) (Figure 21b) which are thought to be due to volatile-loss or sublimation of sulfur-related compounds, likely sulfides (e.g., *Bennett et al.*, 2016) and analogies have been drawn to martian swiss cheese terrain (§4.1.1; Figure 21a).
- Pitted surfaces have been discovered on asteroids, notably pitted crater floors on Vesta *(Denevi et al.*, 2012) and Ceres (*Sizemore et al.*, 2017; 2019) which are remarkably similar to pitted terrain found in craters on Mars (*Boyce et al.*, 2012; *Tornabene et al.*, 2012). Additionally, pitted areas and scarps on outer Solar System moons have been grouped with Mars polar features as evidence of sublimation degradation (*Moore et al.*, 1996).
- Pitted terrains on Pluto (Figure 21c) that are thought to represent erosion from sublimation-driven winds of the surface of nitrogen ice and possibly methane ice (*Buhler and Ingersoll*, 2018; *Moores et al.*, 2017). Similar terrains are thought to exist on other Kuiper Belt Objects, and the origins of flat-floored pits on Arrokoth remain mysterious (*Schenk et al.*, 2020). Bladed terrains on Pluto are also thought to derive from sublimation (*Moores et al.*, 2017).
- Pitted surfaces found on comets (e.g., *Sunshine et al.*, 2016). Recent exploration of 67P Churyumov–Gerasimenko by Rosetta maintains that these pits, which span a range of sizes, grow primarily via sublimation (e.g., tens to hundreds of meters-wide pits: *Vincent et al.* (2015), meters-wide pits: *Birch et al.* (2017)).

On Mars, sublimation is thought to have an important role to play in initiating and/or enhancing mass wasting over sandy slopes (§3.2.1-2, 3.3.1, 5.2) and rocky slopes (§3.2.1, 5.2) (Figure 21d). Martian mass-wasting features have been proposed to form useful analogies for:

- Gully-like landforms identified on Mercury (*Malliband et al.*, 2019) and Vesta (*Krohn et al.*, 2014; *Scully et al.*, 2015) (Figure 21e,f), potentially related to sublimation of sulfur-compounds and water, respectively.
- Downslope features that have been observed on Helene, one of Saturn's Trojan moons, whose formation has been ascribed to sublimation (*Umurhan et al.*, 2016) (Figure 21g).

Furthermore, it is likely that closer inspection of other planetary bodies will reveal further examples of sublimation-driven mass-wasting processes.

In general, sublimation and related processes drive dust and other contaminants up to the atmosphere or, in the case of comets, into their coma. Escaping pressurized gas from sublimation at the base of the CO_2 seasonal ice cap on Mars erodes araneiforms (*Hansen et al.*, 2010; *Kieffer*, 2007; *Piqueux et al.*, 2003; *Portyankina et al.*, 2017), radially organized and /or dendritic channels (*Mc Keown et al.*, 2017) initially dubbed "spiders," and deposits material across the surface (*N. Thomas et al.*, 2010). These jets of gas, whose origin is via basal sublimation and the solid state greenhouse effect (§3.1; *Kieffer*, 2007), and the patterns/rates of material they spew out could be useful analogues for the following:

- Sublimation processes proposed to cause to global-scale contrasting albedo regions on Iapetus and Ganymede (*Giese et al.*, 2008; *Prockter et al.*, 1998; *Spencer and Denk*, 2010).
- CO_2 ice signatures found on the trailing hemispheres of the Uranian satellites (*Cartwright et al.*, 2015; *Grundy*, 2003; *Grundy et al.*, 2006), notably visible as a bright deposit inside Wunda Crater on Umbriel (*Sori et al.*, 2017). Severe sublimation of CO_2-ices is thought to explain the pinnacle terrain on Callisto (*Howard et al.*, 2008; *White et al.*, 2016) (Figure 21h).
- Solar-driven jets of materials found on other bodies. The solar-driven theory was actually proposed to explain plumes on Triton (*Soderblom et al.*, 1990) before it was applied to Mars' geysers (*Kieffer et al.*, 2006), although later Triton observations suggested a cryovolcanic origin might instead be responsible (*Waite et al.*, 2017).

Additionally, interactions between wind and sublimation dynamics can be explored on Mars. For example, a "sublimation wave" model of dynamics at the interface between an icy substrate and a turbulent boundary layer flow may explain certain icy landform periodicities on Mars and Earth (*Bordiec et al.*, 2020). Bodies such as Pluto, Ceres, and Jovian and Saturnian icy moons are also hypothesized to have surface sublimation and winds, so similar dynamics could be expected there (*Bordiec et al.*, 2020).

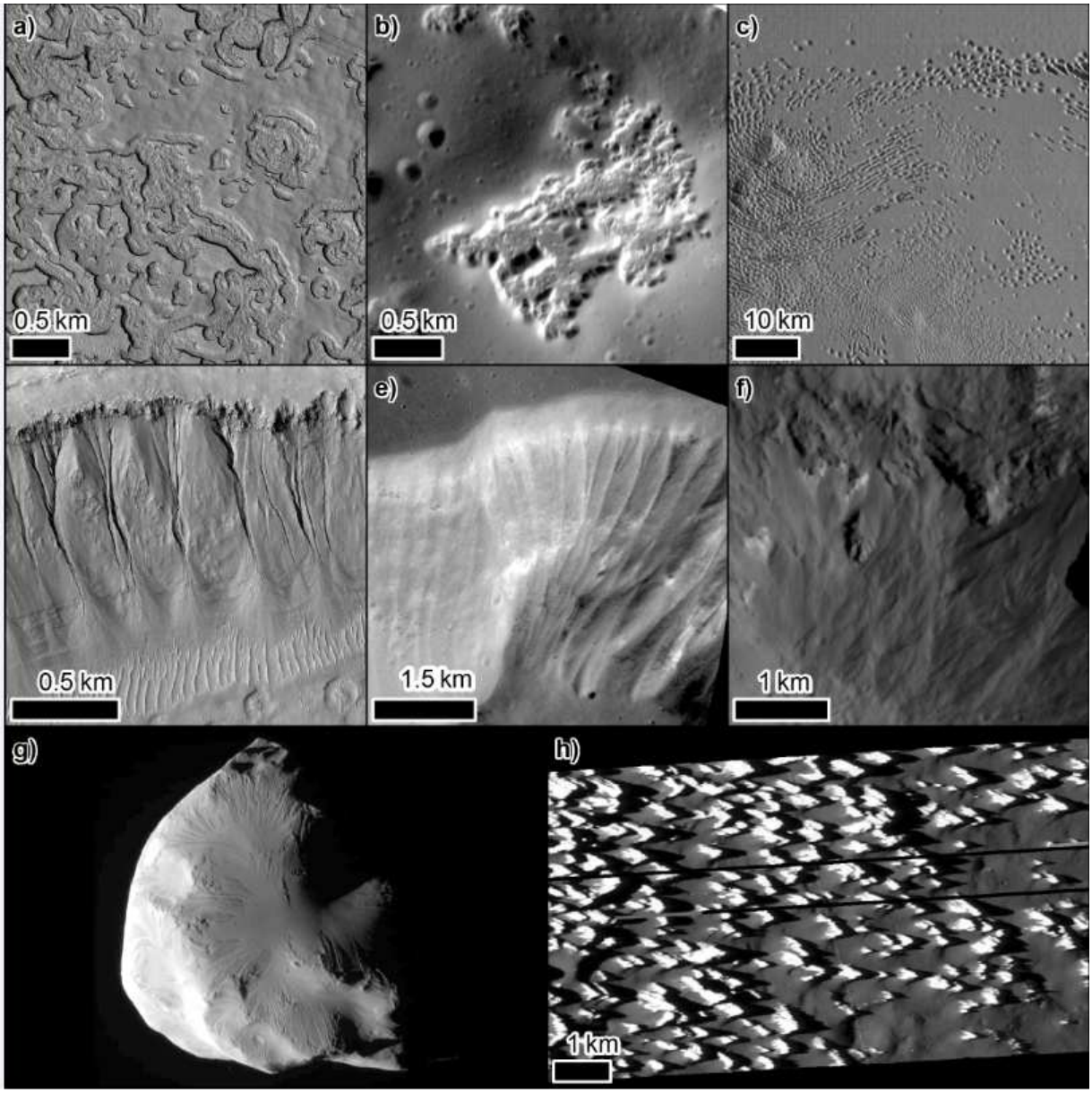

Figure 21. Geomorphic features on multiple planetary bodies, thought to be formed through surface frost sublimation and potentially analogous to features on Mars. *(a)* Swiss cheese terrain on Mars HiRISE image ESP_057828_0930. *(b)* Hollows on Mercury in Scarlatti impact basin, MDIS NAC image EN1051805374M. *(c)* Pits on Pluto, New Horizons LORRI image 0299179742. *(d)* Gullies on Mars, HiRISE image. *(e)* Mass wasting gullies on Mercury in Nathair Facula, MDIS NAC image EN1059620367M. *(f)* Mass wasting gullies on Vesta in Cornelia Crater, DAWN Framing Camera image FC21B0025747. *(g)* Image of Saturn's Moon Helene taken by Cassini-Huygens ISS NA camera. Lit terrain is on the leading hemisphere of Helene measuring ~33 km across and North is down. *(h)* Pinnacle terrain on Callisto, Galileo image PICNO (Picture number) 30C0003. Image processing for MDIS and Galileo was performed using ISIS3 via the U.S. Geological Survey PILOT and POW systems.

In addition to sublimation, studies of the present-day accumulation and evolution of frost and ice on Mars may provide analog information about the types and interactions of frost and ice on other bodies. For example, one model of methane snow on Pluto (*Witzke*, 2015; https://www.nasa.gov/feature/methane–snow–on–pluto–s–peaks; Figure 22) indicates that it forms due to a circulation-induced high-altitude enrichment of gaseous methane, a process different from those forming high-altitude snowpacks on Earth (*Bertrand et al.*, 2020). Comparisons with H_2O and CO_2 snow on Mars may provide a better comparative planetology starting point to understand precipitation and volatile transport on planets and dwarf planets with tenuous atmospheres. The surface pressure of the martian atmosphere is 2–3 orders of magnitude less than that of the Earth, and Pluto's atmosphere is another ~3 orders of magnitude lower, providing a large physical range for future modeling that applies to a full suite of planetary atmospheres in the Solar System and elsewhere. Laboratory studies of H_2O and CO_2 ice (e.g., *Chinnery et al.*, 2018; *Kaufmann and Hagermann*, 2017; *Pommerol et al.*, 2019; *Portyankina et al.*, 2019; *Yoldi et al.*, 2021), as well as how evolution of such materials is altered through interaction between the ices and dust, coupled with Mars ice and environment observations provides the current best route for formulating and calibrating models of these strange ices under extraterrestrial conditions. Even if not providing a direct analog, study of martian ices may also help ground truth models and demonstrate how to interpret spacecraft observations and connect them with terrestrial experiments involving exotic ices.

Finally, while not directly related to present-day frost accumulation/sublimation or observable activity, the creep of martian glaciers also likely presents a useful analog for studies of outer Solar System bodies. The balance between sublimation/ablation, deposition, and flow rates is thought to be significantly different in martian vs. terrestrial glaciers. For example, due to an overall lower surface temperature, water-ice glaciers on Mars exhibit different dynamics from most terrestrial glaciers, i.e., without basal melting or basal sliding (*Head and Marchant*, 2003; *Marchant et al.*, 1993); there may be evidence of past CO_2 glaciers (*Kreslavsky and Head*, 2011). Both valley and piedmont glaciers on Pluto have been identified in the region of Sputnik Planitia (*Moore et al.*, 2016). Some show evidence of bulk flow, with basement material or nunatuks protruding above the mobile material (*Stern et al.*, 2015).

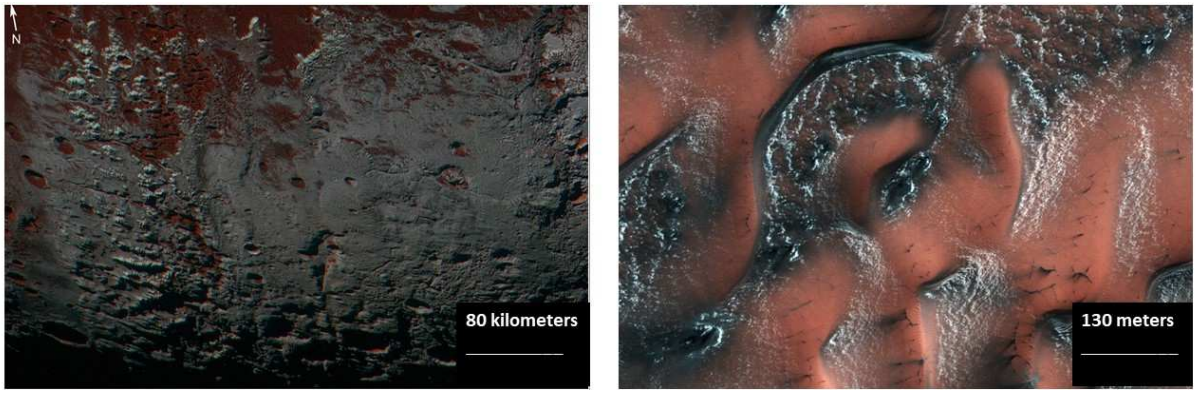

Figure 22. Snow on Pluto and Mars. The image on the left from the Multispectral Visible Imaging Camera on the New Horizons spacecraft shows possible methane snow on mountains in the southern hemisphere of Pluto. The image on the right is a false color image from the High Resolution Imaging Science Experiment (HiRISE) camera on NASA's Mars Reconnaissance Orbiter shows CO_2 frost on martian dunes at a northern latitude of 76° (north is down). Picture credits left: *NASA/JHU APL/SwRI* (discussed in NASA press-release 03-03-2016, https://www.nasa.gov/feature/methane-snow-on-pluto-s-peaks). Right: NASA/JPL/UA, HiRISE ESP_050703_2560.

7.3 Planetary bodies with variable-density atmospheres

Although in this study we primarily focused on known or hypothesized present-day surface activity and related landforms, as discussed above, studies of the present-day Mars provides a key to interpret the archive of past Mars' surface processes and climate conditions. In particular, both aeolian processes and sublimation dynamics will be influenced by atmospheric density, which has varied on Mars over seasonal to much longer timescales. Studies of observable surface activities in the present (including variations in activity rates correlated to seasonal or interannual environmental variations) enables testing of models that then are extrapolated back to past martian climates, or to other bodies that may experience analogous cyclic variations and/or atmospheric collapse.

As discussed in §3.1, the CO_2 atmosphere of Mars is in vapor pressure equilibrium with surface ice; seasonally CO_2 sublimes and condenses, changing the atmospheric density by >25% in the present climate (e.g., *Forget et al.*, 1998; 1999; *Hartogh et al.*, 2005; *Leighton and Murray*, 1966; *Pollack et al.*, 1990; 1993). The dynamics of this process modulate the global circulation and drive local sublimation winds, such as katabatic winds that are thought to play an important role in the formation of polar troughs (*Spiga and Smith*, 2018). Similar surface-atmosphere processes act on other planetary bodies where the atmosphere is in vapor pressure equilibrium with surface ice, such as on Triton, Pluto, and KBOs (*Bertrand et al.,* 2020; *Hansen*

et al., 2018; *Zalucha and Michaels*, 2013). Thus, Mars' processes and climate cycles may present a good analog for interpreting the integrative geomorphological result of atmosphere-surface processes on these bodies, including sublimation-driven formation of surface features and aeolian-driven processes (*Moore et al.*, 2017; *Young*, 2012).

Due to cycles in various orbital parameters (such as obliquity), the Mars atmospheric density may cycle through a range of 1–12 mbar over thousands to millions of years timescales (*Buhler et al.*, 2020; *Manning et al.*, 2019). Derivation of present-day martian surface activity models that quantitatively connect landform morphologies to driving environmental conditions will enable improved interpretation of relict features and reduce uncertainty when extrapolating activity models through past Mars climates. Such developments will also provide a testable basis for generation of similar models on other bodies that also experience large, cyclic changes in atmospheric density, such as on Pluto (*Betrand et al.*, 2018; *Forget et al.*, 2017; *Hansen and Paige*, 1996) and Triton (*Hansen and Paige*, 1992; *Trafton*, 1984; *Yelle et al.*, 1995). As Earth's atmosphere has not gone through comparable large swings in atmospheric density during the portion of Earth's history when most of the Earth's observable rock record was formed, Mars provides important "ground truth" for this type of extrapolative analysis and integration of predicted geologic records through different atmospheric pressures.

For example, on Mars, both ancient surface and stratigraphic features and modern active processes can be directly observed and measured. This enables models of sedimentary processes to be investigated through different climate conditions. In particular, the morphologies of large martian ripples have been proposed to provide a way to constrain atmospheric density changes within Mars' climate history (*Lapôtre et al.*, 2016). As previously discussed (§2.1.3), the wavelength of large martian ripples appears to be a function of atmospheric density (*Lapôtre et al.*, 2016; *Lorenz et al.*, 2014). The wavelength of old ripples can be read in inactive ripple fields, but also within the cross-stratification left behind by bedforms (e.g., *Rubin*, 1987; *Rubin and Carter*, 2006). Thus, provided that bedform dimensions can be extrapolated from the martian aeolian record (e.g., *Banham et al.*, 2018; *Grotzinger et al.*, 2005; *Lapôtre et al.*, 2016) and with a mechanistic understanding of how atmospheric density controls bedform size (e.g., through kinematic viscosity, specific sediment density, and possibly wind shear velocity; *Lapôtre et al.*, 2016; 2017), one should be able to reconstruct the history of atmospheric density from the aeolian rock record. Such results, especially coupled with terrestrial-based sedimentary process

models, could advance studies of analogous sedimentary deposits on other planetary bodies and enable even more climatological and geologic history to be interpreted from limited observations.

Another example is about how erosive potential of basal sublimation from CO_2 ice slabs is affected by the thickness of the seasonal ice layer or insolation conditions, leading to the formation of araneiforms. As discussed in §3.3.2, some studies of these features suggested that araneiforms may be active at very slow rates (*Piqueux and Christensen*, 2008), but repeat high-resolution imaging of these features has not yielded any discernible changes in topography over the last decade. Based on lab experiments of the CO_2 ice sublimation activity over granular materials, it has instead been proposed that some of the araneiforms (especially the largest and those diplaying a non-radial network) may be relicts of a past climate when the frost depth or insolation amount was different, leading to more energetic sublimation (*Mc Keown et al.*, 2021). Determination of the environmental controls on the basal sublimation rates and resultant erosion potential of the escaping gas would enable improved interpretation of the ice layer thickness/strength needed to form these features. Should the needed ice layer be more than those forming in the present climate, then the araneiforms could be interpreted as direct records of past wintertime conditions. Such results provide constraints on models of the pressures attained via basal sublimation—a distinctively non-terrestrial process that would be applicable towards studies of jets and substrate erosion on other bodies.

In parallel, but out of phase with variable density atmospheres, the surface deposition of meteoric ice will result in layered and likely stratified volatile deposits with impurities. On Mars, impurities likely include dust, lithic fragments from volcanic eruptions or ejecta, fine salt grains, trapped gasses, and isotopologues (*ICE-SAG*, 2019; *I.B. Smith et al.*, 2020). Mars is not the only planetary body to experience partial atmospheric collapse (*Soto et al.*, 2015). Pluto (*Bertrand et al.*, 2018; 2019; *Hansen and Paige*, 1996; *Olkin et al.*, 2015) and Titan (*Lorenz et al.*, 1997) likewise have strong seasonal atmospheric cycles (lasting hundreds of Earth years) and orbital variations that could cause similar ice layering as is found on Mars, and atmospheric collapse has been proposed for tidally locked planets around TRAPPIST-1 (*Turbot et al.*, 2018). Earth, with anthropomorphic influences, abundant biology, and liquid phases, does not provide a good analog for such layered ice deposits or climate models.

8 Lessons learned from planetary geomorphological studies

Based on recurrent challenges and some of the key science advancements within studies of martian present-day activity, we identify pitfalls and strategies that may benefit future planetary and terrestrial geomorphological studies. First, a key lesson is that geomorphological similarity to terrestrial landforms may present a good starting point for a hypothesis of similar formation process and driving environmental conditions, but geomorphological similarity alone is not sufficient to conclude parallel evolution. One needs to consider other observations and datasets to determine if there is "system"-level consistency with processes or environmental conditions similar to those on the Earth (e.g., the timing of activity, geologic context, compositional constraints, and contemporaneous environmental characterization). This applies both to comparisons between features on the same planet (e.g., martian gullies (§3.2.1) versus dune alcoves (§3.2.2)) and to comparisons between features on different planets (e.g., gullies (§3.2.1) on Mars, Mercury, and Vesta (§7.2)).

A second key lesson is that many interactions and controls are nonlinear, so there are often complications both in scaling an analog process or landform under new environmental conditions and in trying to separate out the influences of multiple processes on a planetary surface. For the first, laboratory/field experiments and modeling studies are crucial for testing proposed relationships and even seeing what the process looks like under exotic conditions; for example, due to the low surface pressure, liquid water would flow and boil on the present-day martian surface, creating small "flow" morphologies different from those observed on Earth (*Herny et al.*, 2019; *Massé et al.*, 2016; *Raack et al.*, 2017); until these experiments were run, levitating sand pellets were not expected or taken into account in theories. For the second, looking at a range of activity and landform types across a planetary surface, as well as mapping where a process seems to be active and where it appears to not be active (e.g., Figure 2), can help detangle processes and driving environmental conditions.

A third key lesson is that long-term observation of change is needed to fully characterize a process and its expression and rate(s), as moderated by changes in driving environmental conditions. Activity levels can vary dramatically from year to year (e.g., as is currently being investigated with the 2018 Mars PEDE).

Finally, to increase the science value of new observations and enable a holistic look at Mars present-day phenomena, the international space agencies and Mars exploration programs along

with an active and connected Mars science community have been instrumental in enabling strategic linkages between observations, especially between orbital and in situ assets. Having such community communication/coordination and data accessibility is clearly key for the "system" science generally involved in investigations of geomorphological processes. Related, a research and analysis program that supports both data analysis and fundamental research studies helps scientists collaborate and combine different types of study (e.g., Mars' "natural laboratory" observations, laboratory/wind tunnel experiments, field analog studies, and physical/numerical models) to robustly test and calibrate models describing the observed activity, and then extrapolate from observed conditions to past or more exotic environments. As such work is inherently cross-disciplinary, cross-target, and diverse in scope, it is critical also that the community foster an interdisciplinary, diverse, equitable, inclusive, and accessible environment so that a wide range of people and perspectives can interact, communicate, and then contribute towards understanding the active surface processes and improve science advancement.

9 Acknowledgements

We thank our reviewers, Clémence Herny and Mackenzie Day, for their very thorough reads and thoughtful critiques and suggestions. The work by JPL authors (SD, BB, SP) was carried out at the Jet Propulsion Laboratory, California Institute of Technology, under a contract with the National Aeronautics and Space Administration (80NM0018D0004). MC wishes to thank NASA Mars Data Analysis Program grant 80NSSC20K1066. ML wishes to thank NASA Solar System Workings Program grant 80NSSC20K0145. SJC is grateful to the French Space Agency CNES for funding her HiRISE and CaSSIS related work. Some manuscript content was derived based on personal communications with terrestrial and planetary aeolian community members and we appreciate the insights and information; in particular, Scot Rafkin (SwRI) assisted with the description of important untested models of meteorologic dynamics. Finally, we thank the many space/Earth/physical sciences agencies' staff, planetary mission and instrument teams, and researchers who have enabled the observations, analysis, and community collaborations that contribute towards studies of Mars as an active and connected system. This includes, but is not limited to, the spacecraft and instrument engineering teams for the successful completion and operation of MRO and TGO/CaSSIS. CaSSIS is a project of the University of Bern funded through the Swiss Space Office via ESA's PRODEX programme; the CaSSIS instrument hardware development was also supported by the Italian Space Agency (ASI) (ASI-INAF

agreement no. I/018/12/0), INAF/ Astronomical Observatory of Padova, and the Space Research Center (CBK) in Warsaw.

10 References

Abotalib, A.Z., Heggy, E., 2019. A deep groundwater origin for recurring slope lineae on Mars. *Nature Geoscience*, **12**, 235–241, doi:10.1038/s41561-019-0327-5.

Achilles, C., Downs, R.T., Ming, D.W., Rampe, E.B., Morris, R.V., Treiman, A.H., Morrison, S.M., Blake, D.F., Vaniman, D.T., Ewing, R.C., Chipera, S.J., 2017. Mineralogy of an active eolian sediment from the Namib Dune, Gale Crater, Mars. *Journal of Geophysical Research: Planets*, **122**, 2344–2361, doi:10.1002/2017JE005262.

Anderson, D., Gatto, L.W., Ugolini, F., 1973. An examination of Mariner 6 and 7 imagery for evidence of permafrost terrain on Mars. In: Sanger, F.G. (Ed.), *Permafrost: Second International Conference*, 499–508.

Andreotti, B., Claudin, P., Douady, S., 2002. Selection of dune shapes and velocities Part 1: Dynamics of sand, wind and barchans. *Eur. Phys. J.*, **B28**, 321–339.

Andreotti, B., Claudin, P., Pouliquen, O. 2006. Aeolian sand ripples: Experimental study of fully developed states. *Physical Review Letters*, **96**, 028001, doi:10.1103/PhysRevLett.96.028001

Appéré, T., Schmitt, B., Langevin, Y., Douté, S., Pommerol, A., Forget, F., Spiga, A., Gondet, B., Bibring, J.-P., 2011. Winter and spring evolution of northern seasonal deposits on Mars from OMEGA on Mars Express. *Journal of Geophysical Research: Planets*, **116**(E5), E05001, doi:10.1029/2010JE003762.

Arvidson, R.E., Iagnemma, K.D., Maimone, M., Fraeman, A.A., Zhou, F., Heverly, M.C., Bellutta, P., Rubin, D., Stein, N.T., Grotzinger, J.P., Vasavada, A.R., 2017. Mars Science Laboratory Curiosity rover megaripple crossings up to sol 710 in Gale crater. *Journal of Field Robotics*, **34**(3), 495–518, doi:10.1002/rob.21647.

Atwood-Stone, C., McEwen, A.S., 2013. Avalanche slope angles in low–gravity environments from active martian sand dunes. *Geophysical Research Letters*, **40**, 2929–2934, doi:10.1002/grl.50586.

Ayoub, F., Avouac, J.-P., Newman, C., Richardson, M., Lucas, A., Leprince, S., Bridges, N., 2014. Threshold for sand mobility on Mars calibrated from seasonal variations of sand flux. *Nature Communications*, **5**, 5096, doi:10.1038/ncomms6096.

Bagnold, R.A., 1936. The movement of desert sand. *Proceedings of the Royal Society of London. Series A-Mathematical and Physical Sciences*, **157**(892), 594–620.

Bagnold, R.A., 1937. The transport of sand by wind. *The Geographical Journal,* **89**(5), 409–438.

Bagnold, R.A., 1941. *The Physics of Blown Sand and Desert Dunes*. Methuen: London

Baker, M.M., Newman, C.E., Lapôtre, M.G.A., Sullivan, R., Bridges, N.T., Lewis, K.W., 2018a. Coarse sediment transport in the modern martian environment. *Journal of Geophysical Research: Planets*, **123**(6), 1380–1394, doi:10.1002/2017JE005513.

Baker, M.M., Lapôtre, M.G., Minitti, M.E., Newman, C.E., Sullivan, R., Weitz, C.M., Rubin, D.M., Vasavada, A.R., Bridges, N.T., Lewis, K.W., 2018b. The Bagnold dunes in southern

summer: Active sediment transport on Mars observed by the Curiosity rover. *Geophysical Research Letters*, **45**(17), 8853–8863, doi:10.1029/2018GL079040.

Balme, M., Greeley, R., 2006. Dust devils on Earth and Mars. *Review of Geophysics*, **44**(3), RG3003, doi:10.1029/2005RG000188.

Balme, M., Berman, D.C., Bourke, M.C., Zimbelman, J.R., 2008. Transverse aeolian ridges (TARs) on Mars. *Geomorphology*, **101**, 703–720, doi:10.1016/j.geomorph.2008.03.011.

Balme, M.R., Gallagher, C.J., Page, D.P., Murray, J.B., 2009. Sorted stone circles in Elysium Planitia, Mars: Implications for recent martian climate. *Icarus*, **200**, 30–38, doi:10.1016/j.icarus.2008.11.010.

Banfield, D., Spiga, A., Newman, C., 2020. The atmosphere of Mars as observed by InSight. *Nature Geoscience*, **13**, 190–198, doi:10.1038/s41561-020-0534-0.

Banham, S.G., Gupta, S., Rubin, D.M., Watkins, J.A., Sumner, D.Y., Edgett, K.S., Grotzinger, J.P., Lewis, K.W., Edgar, L.A., Stack-Morgan, K.M., Barnes, R., 2018. Ancient martian aeolian processes and palaeomorphology reconstructed from the Stimson formation on the lower slope of Aeolis Mons, Gale crater, Mars. *Sedimentology*, **65** (4), 993–1042, doi:10.1111/sed.12469.

Banks, M.E., Byrne, S., Galla, K., McEwen, A.S., Bray, V.J., Dundas, C.M., Fishbaugh, K.E., Herkenhoff, K.E., Murray, B.C., 2010. Crater population and resurfacing of the Martian north polar layered deposits. *Journal of Geophysical Research*, 115, E08006, doi:10.1029/2009JE003523.

Banks, M.E., Geissler, P.E., Bridges, N.T., Russell, P., Silvestro, S., Chojnacki, M., Zimbelman, J.R., Delamere, W.A., 2015. Emerging global trends in aeolian bedform mobility on Mars. Presented at *Fourth Int. Planetary Dunes Workshop*, Ab. #8036.

Banks, M.E., Fenton, L.K., Bridges, N.T., Geissler, P.E., Chojnacki, M., Runyon, K.D., Silvestro, S., Zimbelman, J.R., 2018. Patterns in mobility and modification of middle- and high-latitude southern hemisphere dunes on Mars. *Journal of Geophysical Research: Planets*, doi:10.1029/2018JE005747.

Baratoux, D., Mangold, N., Arnalds, O., Bardintzeff, J.M., Platevoet, B., Grégoire, M. Pinet, P., 2011. Volcanic sands of Iceland-Diverse origins of aeolian sand deposits revealed at Dyngjusandur and Lambahraun. *Earth Surface Processes and Landforms*, **36**(13), 1789–1808, doi:10.1002/esp.2201.

Barnes, J.W., Lorenz, R.D., Radebaugh, J., Hayes, A.G., Arnold, K., Chandler, C., 2015. Production and global transport of Titan's sand particles. *Planetary Science*, **4** (1), 1–19, doi:10.1186/s13535-015-0004-y.

Barrett, A.M., Balme, M.R., Patel, M.R., Hagermann, A., 2017. Clastic patterned ground in Lomonosov crater, Mars: Examining fracture controlled formation mechanisms. *Icarus*, **295**, 125–139, doi:10.1016/j.icarus.2017.06.008.

Bauer, B.O., Davidson-Arnott, R.G.D., Hesp, P.A., Namikas, S.L., Ollerhead, J., Walker, I.J., 2009. Aeolian sediment transport on a beach: Surface moisture, wind fetch, and mean transport. *Geomorphology*, **105**(1-2), 106–116, doi:10.1016/j.geomorph.2008.02.016.

Becerra, P., Byrne, S., Brown, A.J., 2015. Transient bright "halos" on the south polar residual cap of Mars: implications for mass-balance. *Icarus*, **251**, 211–225, doi:10.1016/j.icarus.2014.04.050.

Becerra, P., Conway, S., Thomas, N., The HiRISE team, 2020. Avalanches of the martian north polar cap. Presented at *EGU General Assembly 2020*, 22331.

Bennett, C.J., McLain, J.L., Sarantos, M., Gann, R.D., DeSimone, A., Orlando, T.M., 2016. Investigating potential sources of Mercury's exospheric Calcium: Photon–stimulated desorption of Calcium Sulfide: PSD OF CAS. *Journal of Geophysical Research: Planets*, **121**, 137–146, doi:10.1002/2015JE004966.

Benson, J. L., Kass, D. M., Kleinböhl, A. 2011. Mars' north polar hood as observed by the Mars Climate Sounder. *Journal of Geophysical Research*, **116**, E03008, doi:10.1029/2010JE003693.

Berger, J.A., Schmidt, M.E., Gellert, R., Campbell, J.L., Boyd, N.I., Elliott, B.E., Fisk, M.R., King, P.L., Ming, D.W., Perrett, G.M., Thompson, L.M., 2015. Germanium enrichments in sedimentary rocks in Gale Crater, Mars: Constraining the timing of alteration and character of the protolith. Presented at the *46th Lunar and Planetary Science Conference*, Ab. 1564.

Berman D.C., Balme M.R., Rafkin S.C.R., Zimbelman J.R., 2011. Transverse aeolian ridges (TARs) on Mars II: Distributions, orientations, and ages. *Icarus*, **213**, 116–130, doi:10.1016/j.icarus.2011.02.014.

Berman, D.C., Balme, M.R., Michalski, J.R., Clark, S.C., Joseph, E.S.C., 2018. High-resolution investigations of transverse aeolian ridges on Mars. *Icarus*, **312,** 247–266, doi:10.1016/j.icarus.2018.05.003.

Bertrand, T., Forget, F., Umurhan, O.M., Grundy, W.M., Schmitt, B., Protopapa, S., Zangari, A.M., White, O.L., Schenk, P.M., Singer, K.N., Stern, A., 2018. The nitrogen cycles on Pluto over seasonal and astronomical timescales. *Icarus*, **309**, 277–296, doi:10.1016/j.icarus.2018.03.012.

Bertrand, T., Forget, F., Umurhan, O.M., Moore, J.M., Young, L.A., Protopapa, S., Grundy, W.M., Schmitt, B., Dhingra, R.D., Binzel, R.P., Earle, A.M., 2019. The CH_4 cycles on Pluto over seasonal and astronomical timescales. *Icarus*, **329**, 148–165, doi:10.1016/j.icarus.2019.02.007.

Bertrand, T., Forget, F., White, O., Schmitt, B., Stern, S.A., Weaver, H.A., Young, L.A., Ennico, K., Olkin, C.B., New Horizons Science Team, 2020. Pluto's beating heart regulates the atmospheric circulation: Results from high-resolution and multiyear numerical climate simulations. *Journal of Geophysical Research: Planets*, **125**(2), e2019JE006120, doi:10.1029/2019JE006120.

Bibring, J.-P., Langevin, Y., Poulet, F., Gendrin, A., Gondet, B., Berthé, M., Soufflot, A., Drossart, P., Combes, M., Bellucci, G., Moroz, V., 2004. Perennial water ice identified in the south polar cap of Mars. *Nature*, **428**(6983), 627–630.

Bierson, C.J., Phillips, R.J., Smith, I.B., Wood, S.E., Putzig, N.E., Nunes, D., Byrne, S., 2016. Stratigraphy and evolution of the buried CO_2 deposit in the martian south polar cap. *Geophysical Research Letters*, **43**(9), 4172–4179.

Birch, S.P.D., Tang, Y., Hayes, A.G., Kirk, R.L., Bodewits, D., Campins, H., Fernandez, Y., de Freitas Bart, R., Kutsop, N.W., Sierks, H., Soderblom, J.M., Squyres, S.W., Vincent, J.-B., 2017. Geomorphology of comet 67P/Churyumov–Gerasimenko. *Monthly Notices of the Royal Astronomical Society* **469**, S50–S67, doi:10.1093/mnras/stx1096.

Bishop, J.L., Yeşilbaş, M., Hinman, N.W., Burton, Z.F.M., Englert, P.A.J., Toner, J.D., McEwen, A.S., Gulick, V.C., Gibson, E.K., Koeberl, C., 2020. Martian subsurface cryosalt expansion and collapse as trigger for landslides. *Science Advances*, in press.

and Blewett, D.T., Chabot, N.L., Denevi, B.W., Ernst, C.M., Head, J.W., Izenberg, N.R., Murchie, S.L., Solomon, S.C., Nittler, L.R., McCoy, T.J., Xiao, Z., Baker, D.M.H., Fassett, C.I., Braden, S.E., Oberst, J., Scholten, F., Preusker, F., Hurwitz, D.M., 2011. Hollows on Mercury: MESSENGER evidence for geologically recent volatile-related activity. *Science*, **333**, 1856–1859, doi:10.1126/science.1211681.

Bordiec, M., Carpy, S., Bourgeois, O., Herny, C., Massé, M., Perret, L., Claudin, P., Pochat, S., Douté, S., 2020. Sublimation waves: Geomorphic markers of interactions between icy planetary surfaces and winds. *Earth-Science Reviews*, **211**, 103350, doi:10.1016/j.earscirev.2020.103350.

Bourke, M.C., Cranford, A., 2011. Seasonal furrow formation on Mars polar dunes. Presented at *Fifth International Conference on Mars Polar Science and Exploration*, Ab. #6059.

Bourke, M., Wilson, S.A., Zimbelman, J.R., 2003. The variability of transverse aeolian ridges in troughs on Mars. Presented at the *34th Lunar and Planetary Science Conference*, Ab. 2090.

Bourke, M.C., Bullard, J.E., Barnouin-Jha, O.S., 2004. Aeolian sediment transport pathways and aerodynamics at troughs on Mars. *Journal of Geophysical Research: Planets*, **109**, E07005, doi:10.1029/2003JE002155.

Bourke, M., Edgett, K., Cantor, B., 2008. Recent aeolian dune change on Mars. *Geomorphology*, **94**, 247–255, doi: 10.1016/j.geomorph.2007.05.012.

Bourke, M.C., Ewing, R.C., Finnegan, D., McGowan, H.A., 2009. Sand dune movement in the Victoria Valley, Antarctica. *Geomorphology*, **109**, 148–160, doi:10.1016/j.geomorph.2009.02.028.

Bourke, M.C., Nield, J.M., Diniega, S., Hansen, C.J., McElwain, J.N., Titus, T.N., 2016a. The geomorphic effect of sublimating CO_2 blocks on dune lee slopes at Grand Falls, Arizona. Presented at the *47th Lunar and Planetary Science Conference*, Ab. 2407.

Bourke, M., Nield, J., Diniega, S., Hansen, C., McElwaine, J., 2016b. A field study of the geomorphic effects of sublimating CO_2 blocks on dune slopes at Coral Pink Dunes, Utah. Presented at the *European Planetary Science Conference*, Ab. EPSC2016-10450.

Boyce, J.M., Wilson, L., Mouginis-Mark, P.J., Hamilton, C.W., Tornabene, L.L., 2012. Origin of small pits in martian impact craters. *Icarus*, **221**, 262–275, doi:10.1016/j.icarus.2012.07.027.

Boynton, W., Feldman, W.C., Squyres, S.W., Prettyman, T.H., Brückner, J., Evans, L.G., Reedy, R.C., Starr, R., Arnold, J.R., Drake, D.M., Englert, P.A.J., 2002. Distribution of hydrogen in the near surface of Mars: Evidence for subsurface ice deposits. *Science*, 297(5578), 81–85, doi:10.1126/science.1073722.

2505 Bramson, A.M., Byrne, S., Putzig, N.E., Sutton, S., Plaut, J.J., Brothers, T.C., Holt, J.W., 2015.
2506 Widespread excess ice in Arcadia Planitia, Mars. *Geophysical Research Letters*, **42**(16),
2507 6566–6574, doi:10.1002/2015GL064844.

2508 Bramson, A.M., Byrne, S., Bapst, J., 2017. Preservation of mid-latitude ice sheets on Mars.
2509 *Journal of Geophysical Research*, **122**, 2250–2266, doi:10.1002/2017JE005357.

2510 Bramson, A.M., Byrne, S., Bapst, J., Smith, I.B., McClintock, T., 2019. A migration model for
2511 the polar spiral troughs of Mars. *JGR Planets*, **124**(4), 1020–1043,
2512 doi:10.1029/2018JE005806.

2513 Bridges, N.T., Ehlmann, B.L., 2018. The Mars Science Laboratory (MSL) Bagnold dunes
2514 campaign, Phase I: Overview and introduction to the special issue. *Journal of Geophysical*
2515 *Research: Planets*, **123**(1), 3–19, doi:10.1002/2017JE005401.

2516 Bridges, N.T., Herkenhoff, K.E., Titus, T.N., Kieffer, H.H., 2001. Ephemeral dark spots
2517 associated with martian gullies. Presented at *32nd Lunar and Planetary Science Conference*,
2518 Ab. #2126.

2519 Bridges, N.T., Geissler, P.E., McEwen, A.S., Thomson, B.J., Chuang, F.C., Herkenhoff, K.E.,
2520 Keszthelyi, L.P., Martínez-Alonso, S., 2007. Windy Mars: A dynamic planet as seen by the
2521 HiRISE camera. *Geophysical Research Letters*, **34**(23), L23205,
2522 doi:10.1029/2007GL031445.

2523 Bridges, N.T. Bourke, M.C., Geissler, P.E., Banks, M.E., Colon, C., Diniega, S., Golombek,
2524 M.P., Hansen, C.J., Mattson, S., McEwen, A.S., Mellon, M.T., 2012a. Planet-wide sand
2525 motion on Mars. *Geology*, **40**(1), 31–34, doi:10.1130/G32373.1.

2526 Bridges, N.T., Ayoub, F., Avouac, J.-P., Leprince, S., Lucas, A., Mattson, S., 2012b. Earth-like
2527 sand fluxes on Mars. *Nature*, **485**, 339–342, doi:10.1038/nature11022.

2528 Bridges, N.T., Geissler, P., Silvestro, S., Banks, M., 2013. Bedform migration on Mars: Current
2529 results and future plans. *Aeolian Research*, **9**, 133–151, doi:10.1016/j.aeolia.2013.02.004.

2530 Bridges, N.T., Sullivan, R., Newman, C.E., Navarro, S., van Beek, J., Ewing, R.C., Ayoub, F.,
2531 Silvestro, S., Gasnault, O., Le Mouélic, S., Lapôtre, M. G. A., Rapin, W., 2017. martian
2532 aeolian activity at the Bagnold Dunes, Gale Crater: The view from the surface and orbit.
2533 *Journal of Geophysical Research: Planets*, **112**, 2077–2100, doi:10.1002/2017JE005263.

2534 Brothers S.C., Kocurek G., 2018. The transitional depositional environment and sequence
2535 stratigraphy of Chasma Boreale. *Icarus*, **308**, 27–41, doi:10.1016/j.icarus.2017.08.038.

2536 Brown, J.R., Roberts, G.P., 2019. Possible evidence for variation in magnitude for marsquakes
2537 from fallen boulder populations, Grjota Valles, Mars. *Journal of Geophysical Research:*
2538 *Planets,* **124**, 801–822, doi:10.1029/2018JE005622.

2539 Brown, A.J., Calvin, W.M., Becerra, P., Byrne, S., 2016. Martian north polar cap summer water
2540 cycle. *Icarus*, **277**, 401–415, doi:10.1016/j.icarus.2016.05.007.

2541 Buhler, P.B., Ingersoll, A.P., 2018. Sublimation pit distribution indicates convection cell surface
2542 velocities of∼ 10 cm per year in Sputnik Planitia, Pluto. *Icarus,* **300**, 327–340,
2543 doi:10.1016/j.icarus.2017.09.018.

2544 Buhler, P.B., Ingersoll, A.P., Ehlmann, B.L., Fassett, C.I., Head, J.W., 2017. How the martian
2545 residual south polar cap develops quasi-circular and heart-shaped pits, troughs, and moats.
2546 *Icarus*, **286**, 69–93, doi:10.1016/j.icarus.2017.01.012.

Buhler, P.B., Dickson, J., Ehlmann, B.L., Ingersoll, A.P., Byrne, S., Tao, Y., Muller, J.P., 2018. Prospects for measuring vertical change on the martian residual south polar cap using HiRISE digital elevation models. Presented at the *49th Lunar and Planetary Science Conference*, Ab. 2908.

Buhler, P.B., Ingersoll, A.P., Piqueux, S., Ehlmann, B.L., Hayne, P.O., 2020. Coevolution of Mars' atmosphere and massive south polar CO_2 ice deposit. *Nature Astronomy*, **4**, 364–371, doi:10.1038/s41550-019-0976-8.

Businger, J.A., Yaglom, A.M., 1971. Introduction to Obukhov's paper on 'turbulence in an atmosphere with a non–uniform temperature'. *Boundary-Layer Meteorology*, **2**(1), 3–6.

Byrne, S., Ingersoll, A.P., 2003a. Martian climatic events on timescales of centuries: Evidence from feature morphology in the residual south polar ice cap. *Geophysical Research Letters*, **30**(13), 1696, doi:10.1029/2003GL017597.

Byrne, S., Ingersoll, A.P., 2003b. A sublimation model for martian south polar ice features. *Science*, **299**(5609), 1051–1053, doi:10.1126/science.1080148.

Byrne, S., Murray, B.C. 2002. North polar stratigraphy and the paleo-erg of Mars. *Journal of Geophysical Research*, **107**, 1–12.

Byrne, S., Dundas, C.M., Kennedy, M.R., Mellon, M.T., McEwen, A.S., Cull, S.C., Daubar, I.J., Shean, D.E., Seelos, K.D., Murchie, S.L., Cantor, B.A., 2009. Distribution of mid-latitude ground ice on Mars from new impact craters. *Science*, **325**(5948), 1674–1676, doi:10.1126/science.1175307.

Byrne, S., Hayne, P.O., Becerra, P., the HiRISE Team, 2015. Evolution and stability of the residual CO_2 ice cap. Presented at the *46th Lunar and Planetary Science Conference*, Ab. 1657.

Byrne, S., Sori, M.M., Russell, P., Pathare, A.V., Becerra, P., Molaro, J.L., Sutton, S., Mellon, M.T., the HiRISE Team, 2017. Mars polar cliffs: stressed out and falling apart. Presented at the *European Planetary Science Congress 2017*, Ab. 333.

Calvin, W.M., Seelos, K.D., 2019. Evolution within the Martian Southern Seasonal Cryptic Terrain from CTX and CRISM. Presented at the *AGU Fall Meeting*, 2019, Ab. P33F-3501.

Calvin, W.M., James, P.B., Cantor, B.A., Dixon, E.M., 2015. Interannual and seasonal changes in the north polar ice deposits of Mars: Observations from MY 29–31 using MARCI. *Icarus*, **251**, 181-190, doi:10.1016/j.icarus.2014.08.026.

Cardinale, M., Pozzobon, R., Tangari, A.C., Runyon, K., Di Primio, M., Marinangeli, L., 2020. Reconstruction of the sand transport pathways and provenance in Moreux crater, Mars. *Planetary and Space Science*, **181**, 104788, doi:10.1016/j.pss.2019.104788.

Cartwright, R.J., Emery, J.P., Rivkin, A.S., Trilling, D.E., Pinilla-Alonso, N., 2015. Distribution of CO_2 ice on the large moons of Uranus and evidence for compositional stratification of their near–surfaces. *Icarus*, **257**, 428–456, doi:10.1016/j.icarus.2015.05.020.

Cedillo-Flores, Y., Treiman, A. H., Lasue, J., Clifford, S. M., 2011. CO_2 gas fluidization in the initiation and formation of martian polar gullies. *Geophysical Research Letters*, **38**, L21202, doi:10.1029/2011GL049403.

Chamberlain, M.A., Boynton, W.V., 2007. Response of martian ground ice to orbit-induced climate change. *Journal of Geophysical Research*, **112**, E06009. https://doi.org/10.1029/2006JE002801.

Cheng, A.F., Lisse, C.M., A'Hearn, M., 2013. Surface geomorphology of Jupiter Family Comets: A geologic process perspective. *Icarus*, **222**(2), 808–817, doi:10.1016/j.icarus.2012.10.004.

Chevrier, V.F., Rivera-Valentin, E.G., 2012. Formation of recurring slope lineae by liquid brines on present-day Mars. *Geophysical Research Letters*, **39**, doi:10.1029/2012GL054119.

Chinnery, H.E., Hagermann, A., Kaufmann, E., Lewis, S.R., 2018. The penetration of solar radiation into carbon dioxide ice. *Journal of Geophysical Research: Planets*, **123**(4), 864–871, doi:10.1002/2018JE005539.

Chojnacki, M., Moersch, J., Burr, D., 2010. Climbing and falling dunes in Valles Marineris, Mars. *Geophysical Research Letters*, **37**(8), L08201, doi:10.1029/2009GL042263.

Chojnacki, M., Burr, D.M., Moersch, J.E., 2014a. Valles Marineris dune fields as compared with other martian populations: Diversity of dune compositions, morphologies, and thermophysical properties. *Icarus (Third Planetary Dunes Systems)*, **230**, 96–142, doi:10.1016/j.icarus.2013.08.018.

Chojnacki, M., Burr, D.M., Moersch, J.E., Wray J. J., 2014b. Valles Marineris dune sediment provenance and pathways. *Icarus*, **232**,187–219, doi:10.1016/j.icarus.2014.01.011.

Chojnacki, M., Johnson, J.R., Moersch, J.E., Fenton, L.K., Michaels, T.I., Bell III, J.F., 2015. Persistent aeolian activity at Endeavour crater, Meridiani Planum, Mars: new observations from orbit and the surface. *Icarus*, **251**, 275–290, doi:10.1016/j.icarus.2014.04.044.

Chojnacki, M., McEwen, A., Dundas, C., Ojha, L., Urso, A., Sutton, S., 2016. Geologic context of Recurring Slope Lineae in Melas and Coprates Chasmata, Mars. *Journal of Geophysical Research,* **121**(2), 1204–1231, doi:10.1002/2015JE004991.

Chojnacki, M., Urso, A.C., Fenton, L.K., Michaels, T.I., 2017. Aeolian dune sediment flux heterogeneity in Meridiani Planum, Mars. *Aeolian Research*, **26**, 73–88, doi:10.1016/j.aeolia.2016.07.004.

Chojnacki, M., Banks, M., Urso, A., 2018. Wind-driven erosion and exposure potential at Mars 2020 rover candidate-landing sites. *Journal of Geophysical Research: Planets*, **123**, 468–488, doi:10.1002/2017JE005460.

Chojnacki, M., Banks, M.E., Fenton, L.K., Urso, A.C., 2019. Boundary condition controls on the high-sand-flux regions of Mars. *Geology*, **47**(5), 427–430, doi: 10.1130/G45793.1.

Chojnacki, M., Fenton, L.K., Weintraub, A.R., Edgar, L.A., Jodhpurkar, M.J., Edwards, C.S. 2020. Ancient martian aeolian sand dune deposits recorded in the stratigraphy of Valles Marineris and implications for past climates. *Journal of Geophysical Research: Planets*, **125**, e2020JE006510, doi:10.1029/2020JE006510.

Chuang, F.C., Beyer, R.A., McEwen, A.S., Thomson, B.J., 2007. HiRISE observations of slope streaks on Mars. *Geophysical Research Letters*, **34**(20), L20204, doi:10.1029/2007GL031111.

Claudin, P., Andreotti, B., 2006. A scaling law for aeolian dunes on Mars, Venus, Earth, and for subaqueous ripples. *Earth and Planetary Science Letters*, **252**, 30–44, doi:10.1016/j.epsl.2006.09.004.

Colaprete, A., Barnes, J.R., Haberle, R.M., Hollingsworth, J.L., Kieffer, H.H., Titus, T.N., 2005. Albedo of the south pole on Mars determined by topographic forcing of atmosphere dynamics. *Nature*, **435**, 184–188, doi:10.1038/nature03561.

Costard, F.M., Kargel, J.S., 1995. Outwash plains and thermokarst on Mars. *Icarus,* **114**, 93–112.

Courrech du Pont, S., Narteau, C., Gao, X. 2014. Two modes for dune orientation. *Geology*, **42**(9), 743–746, doi: 10.1130/G35657.1.

Cross, A.J., Goldsby, D.L., Hager, T.F., Smith, I.B., 2020. The rheological behavior of CO_2 ice: Application to glacial flow on Mars. *Geophysical Research Letters*, **47**(22), GL090431, doi:10.1029/2020GL090431.

Daubar, I.J., McEwen, A.S., Byrne, S., Kennedy, M.R., Ivanov, B., 2013. The current martian cratering rate. *Icarus*, **225**, 506–516, doi:10.1016/j.icarus.2013.04.009.

Daubar, I.J., Banks, M.E., Schmerr, N.C., Golombek, M.P., 2019. Recently formed crater clusters on Mars. *Journal of Geophysical Research: Planets*, **124**(4), 958–969, doi:10.1029/2018JE005857.

Davis, J.M., Banham, S.G., Grindrod, P.M., Boazman, S.J., Balme, M.R., Bristow, C.S., 2020. Morphology, development, and sediment dynamics of elongating linear dunes on Mars. *Geophysical Research Letters*, **47**, e2020GL088456, doi:10.1029/2020GL088456.

Day, M., Kocurek, G. 2016. Observations of an aeolian landscape: From surface to orbit in Gale crater. *Icarus*, **280**, 37–71, doi: 10.1016/j.icarus.2015.09.042

Day, M., Edgett, K. S., Stumbaugh, D., 2019. Ancient stratigraphy preserving a wet-to-dry, fluvio-lacustrine to aeolian transition near Barth crater, Arabia Terra, Mars. *Journal of Geophysical Research: Planets*, **124**(12), 3402–3421, doi:10.1029/2019JE006226.

de Haas, T., McArdell, B.W., Conway, S.J., McElwaine, J.N., Kleinhans, M.G., Salese, F., Grindrod, P.M., 2019. Initiation and flow conditions of contemporary flows in Martian gullies. *J. Geophys Res. Planets*, **124**, 2246–2271, doi:10.1029/2018JE005899.

Denevi, B.W., Blewett, D.T., Buczkowski, D.L., Capaccioni, F., Capria, M.T., De Sanctis, M.C., Garry, W.B., Gaskell, R.W., Le Corre, L., Li, J.-Y., Marchi, S., McCoy, T.J., Nathues, A., O'Brien, D.P., Petro, N.E., Pieters, C.M., Preusker, F., Raymond, C.A., Reddy, V., Russell, C.T., Schenk, P., Scully, J.E.C., Sunshine, J.M., Tosi, F., Williams, D.A., Wyrick, D., 2012. Pitted terrain on Vesta and implications for the presence of volatiles. *Science*, **338**, 246–249, doi:10.1126/science.1225374.

Dickson, J.L., Head, J.W., Levy, J.S., Marchant, D.R., 2013. Don Juan Pond, Antarctica: near-surface $CaCl_2$-brine feeding Earth's most saline lake and implications for Mars. *Scientific Reports*, **3**, 1166, doi:10.1038/srep01166.

Dickson, J.L., Kerber, L.A., Fassett, C.I., Ehlmann, B.L., 2018. A global, blended CTX mosaic of Mars with vectorized seam mapping: a new mosaicking pipeline using principles of non-destructive image editing. Presented at the *49th Lunar and Planetary Science Conference*, Ab. 2480.

Diniega, S., Smith, I.B., 2020. High-priority science questions identified at the Mars Workshop on Amazonian and Present-day Climate. *Planetary and Space Science*, **182**, 104813, doi:10.1016/j.pss.2019.104813.

Diniega, S., Byrne, S., Bridges, N.T., Dundas, C.M., McEwen, A.S., 2010. Seasonality of present-day martian dune-gully activity. *Geology*, **38**, 1047–1050, doi:10.1130/G31287.1.

Diniega, S., Hansen, C.J., McElwaine, J.N., Hugenholtz, C.H., Dundas, C.M., McEwen, A.S., Bourke, M.C., 2013. A new dry hypothesis for the formation of martian linear gullies. *Icarus*, **225**(1), 526–537, doi:10.1016/j.icarus.2013.04.006.

Diniega, S., Kreslavsky, M., Radebaugh, J., Silvestro, S., Telfer, M., Tirsch, D., 2017. Our evolving understanding of aeolian bedforms, based on observation of dunes on different worlds. *Aeolian Research*, **26**, 5–27, doi:10.1016/j.aeolia.2016.10.001.

Diniega, S., Hansen, C.J., Allen, A., Grigsby, N., Li, Z., Perez, T., Chojnacki, M., 2019a. Dune-slope activity due to frost and wind throughout the north polar erg, Mars. *Geological Society, London, Special Publications*, **467**, 95–114, doi:10.1144/SP467.6

Diniega, S., Widmer, J.M., Gary-Bicas, C., Fraeman, A.A., Hayne, P.O., Piqueux, S., 2019b. Correlating present-day surface and subsurface frost conditions with geomorphologic activity on Mars. Presented at the *50th Lunar and Planetary Science Conference*, Ab. 2165.

Dorn, T., Day, M. 2020. Intracrater sediment trapping and transport in Arabia Terra, Mars. *Journal of Geophysical Research: Planets*, **125**(9), e2020JE006581, doi:10.1029/2020JE006581.

Dundas, C.M., 2017. Effects of varying obliquity on Martian sublimation thermokarst landforms. *Icarus*, **281**, 115–120, doi:10.1016/j.icarus.2016.08.031.

Dundas, C.M., 2020a. An aeolian grainflow model for martian Recurring Slope Lineae, *Icarus*, **343**, 113681, doi:10.1016/j.icarus.2020.113681.

Dundas, C.M., 2020b. Geomorphological evidence for a dry dust avalanche origin of slope streaks on Mars. *Nature Geoscience*, **13**, 473-476, doi:10.1038/s41561-020-0598-x.

Dundas, C.M., Byrne, S., 2010. Modeling sublimation of ice exposed by new impacts in the martian mid-latitudes. *Icarus*, **206**, 716–728. https://doi.org/10.1016/j.icarus.2009.09.007.

Dundas, C.M., Diniega, S., Hansen, C.J., Byrne, S. McEwen, A.S., 2012. Seasonal activity and morphological changes in Martian gullies. *Icarus*, **220**(1), 124–143, doi:10.1016/j.icarus.2012.04.005.

Dundas, C.M., Byrne, S., McEwen, A.S., Mellon, M.T., Kennedy, M.R., Daubar, I.J., Saper, L., 2014. HiRISE observations of new impact craters exposing martian ground ice. *Journal of Geophysical Research*, **119**, 109–127, doi:10.1002/2013JE004482.

Dundas, C.M., Diniega, S., McEwen, A.S., 2015a. Long-term monitoring of martian gully formation and evolution with MRO/HiRISE. *Icarus*, **251**, 244–263, doi:10.1016/j.icarus.2014.05.013.

Dundas, C.M., Byrne, S., McEwen, A., 2015b. Modeling the development of martian sublimation thermokarst landforms. *Icarus*, **262**, 154–169, doi:10.1016/j.icarus.2015.07.033.

2707 Dundas, C.M., McEwen, A.S., Chojnacki, M., Milazzo, M.P., Byrne, S., McElwaine, J.N., Urso,
2708 A., 2017. Granular flows at recurring slope lineae on Mars indicate a limited role for liquid
2709 water. *Nature Geoscience*, **10**(12), 903-907.

2710 Dundas, C.M., Bramson, A.M., Ojha, L., Wray, J.J., Mellon, M.T., Byrne, S., McEwen, A.S.,
2711 Putzig, N.E., Viola, D., Sutton, S., Clark, E., 2018. Exposed subsurface ice sheets in the
2712 martian mid-latitudes. *Science*, **359**, 199–201, doi:10.1126/science.aao1619.

2713 Dundas, C.M., McEwen, A.S., Diniega, S., Hansen, C. J., Byrne, S., McElwaine, J.N., 2019a.
2714 The formation of gullies on Mars today. *Geological Society, London, Special Publications*,
2715 **467**, 67–94, doi:10.1144/SP467.5.

2716 Dundas, C.M., Mellon, M.T., Conway, S.J., Gastineau, R., 2019b. Active boulder movement at
2717 high martian latitudes. *Geophysical Research Letters*, **46**(10), 2019GL082293,
2718 doi:10.1029/2019GL082293.

2719 Duran Vinent, O., Andreotti, B., Claudin, P., Winter, C., 2019. A unified model of ripples and
2720 dunes in water and planetary environments. *Nature Geoscience*, **12**, 345–350,
2721 doi:10.1038/s41561-019-0336-4.

2722 Edgett, K., Christensen, P., 1991. The particle size of martian aeolian dunes. *Journal of*
2723 *Geophysical Research*, **96**(E5), 22,765–22,776.

2724 Edgett, K.S., Lancaster, N., 1993. Volcaniclastic aeolian dunes: terrestrial examples and
2725 application to martian sands. *Journal of Arid Environments*, **25**(3), 271–297,
2726 doi:10.1006/jare.1993.1061.

2727 Edgett, K.S., Malin, M.C., 2000. New views of Mars eolian activity, materials, and surface
2728 properties: Three vignettes from the Mars Global Surveyor Mars Orbiter Camera. *Journal of*
2729 *Geophysical Research,* **105**, 1623–1650, doi:10.1029/1999JE001152.

2730 Edwards, C.S., Piqueux, S., 2016. The water content of recurring slope lineae on Mars.
2731 *Geophysical Research Letters,* **43**, doi:10.1002/2016GL070179.

2732 Edwards, C.S., Piqueux, S., Hamilton, V.E., Fergason, R.L., Herkenhoff, K.E., Vasavada, A.R.,
2733 Bennett, K.A., Sacks, L., Lewis, K., Smith, M.D., 2018. The thermophysical properties of the
2734 Bagnold Dunes, Mars: Ground-truthing orbital data. *Journal of Geophysical Research:*
2735 *Planets*, **123**, 1307–1326, doi:10.1029/2017JE005501.

2736 Ehlmann, B.L., Edgett, K.S., Sutter, B., Achilles, C.N., Litvak, M.L., Lapôtre, M.G.A., Sullivan,
2737 R., Fraeman, A.A., Arvidson, R.E., Blake, D.F., Bridges, N.T., 2017. Chemistry, mineralogy,
2738 and grain properties at Namib and High dunes, Bagnold dune field, Gale crater, Mars: A
2739 synthesis of Curiosity rover observations. *Journal of Geophysical Research: Planets*, **122**,
2740 2510–2543, doi:10.1002/2017JE005267.

2741 Ewing R.C., Kocurek G., 2010. Aeolian dune-field pattern boundary conditions.
2742 *Geomorphology*, **114**, 175–187, doi:10.1016/j.geomorph.2009.06.015.

2743 Ewing, R.C., Lapôtre, M.G.A., Lewis, K.W., Day, M., Stein, N., Rubin, D.M., Sullivan, R.,
2744 Banham, S., Lamb, M.P., Bridges, N.T., Gupta, S., 2017. Sedimentary processes of the
2745 Bagnold Dunes: Implications for the eolian rock record of Mars. *Journal of Geophysical*
2746 *Research: Planets*, **122**, 2544–2573, doi:10.1002/2017JE005324.

2747 Fanale, F.P., Salvail, J.R., Zent, A.P., Postawko, S.E., 1986. Global distribution and migration of
2748 subsurface ice on Mars. *Icarus*, **67**(1), 1–18, doi:10.1016/0019-1035(86)90170-3.

2749 Fanara, L., Gwinner, K., Hauber, E., Oberst, J., 2020a. Present-day erosion rate of north polar
2750 scarps on Mars due to active mass wasting. *Icarus*, **342**, 113434,
2751 doi:10.1016/j.icarus.2019.113434.

2752 Fanara, L., Gwinner, K., Hauber, E., Oberst, J., 2020b. Automated detection of block falls in the
2753 north polar region of Mars. *Planetary and Space Science*, **180**, 104733,
2754 doi:10.1016/j.pss.2019.104733.

2755 Farley, K.A., Malespin, C., Mahaffy, P., Grotzinger, J.P., Vasconcelos, P.M., Milliken, R.E.,
2756 Malin, M., Edgett, K.S., Pavlov, A.A., Hurowitz, J.A., Grant, J.A., 2014. In situ radiometric
2757 and exposure age dating of the Martian surface. *Science*, **343**(6169), 1247166,
2758 doi:10.1126/science.1247166.

2759 Fedo, C.M., McGlynn, I.O., McSween Jr, H.Y., 2015. Grain size and hydrodynamic sorting
2760 controls on the composition of basaltic sediments: Implications for interpreting martian soils.
2761 *Earth and Planetary Science Letters*, **423**, 67–77, doi:10.1016/j.epsl.2015.03.052.

2762 Fenton, L.K., 2005. Potential sand sources for the dune fields in Noachis Terra, Mars. *Journal of*
2763 *Geophysical Research,* **110,** E11004, doi:10.1029/2005JE002436.

2764 Fenton, L.K., 2020. Updating the global inventory of dune fields on mars and identification of
2765 many small dune fields. *Icarus*, **352**, 114018, doi:10.1016/j.icarus.2020.114018.

2766 Fenton, L.K., Hayward R.K.. 2010. Southern high latitude dune fields on Mars: Morphology,
2767 aeolian inactivity, and climate change. *Geomorphology*, **121**, 98–121,
2768 doi:10.1016/j.geomorph.2009.11.006.

2769 Fenton, L.K., Michaels, T.I., 2010. Characterizing the sensitivity of daytime turbulent activity on
2770 Mars with the MRAMS LES: Early results. *Mars*, **5**, 159–171, doi:10.1555/mars.2010.0007.

2771 Fenton, L.K., Ewing, R.C., Bridges, N.T., Lorenz, R., 2013. 11.15 Extraterrestrial Aeolian
2772 Landscapes. In *Treatise on Geomorphology*. Elsevier, 287–312.

2773 Fenton, L.K., Gullikson, A.L., Hayward, R.K., Charles, H., Titus, T.N., 2019. The Mars Global
2774 Digital Dune Database (MGD3): global patterns of mineral composition and bedform
2775 stability. *Icarus*, **330**, 189–203, doi:10.1016/j.icarus.2019.04.025.

2776 Fischer, E., Martínez, G.M., Rennó, N.O., Tamppari, L.K., Zent, A.P., 2019. Relative humidity
2777 on Mars: new results from the Phoenix TECP sensor. *Journal of Geophysical Research:*
2778 *Planets*, **124**(11), 2780–2792, doi:10.1029/2019JE006080.

2779 Forget, F., Hourdin, F., Talagrand, O., 1998. CO_2 snowfall on Mars: Simulation with a general
2780 circulation model. *Icarus*, **131**(2), 302–316, doi:10.1006/icar.1997.5874.

2781 Forget, F., Hourdin, F., Fournier, R., Hourdin, C., Talagrand, O., Collins, M., Lewis, S. R., Read,
2782 P. L., Huot, J.-P., 1999. Improved general circulation models of the Martian atmosphere from
2783 the surface to above 80 km. *Journal of Geophysical Research*, **104**, 24,155-24,176,
2784 doi:10.1029/1999JE001025.

2785 Forget, F., Bertrand, T., Vangvichith, M., Leconte, J., Millour, E., Lellouch, E., 2017. A post–
2786 new horizons global climate model of Pluto including the N_2, CH_4 and CO cycles. *Icarus*,
2787 **287**, 54–71, doi:10.1016/j.icarus.2016.11.038.

2788 Foroutan, M., Steinmetz, G., Zimbelman, J.R., Duguay, C.R.. 2019. Megaripples at Wau-an-
2789 Namus, Libya: A new analog for similar features on Mars. *Icarus*, **319**, 840–851,
2790 doi:10.1016/j.icarus.2018.10.021.

2791 Foroutan, M., Zimbelman, J.R.. 2016. Mega-ripples in Iran: A new analog for transverse aeolian
2792 ridges on Mars. *Icarus*, **274**, 99–105, doi:10.1016/j.icarus.2016.03.025.

2793 French, H., 2007. *The Periglacial Environment*, Third Edition. Wiley, Chichester.

2794 Gallagher, C.J., Balme, M.R., 2011. Landforms indicative of ground-ice thaw in the northern
2795 high latitudes of Mars. *Geological Society, London, Special Publications*, **356**(1), 87–110,
2796 doi:10.1144/SP356.6.

2797 Gallagher, C., Balme, M.R., Conway, S.J., Grindrod, P.M., 2011. Sorted clastic stripes, lobes and
2798 associated gullies in high–latitude craters on Mars: Landforms indicative of very recent,
2799 polycyclic ground-ice thaw and liquid flows. *Icarus*, **211**(1), 458–471,
2800 doi:10.1016/j.icarus.2010.09.010.

2801 Gao, X., Narteau, C., Rozier, O., du Pont, S.C., 2015. Phase diagrams of dune shape and
2802 orientation depending on sand availability. *Scientific Reports*, **5**, 14677.
2803 doi:10.1038/srep14677.

2804 Gardin, E., Allemand, P., Quantin, C., Thollot, P., 2010. Defrosting, dark flow features, and dune
2805 activity on Mars: example in Russell crater. *Journal of Geophysical Research: Planets*,
2806 **115**(E6), E06016, doi:10.1029/2009JE003515.

2807 Gary-Bicas, C.E., Hayne, P.O., Horvath, T., Heavens, N.G., Kass, D.M., Kleinböhl, A., Piqueux,
2808 S., Shirley, J.H., Schofield, J.T., McCleese, D.J., 2020. Asymmetries in snowfall, emissivity,
2809 and albedo of Mars' seasonal polar caps: Mars Climate Sounder observations. *Journal of*
2810 *Geophysical Research: Planets*, **125**(5), e2019JE006150, doi:10.1029/2019JE006150.

2811 Giese, B., Denk, T., Neukum, G., Roatsch, T., Helfenstein, P., Thomas, P.C., Turtle, E.P.,
2812 McEwen, A., Porco, C.C., 2008. The topography of Iapetus' leading side. *Icarus*, **193**(2),
2813 359–371, doi:10.1016/j.icarus.2007.06.005.

2814 Geissler, P.E., 2014. The birth and death of transverse aeolian ridges on Mars. *Journal of*
2815 *Geophysical Research: Planets*, **119**(12), 2583–2599, doi:10.1002/2014JE004633.

2816 Geissler, P.E., Wilgus, J.T.. 2017. The morphology of transverse aeolian ridges on Mars. *Aeolian*
2817 *Research*, **26**, 63–71, doi:10.1016/j.aeolia.2016.08.008.

2818 Geissler, P. E., Banks, M. E., Bridges, N. T., Silvestro, S., the HiRISE Team, 2012. HiRISE
2819 observations of sand dune motion on Mars: Emerging global trends. Presented at *3rd*
2820 *International Planetary Dunes Workshop*, Ab. #7053.

2821 Gendrin, A., Mangold, N., Bibring, J.-P., Langevin, Y., Gondet, B., Poulet, F., Bonello, G.,
2822 Quantin, C., Mustard, J., Arvidson, R., LeMouélic, S., 2005. Sulfates in martian layered
2823 terrains: the OMEGA/Mars Express view. *Science*, **307**(5715), 1587–1591,
2824 doi:10.1126/science.1109087.

2825 Golombek, M.P., Grant, J.A., Crumpler, L.S., Greeley, R., Arvidson, R.E., Bell, J.F., Weitz,
2826 C.M., Sullivan, R., Christensen, P.R., Soderblom, L.A., Squyres, S.W., 2006. Erosion rates at
2827 the Mars Exploration Rover landing sites and long-term climate change on Mars. *Journal of*
2828 *Geophysical Research: Planets*, **111**(E12), E12S10, doi:10.1029/2006JE002754.

2829 Golombek, M.P., Warner, N.H., Ganti, V., Lamb, M.P., Parker, T.J., Fergason, R.L., Sullivan,
2830 R., 2014. Small crater modification on Meridiani Planum and implications for erosion rates
2831 and climate change on Mars: Small crater modification on Mars. *Journal of Geophysical*
2832 *Research: Planets*, **119**, 2522–2547, doi:10.1002/2014JE004658.

2833 Golombek, M.P., Charalambous, C., Pike, W.T.., Sullivan, R., 2018. The origin of sand on Mars.
2834 Presented at the *49th Lunar and Planetary Science Conference*, Ab. 2319.

2835 Gomez-Elvira, J., Armiens, C., Carrasco, I., Genzer, M., Gomez, F., Haberle, R., Hamilton, V.E.,
2836 Harri, A.M., Kahanpaa, J., Kemppinen, O., Lepinette, A. 2014. Curiosity's rover
2837 environmental monitoring station: Overview of the first 100 sols. *Journal of Geophysical*
2838 *Research: Planets*, **11**, 1680–1688, doi: 10.1002/2013JE004576

2839 Goudie, A.S., Watson, A., 1981. The shape of desert sand dune grains. Journal of Arid
2840 Environments, **4**(3), 185–190, doi:10.1016/S0140-1963(18)31559-3.

2841 Gough, R. V., Nuding, D. L., Toigo, A., Guzewich, S., Tolbert, M. A., 2019a. An Examination
2842 of Atmospheric Water Vapor as a Source for Recurring Slope Lineae on Mars. Presented at
2843 the *Ninth International Conference on Mars*, Ab. 6327.

2844 Gough, R.V., Primm, K.M., Rivera-Valentín, E.G., Martínez, G.M., Tolbert, M.A., 2019b. Solid-
2845 solid hydration and dehydration of Mars-relevant chlorine salts: Implications for Gale Crater
2846 and RSL locations. *Icarus*, **321**, 1–13, doi:10.1016/j.icarus.2018.10.034.

2847 Grant, J.A., Golombek, M.P., Wilson, S.A., Farley, K.A., Williford, K.H., Chen, A., 2018. The
2848 science process for selecting the landing site for the 2020 Mars rover. *Planetary and Space*
2849 *Science*, **164**, 106–126, doi:10.1016/j.pss.2018.07.001.

2850 Greeley, R., Iversen, J.D., 1985. *Wind as a geological process on Earth, Mars, Venus and Titan*.
2851 Greeley R (ed). Cambridge Univ. Press: New York

2852 Greeley, R., White, B., Leach, R., Iversen, J., Pollack, J., 1976. Mars: Wind friction speeds for
2853 particle movement. *Geophysical Research Letters*, **3**(8), 417–420.

2854 Greeley, R., Leach, R., White, B., Iversen, J., Pollack, J., 1980. Threshold windspeeds for sand
2855 on Mars: Wind tunnel simulations. *Geophysical Research Letters*, **7**(2), 121-124.

2856 Greeley, R., Leach, R.N., Williams, S.H., White, B.R., Pollack, J.B., Krinsley, D.H., Marshall,
2857 J.R., 1982. Rate of wind abrasion on Mars. *Journal of Geophysical Research*, **87**, 10009–
2858 10024, doi:10.1029/JB087iB12p10009.

2859 Greeley, R., Lancaster, N., Lee, S., Thomas, P., 1992. Martian aeolian processes, sediments, and
2860 features. In *Mars*, pp.730–766.

2861 Greeley, R., Bender, K., Thomas, P.E., 1995. Wind-related features and processes on Venus:
2862 Summary of Magellan results. *Icarus*, **115**, 399–420.

2863 Greeley, R., Arvidson, R.E., Barlett, P.W., Blaney, D., Cabrol, N.A., Christensen, P.R.,
2864 Fergason, R.L., Golombek, M.P., Landis, G.A., Lemmon, M.T., McLennan, S.M., 2006.
2865 Gusev Crater: Wind-related features and processes observed by the Mars Exploration Rover
2866 Spirit. *Journal of Geophysical Research*, **111**, E02S09, doi:10.1029/2005JE002491

2867 Gigsby, N., Diniega, S., 2008. Slope and volume analysis of alcove-channel-apron avalanche
2868 morphologies within the north polar region of Mars. Presented at the *49th Lunar and*
2869 *Planetary Science Conference*, Ab. 1122.

2870 Grimm, R.E., Harrison, K.P., Stillman, D.E., 2014. Water budgets of martian recurring slope
2871 lineae. *Icarus*, **233**, 316–327, doi:10.1016/j.icarus.2013.11.013.

Grotzinger, J.P., Milliken, R.E., 2012. The sedimentary rock record of Mars: Distribution, origins, and global stratigraphy. *SEPM Special Publication: Sedimentary Geology of Mars*, **102**, 1–48, doi:10.2110/pec.12.102.0001.

Grotzinger, J.P., Arvidson, R.E., Bell Iii, J.F., Calvin, W., Clark, B.C., Fike, D.A., Golombek, M., Greeley, R., Haldemann, A., Herkenhoff, K.E., Jolliff, B.L., 2005. Stratigraphy and sedimentology of a dry to wet eolian depositional system, Burns Formation, Meridiani Planum, Mars. *Earth and Planetary Science Letters*, **240**, 11–72.

Grundy, W., 2003. Discovery of CO_2 ice and leading–trailing spectral asymmetry on the uranian satellite Ariel. *Icarus*, **162**, 222–229, doi:10.1016/S0019-1035(02)00075-1.

Grundy, W., Young, L., Spencer, J., Johnson, R., Young, E., Buie, M., 2006. Distributions of H_2O and CO_2 ices on Ariel, Umbriel, Titania, and Oberon from IRTF/SpeX observations. *Icarus*, **184**, 543–555, doi:10.1016/j.icarus.2006.04.016.

Gwinner, K., Bostelmann, J., Dumke, A., Michael, G., Annibali, S., Stark, A., Kersten, E., Walter, S., Roatsch, T., Jaumann, R., 2019. Characteristics of the HRSC Mars Chart (HMC-30) and its quality of co-registration with the MOLA reference. Presented at the *European Planetary Science Conference*, Ab. EPSC-DPS2019-2006-1.

Haberle, R. M., Gómez–Elvira, J., de la Torre Juárez, M., Harri, A.-M., Hollingsworth, J.L., Kahanpaa, H., Kahre, M.A., Lemmon, M., Martín-Torres, F.J., Mischna, M., Moores, J.E., Newman, C., Rafkin, S.C.R., Rennó, N., Richardson, M.I., Rodríguez–Manfredi, J.A., Vasavada, A.R., Zorzano-Mier, M.-P., 2014. Preliminary interpretation of the REMS pressure data from the first 100 sols of the MSL mission. *Journal of Geophysical Research: Planets*, **19(3)**, 440–453.

Hallet, B., 2013. Stone circles: form and soil kinematics. *Proc. R. Soc. A*, **371**(2004), 20120357–17, doi:10.1098/rsta.2012.0357.

Hansen, C.J., Paige, D.A., 1992. A thermal model for the seasonal nitrogen cycle on Triton. *Icarus*, **99**(2), 273–288.

Hansen, C.J., Paige, D.A., 1996. Seasonal Nitrogen Cycles on Pluto. *Icarus*, **120**, 247–265.

Hansen, C. J., Thomas, N., Portyankina, G., McEwen, A.S., Becker, T., Byrne, S., Herkenhoff, K., Kieffer, H., Mellon, M., 2010. HiRISE observations of gas sublimation-driven activity in Mars' southern polar regions: I. Erosion of the surface. *Icarus*, **205**, 283–295, doi:10.1016/j.icarus.2009.07.021.

Hansen, C.J., Bourke, M., Bridges, N.T., Byrne, S., Colon, C., Diniega, S., Dundas, C., Herkenhoff, K., McEwen, A., Mellon, M., Portyankina, G., Thomas, N., 2011. Seasonal erosion and restoration of Mars' northern polar dunes. *Science*, **331**, 575–578, doi:10.1126/science.1197636.

Hansen, C.J., Diniega, S. Bridges, N., Byrne, S., Dundas, C., McEwen, A., Portyankina, G., 2015. Agents of change on Mars' northern dunes: CO_2 ice and wind. *Icarus* **251**, 264–274, doi:10.1016/j.icarus.2014.11.015.

Hansen, C.J., Diniega, S., Hayne, P.O., 2018. Mars' Snowfall and Sand Avalanches. Presented at the *49th Lunar and Planetary Science Conference*, Ab. 2175.

Hansen, C.J., Aye, K.M., Diniega, S., Hayne, P., McEwen, A., Portyankina, G., Schwamb, M.E., 2020. Dynamic Seasons on Mars—Polar Images and Investigations. Presented at the *7th International Conference on Mars Polar Science and Exploration*, Ab. 6019.

Hao, J., Michael, G. G., Adeli, S., Jaumann, R., Portyankina, G., Hauber, E., Millot, C., Zuschneid, W., 2020. Variability of spider spatial configuration at the Martian south pole. *Planet. Space Sci.*, **185**, 104848, doi:10.1016/j.pss.2020.104848.

Harrison, T., Malin, M.C., Edgett, K.S., 2009. Present-day activity, monitoring, and documentation of gullies with the Mars Reconnaissance Orbiter (MRO) Context Camera (CTX). Presented at *Geological Society of America Meeting*, Ab. 97-12.

Harri, A.M., Genzer, M., Kemppinen, O., Kahanpää, H., Gomez-Elvira, J., Rodriguez-Manfredi, J.A., Haberle, R., Polkko, J., Schmidt, W., Savijärvi, H., Kauhanen, J., 2014. Pressure observations by the Curiosity rover: Initial results. *Journal of Geophysical Research: Planets*, **119**(1), 82–92, doi:10.1002/2013JE004423.

Hart, H.M., Jakosky, B.M., 1986. Composition and stability of the condensate observed at the Viking Lander 2 site on Mars. *Icarus*, **66**(1), 134–142, doi:10.1016/0019-1035(86)90013-8.

Hartogh, P., Medvedev, A. S., Kuroda, T., Saito, R., Villanueva, G., Feofilov, A. G., Kutepov, A. A., Berger, U., 2005. Description and climatology of a new general circulation model of the Martian atmosphere. *Journal of Geophysical Research*, **110**, doi:10.1029/2005JE002498.

Hayne, P.O., Paige, D.A., Schofield, J.T., Kass, D.M., Kleinböhl, A., Heavens, N.G., McCleese, D.J., 2012. Carbon dioxide snow clouds on Mars: southern polar winter observations by the Mars Climate Sounder. *Journal of Geophysical Research*, **117**, E8, E08014, doi:10.1029/2011JE004040.

Hayne, P.O., Paige, D.A., Heavens, N.G., 2014. The role of snowfall in forming the seasonal ice caps of Mars: Models and constraints from the Mars Climate Sounder. *Icarus*, **231**, 122–130, doi:10.1016/j.icarus.2013.10.020.

Hayne, P. O., Hansen, C. J., Byrne, S., Kass, D. M., Kleinböhl, A., Piqueux, S., McCleese, D. J., Diniega, S., Portyankina, G., 2016. Snowfall variability and surface changes in the polar regions of Mars. Presented at *6th International Conference on Mars Polar Science and Exploration*, Ab. #6012.

Hayward, R., Mullins, K., Fenton, L., Hare, T., Titus, T., Bourke, M., Colaprete, A., Christensen, P., 2007. Mars global digital dune database: MC2-MC20 Rep. 2331-1258, U.S. Geological Survey.

Hayward, R., Fenton, L., Tanaka, K., Titus, T., Colaprete, A., Christensen, P., 2010. Mars global digital dune database: MC-1 Rep. 2010-1170, U.S. Geological Survey.

Hayward, R., Fenton, L., Titus, T., Colaprete, A., Christensen, P., 2012. Mars global digital dune database: MC-30 Rep. 2331-1258, U.S. Geological Survey.

Hayward, R.K., Fenton, L.K., Titus, T.N., 2014. Mars Global Digital Dune Database (MGD3): Global dune distribution and wind pattern observations. *Icarus*, **230**, 38–46, doi:10.1016/j.icarus.2013.04.011.

Head, J.W., Marchant, D.R., 2003. Cold-based mountain glaciers on Mars: Western Arsia Mons. *Geology*, **31**, 641–644.

2953 Head, J.W., Mustard, J.F., Kreslavsky, M.A., Milliken, R.E., Marchant, D.R., 2003. Recent ice
2954 ages on Mars. *Nature*, **426**(6968), 797–802, doi:10.1038/nature02114.

2955 Heinz, J., Schulze-Makuch, D., Kounaves, S. P., 2016. Deliquescence-induced wetting and RSL-
2956 like darkening of a Mars analogue soil containing various perchlorate and chloride salts.
2957 *Geophysical Research Letters*, **43**, 4880–4884, doi:10.1002/2016GL068919.

2958 Herkenhoff, K.E., Byrne, S., Russell, P.S., Fishbaugh, K.E., McEwen, A.S., 2007. Meter-scale
2959 morphology of the north polar region of Mars. *Science*, **317**, 1711–1715,
2960 doi:10.1126/science.1143544.

2961 Herny, C., Masse, M., Bourgeois, O., Carpy, S., Le Mouelic, S., Appere, T., Smith, I.B., Spiga,
2962 A., Rodriguez, S., 2014. Sedimentation waves on the martian north polar cap: Analogy with
2963 megadunes in Antarctica. *Earth and Planetary Science Letters,* **403**, 56–66,
2964 doi:10.1016/j.epsl.2014.06.033.

2965 Herny, C., Conway, S. J., Raack, J., Carpy, S., Colleu-Banse, T., Patel, M. R., 2019. Downslope
2966 sediment transport by boiling liquid water under Mars-like conditions: experiments and
2967 potential implications for martian gullies. *Geological Society, London, Special Publications*,
2968 467, 373–410, doi:10.1144/SP467.10.

2969 Hess, S.L., Henry, R.M., Leovy, C.B., Ryan, J.A., Tillman, J.E., Chamberlain, T.E., Cole, H.L.,
2970 Dutton, R.G., Greene, G.C., Simon, W.E., Mitchell, J.L., 1976. Preliminary meteorological
2971 results on Mars from the Viking 1 lander. *Science*, **193**(4255), 788–791,
2972 doi:10.1126/science.193.4255.788.

2973 Hoffman, N., 2002. Active polar gullies on Mars and the role of carbon dioxide. *Astrobiology*, **2**,
2974 313–323, doi:10.1089/153110702762027899.

2975 Horgan, B.H.N., Bell III, J. F., 2012. Seasonally active slipface avalanches in the north polar
2976 sand sea of Mars: Evidence for a wind-related origin. *Geophysical Research Letters*, **39**,
2977 L09201, doi:10.1029/2012GL051329.

2978 Houben, H., 1997. Stability of Ground Ice on Mars. Presented at *DPS Meeting*, Ab. 06-06.

2979 Houben, H., Haberle, R.M., Young, R.E., Zent, A.P., 1997a. Modeling the Martian seasonal
2980 water cycle. *Journal of Geophysical Research: Planets*, **102**(E4), 9069–9083.

2981 Howard, A.D., 2000. The role of eolian processes in forming surface features of the martian
2982 polar layered deposits. *Icarus*, **144**, 267–288, doi:10.1006/icar.1999.6305.

2983 Howard, A. D., Moore, J. M., 2008. Sublimation-driven erosion on Callisto: A landform
2984 simulation model test. *Geophysical Research Letters*, **35**(3), L03203,
2985 doi:10.1029/2007GL032618.

2986 Huber, C., Ojha, L., Lark, L., Head, J.W., 2020. Physical models and predictions for recurring
2987 slope lineae formed by wet and dry processes. *Icarus*, **335**, 113385.

2988 Hudson, T.L., Aharonson, O., Schorghofer, N., Farmer, C.B., Hecht, M.H., Bridges, N.T., 2007.
2989 Water vapor diffusion in Mars subsurface environments. *Journal of Geophysical Research:*
2990 *Planets*, **112**(E5), E05016, doi:10.1029/2006JE002815.

2991 Hugenholtz, C.H., 2008. Frosted granular flow: A new hypothesis for mass wasting in martian
2992 gullies. *Icarus*, **197**, 65–72, doi:10.1016/j.icarus.2008.04.010.

2993 Hugenholtz, C.H., Barchyn, T.E., Boulding, A., 2017. Morphology of transverse aeolian ridges
2994 (TARs) on Mars from a large sample: Further evidence of a megaripple origin? *Icarus*, **286**,
2995 193–201, doi:10.1016/j.icarus.2016.10.015.

2996 ICE-SAG, 2019. Report from the Ice and Climate Evolution Science Analysis group (ICE-SAG).
2997 Chaired by S. Diniega and N. E. Putzig, 157 pages posted 08 July 2019, by the Mars
2998 Exploration Program Analysis Group (MEPAG) at http://mepag.nasa.gov/reports.cfm.

2999 ICE-WG, 2015. ISRU and Civil Engineering needs for future human Mars missions. Chaired by
3000 S. Hoffman, posted at
3001 https://mepag.jpl.nasa.gov/reports/HLS2%20briefing%2027Oct15%20ICEWG%20v2.pdf

3002 Ingersoll, A.P., 1970. Mars: Occurrence of liquid water. *Science*, **168**(3934), 972–973.

3003 Ingersoll, A. P., 1990. Dynamics of Triton's Atmosphere. *Nature,* **344**, 315–317.

3004 Ishii, T., Sasaki, S., 2004. Formation of recent Martian gullies by avalanches of CO_2 Frost.
3005 Presented at *35th Lunar and Planetary Science Conference*, Ab. #1556.

3006 Iversen, J.D., White, B.R., 1982. Saltation threshold on Earth, Mars and Venus. *Sedimentology*,
3007 **29**(1), 111-119.

3008 Jackson, B., Lorenz, R.D., Barnes, J.W., Szurgot, M., 2020. Dust devils on Titan. *Journal of*
3009 *Geophysical Research: Planets*, **125**, e2019JE006238, doi:10.1029/2019JE006238.

3010 Jakosky, B.M., Haberle, R.M., 1990. Year-to-year instability of the Mars south polar cap.
3011 *Journal of Geophysical Research*, **95**(B2), 1359–1365, doi:10.1029/JB095iB02p01359.

3012 Jakosky, B.M., Mellon, M.T., Varnes, E.S., Feldman, W.C., Boynton, W.V., Haberle, R.M.,
3013 2005. Mars low-latitude neutron distribution: Possible remnant near-surface water ice and a
3014 mechanism for its recent emplacement. *Icarus*, **175**(1), 58–67,
3015 doi:10.1016/j.icarus.2004.11.014.

3016 James, P.B., Kieffer, H.H., Paige, D.A., 1992. The seasonal cycle of carbon dioxide on Mars.
3017 *Mars*, 934–968.

3018 Jerolmack, D.J., Mohrig, D., Grotzinger, J.P., Fike, D.A., Watters, W.A., 2006. Spatial grain
3019 size sorting in eolian ripples and estimation of wind conditions on planetary surfaces:
3020 Application to Meridiani Planum, Mars. *Journal of Geophysical Research,* **111,** E12S02,
3021 doi:10.1029/2005JE002544.

3022 Jia, P., Andreotti, B., Claudin, P., 2017. Giant ripples on comet 67P/Churyumov–Gerasimenko
3023 sculpted by sunset thermal wind. *Proceedings of the National Academy of Science of U.S.A.*,
3024 **114**(10), 2509–2514, doi:10.1073/pnas.1612176114.

3025 Johnson, F.S., 1965. Atmosphere of Mars. *Science,* **150**(3702), 1445–1448,
3026 doi:10.1126/science.150.3702.1445

3027 Johnson, J.R., Achilles, C., Bell III, J.F., Bender, S., Cloutis, E., Ehlmann, B., Fraeman, A.,
3028 Gasnault, O., Hamilton, V.E., Le Mouélic, S., Maurice, S., 2017. Visible/near-infrared
3029 spectral diversity from in situ observations of the Bagnold dune field sands in Gale crater,
3030 Mars. *Journal of Geophysical Research: Planets*, **122**, 2655–2684,
3031 doi:10.1002/2016JE005187.

3032 Johnson, J.R., Bell III, J.F., Bender, S., Cloutis, E., Ehlmann, B., Fraeman, A., Gasnault, O.,
3033 Maurice, S., Pinet, P., Thompson, L., Wellington, D., 2018. Bagnold Dunes campaign Phase

2: Visible/near-infrared reflectance spectroscopy of longitudinal ripple sands. *Geophysical Research Letters*, **45**(18), 9480–948, doi:10.1029/2018GL079025.

Jouannic, G., Gargani, J., Costard, F., Ori, G.G., Marmo, C., Schmidt, F., Lucas, A., 2012. Morphological and mechanical characterization of gullies in a periglacial environment: The case of the Russell crater dune (Mars). *Planetary and Space Science*, **71**(1), 38–54, doi:10.1016/j.pss.2012.07.005.

Jouannic, G., Conway, S.J., Gargani, J., Costard, F., Massé, M., Bourgouis, O., Carter, J., Schmidt, F., Marmo, C., Ori, G.G., Nachon, M., Pasquon, K., 2019. Morphological characterization of landforms produced by springtime seasonal activity on Russell crater megadune, Mars. *Geol. Soc. London Spec. Pub.*, **467**, 115–144, doi:10.1144/SP467.16.

Lämmel, M., Meiwald, A., Yizhaq, H., Tsoar, H., Katra, I., Kroy, K., 2018. Aeolian sand sorting and megaripple formation. *Nature Physics*, **14**, 759–765, doi:10.1038/s41567-018-0106-z.

Kaufmann, E., Hagermann, A., 2017. Experimental investigation of insolation-driven dust ejection from Mars' CO_2 ice caps. *Icarus*, **282**, 118–126, doi:10.1016/j.icarus.2016.09.039.

Kessler, M.A., Werner, B.T., 2003. Self-organization of sorted patterned ground. *Science*, **299**(5605), 380–383, doi:10.1126/science.1077309.

Kieffer, H.H., 2007. Cold jets in the martian polar caps. *Journal of Geophysical Research: Planets*, **112**, E08005, doi:10.1029/2006JE002816.

Kieffer, H.H., Christensen, P.R., Titus, T.N., 2006. CO_2 jets formed by sublimation beneath translucent slab ice in Mars' seasonal south polar ice cap. *Nature,* **442**, 793-796, doi:10.1038/nature04945.

Kite, E.S., Mayer, D.P., 2017. Mars sedimentary rock erosion rates constrained using crater counts, with applications to organic-matter preservation and to the global dust cycle. *Icarus*, **286**, 212–222, doi:10.1016/j.icarus.2016.10.010.

Kminek, G., Conley, C., Hipkin, V., Yano, H., 2017. COSPAR's planetary protection policy. *Space Research Today*, **200**, 12–25, doi:10.1016/j.srt.2017.11.010.

Kocurek, G., Lancaster, N., 1999. Aeolian system sediment state: theory and Mojave Desert Kelso dune field example. *Sedimentology*, **46**(3), 505–515.

Kok, J.F., 2010. An improved parameterization of wind-blown sand flux on Mars that includes the effect of hysteresis. *Geophysical Research Letters*, **37**, L12202, doi:10.1029/2010GL043646.

Kok, J.F., Renno, N.O., 2006.Enhancement of the emission of mineral dust aerosols by electric forces. *Geophysical Research Letters*, **33**, L19S10, doi:10.1029/2006GL026284.

Kok, J.F., Renno, N.O., 2009. A comprehensive numerical model of steady state saltation (COMSALT). *Journal of Geophysical Research*, **114**, D17204, doi:10.1029/2009JD011702.

Kok, J.F., Parteli, E.J.R., Michaels, T.I., Bou Karam, D., 2012. The physics of windblown sand and dust. *Rep. Prog. Phys.*, **75**, 106901, doi:10.1088/0034-4885/75/10/106901.

Kolb, K.J., Pelletier, J.D., McEwen, A.S., 2010. Modeling the formation of bright slope deposits associated with gullies in Hale crater, Mars: Implications for recent liquid water. *Icarus*, **205**, 113–137, doi:10.1016/j.icarus.2009.09.009.

Kreslavsky M.A., Head, J.W., 2011. Carbon dioxide glaciers on Mars: Products of recent low obliquity epochs (?). *Icarus*, **216**, 111–115, doi:10.1016/j.icarus.2011.08.020.

Kreslavsky, M.A., Head, J.W., Marchant, D.R., 2008. Periods of active permafrost layer formation during the geological history of Mars: Implications for circum-polar and mid-latitude surface processes. *Planetary and Space Science*, **56**(2), 289–302, doi:10.1016/j.pss.2006.02.010.

Krinsley, D.H., Smalley, I.J., 1972. Sand: The study of quartz sand in sediments provides much information about ancient geological environments. *American Scientist*, **60**(3), 286-291.

Krohn, K., Jaumann, R., Otto, K., Hoogenboom, T., Wagner, R., Buczkowski, D.L., Garry, B., Williams, D.A., Yingst, R.A., Scully, J., De Sanctis, M.C., Kneissl, T., Schmedemann, N., Kersten, E., Stephan, K., Matz, K.-D., Pieters, C.M., Preusker, F., Roatsch, T., Schenk, P., Russell, C.T., Raymond, C.A., 2014. Mass movement on Vesta at steep scarps and crater rims. *Icarus*, **244**, 120–132, doi:10.1016/j.icarus.2014.03.013.

Laity, J.E., Bridges, N.T., 2009. Ventifacts on Earth and Mars: Analytical, field, and laboratory studies supporting sand abrasion and windward feature development. *Geomorphology*, **105**(3–4), 202–217, doi:10.1016/j.geomorph.2008.09.014.

Lancaster, N., Greeley, R., 1990. Sediment volume in the north polar sand seas of Mars. *Journal of Geophysical Research*, **95**, 10921–10927, doi:10.1029/JB095iB07p10921.

Langevin, Y., Poulet, F., Bibring, J.-P., Schmitt, B., Douté, S., Gondet, B., 2005. Summer evolution of the north polar cap of Mars as observed by OMEGA/Mars express. *Science*, **307**(5715), 1581–1584.

Langevin, Y., Bibring, J.-P., Montmessin, F., Forget, F., Vincendon, M., Douté, S., Poulet, F. and Gondet, B., 2007. Observations of the south seasonal cap of Mars during recession in 2004–2006 by the OMEGA visible/near-infrared imaging spectrometer on board Mars Express. *Journal of Geophysical Research: Planets*, **112**, E08S12, doi:10.1029/2006JE002841.

Landis, G.A., 2007. Observation of frost at the equator of Mars by the Opportunity rover. Presented at *38th Lunar and Planetary Science Conference*, Ab. 2423.

Landis, M.E., Byrne, S., Daubar, I.J., Herkenhoff, K.E., Dundas, C.M., 2016. A revised surface age for the north polar layered deposits of Mars. *Geophysical Research Letters*, **43**(7), 3060–3068, doi:10.1002/2016GL068434.

Lane, M.D., Christensen, P.R., 2013. Determining olivine composition of basaltic dunes in Gale crater, Mars, from orbit: Awaiting ground truth from Curiosity. *Geophysical Research Letters*, **40**(14), 3517–3521, doi:10.1002/grl.50621.

Lapôtre, M.G.A., Lamb, M., McElroy, B., 2017. What sets the size of current ripples? *Geology*, **45**(3), 243–246, doi:10.1130/G38598.1.

Lapôtre, M.G.A., Rampe, E., 2018. Curiosity's investigation of the Bagnold Dunes, Gale crater: Overview of the two-phase scientific campaign and introduction to the special collection. *Geophysical Research Letters*, **45**, 10200–10210, doi:10.1029/2018GL079032.

Lapôtre, M.G.A., Ewing, R.C., Lamb, M.P., Fischer, W.W., Grotzinger, J.P., Rubin, D.M., Lewis, K.W., Ballard, M.J., Day, M., Gupta, S., Banham, S.G., Bridges, N.T., Des Marais, D.J., Fraeman, A.A., Grant, J.A., Herkenhoff, K.E., Ming, D.W., Mischna, M.A., Rice, M.S.,

Sumner, D.Y., Vasavada, A.R., Yingst, R.A., 2016. Large wind ripples on Mars: A record of atmospheric evolution. *Science*, **353**, 6294, 55–58.

Lapôtre, M.G.A., Ehlmann, B.L., Minson, S.E., Arvidson, R.E., Ayoub, F., Fraeman, A.A., Ewing, R.C., Bridges, N.T., 2017. Compositional variations in sands of the Bagnold dunes, Gale crater, Mars, from visible-shortwave infrared spectroscopy and comparison with ground truth from the Curiosity rover. *Journal of Geophysical Research: Planets*, **122**, 2489–2509, doi:10.1002/2016JE005133.

Lapôtre, M.G.A., Ewing, R. C., Weitz, C. M., Lewis, K.W., Lamb, M.P., Ehlmann, B.L., Rubin, D.M., 2018. Morphologic diversity of martian ripples: Implications for large-ripple formation. *Geophysical Research Letters*, 45(19), 10,229–10,239, doi:10.1029/2018GL079029.

Lapôtre, M.G.A., O'Rourke, J.G., Schaefer, L.K., Siebach, K.L., Spalding, C., Tikoo, S.M., Wordsworth, R.D., 2020. Probing space to understand Earth. *Nature Reviews Earth and Environment*, **1**, 170–181, doi:10.1038/s43017-020-0029-y.

Lapôtre, M.G.A., Ewing, R. C., Lamb, M.P., 2021. An evolving understanding of enigmatic large ripples on Mars. *Journal of Geophysical Research: Planets*, in press.

Laskar, J., Correia, A.C.M., Gastineau, M., Joutel, F., Levrard, B., Robutel, P., 2004. Long term evolution and chaotic diffusion of the insolation quantities of Mars. *Icarus*, **170**(2), 343–364, doi:10.1016/j.icarus.2004.04.005.

Lasue, J., Cousin, A., Meslin, P.Y., Mangold, N., Wiens, R.C., Berger, G., Dehouck, E., Forni, O., Goetz, W., Gasnault, O., Rapin, W., 2018. Martian eolian dust probed by ChemCam. *Geophysical Research Letters*, **45**(20), 10,968-10,977, doi:10.1029/2018GL079210.

Leask, E.K., Ehlmann, B.L., Dundas, M.M., Murchie, S.L., Seelos, F.P., 2018. Challenges in the search for perchlorate and other hydrated minerals with 2.1- μm absorptions on Mars. *Geophysical Research Letters*, **45**, 12,180–12,189, doi:10.1029/2018GL080077.

Lefort, A., Russell, P.S., Thomas, N., McEwen, A.S., Dundas, C.M., Kirk, R.L., 2009. Observations of periglacial landforms in Utopia Planitia with the High Resolution Imaging Science Experiment (HiRISE). *Journal of Geophysical Research*, **114**, E04005, doi:10.1029/2008JE003264.

Lefort, A., Russell, P.S., Thomas, N., 2010. Scalloped terrains in the Peneus and Amphitrites Paterae region of Mars as observed by HiRISE. *Icarus*, **205**, 259–268, doi:10.1016/j.icarus.2009.06.005.

Leighton, R.B., Murray, B.C., 1966. Behavior of carbon dioxide and other volatiles on Mars. *Science*, **153**, 136–144, doi:10.1126/science.153.3732.136.

Leprince, S., Barbot, S., Ayoub, F., Avouac, J.-P., 2007. Automatic and precise orthorectification, coregistration, and subpixel correlation of satellite images, application to ground deformation measurements. *IEEE Transactions on Geoscience and Remote Sensing*, **45**, 1529–1558, doi:10.1109/TGRS.2006.888937.

Levrard, B., Forget, F., Montmessin, F., Laskar, J., 2007. Recent formation and evolution of northern martian polar layered deposits as inferred from a global climate model. *Journal of Geophysical Research*, **112**, E06012.doi:10.1029/2006JE002772.

Levy, J., 2012. Hydrological characteristics of recurrent slope lineae on Mars: Evidence for liquid flow through regolith and comparisons with Antarctic terrestrial analogs. *Icarus*, 219, 1–4, doi:10.1016/j.icarus.2012.02.016.

Levy, J.S., Marchant, D.R., Head, J.W., 2006. Distribution and origin of patterned ground on Mullins Valley debris-covered glacier, Antarctica: The roles of ice flow and sublimation. *Antarctic Science*, **18**(3), 385.

Levy, J.S., Head, J.W., Marchant, D.R., 2009a. Concentric crater fill in Utopia Planitia: History and interaction between glacial "brain terrain" and periglacial mantle processes. *Icarus*, **202**, 462–476, doi:10.1016/j.icarus.2009.02.018.

Levy, J., Head, J., Marchant, D., 2009b. Thermal contraction crack polygons on Mars: Classification, distribution, and climate implications from HiRISE observations. *Journal of Geophysical Research: Planets*, **114**(E1), E01007, doi:10.1029/2008JE003273.

Levy, J.S., Marchant, D.R., Head, J.W., 2010. Thermal contraction crack polygons on Mars: A synthesis from HiRISE, Phoenix, and terrestrial analog studies. *Icarus*, **206**(1), 229–252, doi:10.1016/j.icarus.2009.09.005.

Levy, J.S., Fassett, C.I., Rader, L.X., King, I.R., Chaffey, P.M., Wagoner, C.M., Hanlon, A.E., Watters, J.L., Kreslavsky, M.A., Holt, J.W., Russell, A.T., 2018. Distribution and characteristics of boulder halos at high latitudes on Mars: Ground ice and surface processes drive surface reworking. *Journal of Geophysical Research: Planets*, **123**(2), 322–334, doi:10.1002/2017JE005470.

Liu, J., Di, K., Gou, S., Yue, Z, Liu, B., Xiao, J., Liu, Z., 2020. Mapping and spatial statistical analysis of Mars yardangs. *Planetary and Space Science*, **192**, 105035, doi:10.1016/j.pss.2020.105035.

Lorenz, R.D., 1996. Martian surface wind speeds described by the Weibull distribution. *Journal of Spacecraft and Rockets*, **33**, 754-756.

Lorenz, R.D., McKay, C.P., Lunine, J.I., 1997. Photochemically driven collapse of Titan's atmosphere. *Science*, **275**, 642–644.

Lorenz, R.D., Wall, S., Radebaugh, J., Boubin, G., Reffet, E., Janssen, M., Stofan, E., Lopes, R., Kirk, R., Elachi, C., Lunine, J., 2006. The sand seas of Titan: Cassini RADAR observations of longitudinal dunes. *Science*, **312**, 724–727, doi:10.1126/science.1123257.

Lorenz, R.D., Bridges, N.T., Rosenthal, A.A., Donkor, E., 2014. Elevation dependence of bedform wavelength on Tharsis Montes, Mars: Atmospheric density as a controlling parameter. *Icarus*, **230**, 77–80.

Lowell, 1895. https://en.wikisource.org/wiki/Mars_(Lowell): Mars (Lowell). (2012, October 5). In *Wikisource* . Retrieved 06:58, July 3, 2020, from https://en.wikisource.org/w/index.php?title=Mars_(Lowell)&oldid=4087387

Malin, M.C., Edgett, K.S., 2000. Evidence for recent groundwater seepage and surface runoff on Mars. *Science*, **288**(5475), 2330–2335, doi:10.1126/science.288.5475.2330.

Malin, M.C., Edgett, K.S., 2001. Mars Global Surveyor Mars Orbiter Camera: Interplanetary cruise through primary mission. *Journal of Geophysical Research,* **106**, 23,429–23,570, doi:10.1029/2000JE001455.

Malin, M.C., Danielson, G.E., Ingersoll, A.P., Masursky, H., Veverka, J., Ravine, M.A., Soulanille, T.A., 1992. Mars Observer Camera. *Journal of Geophysical Research,* **97**, 7699, doi:10.1029/92JE00340.

Malin, M.C., Caplinger, M.A., Davis, S.D., 2001. Observational evidence for an active surface reservoir of solid carbon dioxide on Mars. *Science*, **294**(5549), 2146–2148.

Malin, M.C., Edgett, K.S., Posiolova, L.V., McColley, S.M., Noe Dobrea, E.Z., 2006. Present-day impact cratering rate and contemporary gully activity on Mars. *Science*, **314**, 1573-1577, doi:10.1126/science.1135156.

Malin, M.C., Bell, J.F., Cantor, B.A., Caplinger, M.A., Calvin, W.M., Clancy, R.T., Edgett, K.S., Edwards, L., Haberle, R.M., James, P.B., Lee, S.W., 2007. Context camera investigation on board the Mars Reconnaissance Orbiter. *Journal of Geophysical Research*, **112**, E05S04, doi:10.1029/2006JE002808.

Malin, M.C., Edgett, K.S., Cantor, B.A., Caplinger, M.A., Danielson, G.E., Jensen, E.H., Ravine, M.A., Sandoval, J.L., Supulver, K.D., 2010. An overview of the 1985–2006 Mars Orbiter Camera science investigation. *Mars*, **5**, 1–60.

Malliband, C.C., Conway, S.J., Rothery, D.A., Balme, M.R., 2019. Potential identification of downslope mass movements on Mercury driven by volatile-loss. Presented at the *50th Lunar and Planetary Science Conference*, Ab. 1804.

Mangold, N., 2003. Geomorphic analysis of lobate debris aprons on Mars at Mars Orbiter Camera scale: Evidence for ice sublimation initiated by fractures. *Journal of Geophysical Research*, 108(E4), 8021 doi:10.1029/2002JE001885.

Mangold, N., 2005. High latitude patterned grounds on Mars: Classification, distribution and climatic control. *Icarus*, **174**(2), 336–359, doi:10.1016/j.icarus.2004.07.030.

Mangold, N., 2011. Ice sublimation as a geomorphic process: A planetary perspective. *Geomorphology*, 126, 1–17, doi:10.1016/j.geomorph.2010.11.009.

Mangold, N., Costard, F., Forget, F., 2003. Debris flows over sand dunes on Mars: Evidence for liquid water. *Journal of Geophysical Research*, 108, doi:10.1029/2002JE001958.

Mangold, N., Mangeney, A., Migeon, V., Ansan, V., Lucas, A., Baratoux, D., Bouchut, F., 2010. Sinuous gullies on Mars: Frequency, distribution, and implications for flow properties. *Journal of Geophysical Research: Planets*, **115**, E11001, doi:10.1029/2009JE003540.

Manning, C.V., Bierson, C., Putzig, N.E. McKay, C.P., 2019. The formation and stability of buried polar CO_2 deposits on Mars. *Icarus*, **317**, 509–517, doi:10.1016/j.icarus.2018.07.021.

Marchant, D.R., Denton, G.H., Sugden, D.E., Swisher, C.C., 1993. Miocene glacial stratigraphy and landscape evolution of the western Asgard Range, Antarctica. *Geografiska Annaler* **75**A, 303–330.

Marchant, D.R., Lewis, A.R., Phillips, W.M., Moore, E.J., Souchez, R.A., Denton, G.H., Sugden, D.E., Potter, N., Landis, G.P., 2002. Formation of patterned ground and sublimation till over Miocene glacier ice in Beacon Valley, southern Victoria Land, Antarctica. *Geological Society of America Bulletin*, 114(6), 718–730.

Martínez, G.M., Newman, C.N., De Vicente-Retortillo, A., Fischer, E., Renno, N.O., Richardson, M.I., Fairén, A.G., Genzer, M., Guzewich, S.D., Haberle, R.M., Harri, A.M., 2017. The modern near-surface martian climate: A review of in-situ meteorological data

from Viking to Curiosity. *Space Science Reviews*, **212**(1-2), 295–338, doi:10.1007/s11214-017-0360-x.

Masursky, H., 1973. An overview of geological results from Mariner 9. *Journal of Geophysical Research,* **78**(20), 4009–4030, doi:10.1029/JB078i020p04009.

Massé, M., Bourgeois, O., Lemouélic, S., Verpoorter, C., Spiga, A., Le Deit, L. 2012. Wide distribution and glacial origin of polar gypsum on Mars. *Earth and Planetary Science Letters*, **317–318**, 44–55, doi:10.1016/j.epsl.2011.11.035.

Massé, M., Conway, S.J., Gargani, J., Patel, M.R., Pasquon, K., McEwen, A., Carpy, S., Chevrier, V., Balme, M.R., Ojha, L., Vincendon, M., 2016. Transport processes induced by metastable boiling water under martian surface conditions. *Nature Geoscience*, **9**(6), 425–428, doi:10.1038/ngeo2706.

Matson, D.L., Brown, R.H., 1989. Solid-state greenhouse and their implications for icy satellites. *Icarus*, **77**(1), 67–81, doi:10.1016/0019-1035(89)90007-9.

Matsuo, K., Heki, K., 2009. Seasonal and inter-annual changes of volume density of martian CO_2 snow from time-variable elevation and gravity. *Icarus*, **202**, 90–94, doi:10.1016/j.icarus.2009.02.023.

Maus, D., Heinz, J., Schirmack, J., Airo, A., Kounaves, S. P., Wagner, D., Schulze-Makuch, D., 2020. Methanogenic Archaea can produce methane in deliquescence-driven Mars analog environments. *Scientific Reports*, **10**, 6, doi:10.1038/s41598-019-56267-4.

McEwen, A.S., 2018. Are recurring slope lineae habitable? In *From Habitability to Life on Mars*, N.A. Cabrol and E.A. Grin, Editors, Chapter 10, Elsevier Inc., 249–274, doi:10.1016/B978-0-12-809935-3.00008-6.

McEwen, A.S., Eliason, E.M., Bergstrom, J.W., Bridges, N.T., Hansen, C.J., Delamere, W.A., Grant, J.A., Gulick, V.C., Herkenhoff, K.E., Keszthelyi, L., Kirk, R.L., 2007. Mars Reconnaissance Orbiter's High Resolution Imaging Science Experiment (HiRISE). *Journal of Geophysical Research*, **112**, E05S02, doi:10.1029/2005JE002605.

McEwen, A.S., Ojha, L., Dundas, C.M., Mattson, S.S., Byrne, S., Wray, J.J., Cull, S.C., Murchie, S.L., Thomas, N., Gulick, V.C., 2011. Seasonal flows on warm martian slopes. *Science,* 333, 740–743, doi:10.1126/science.1204816.

McEwen, A.S., Dundas, C.M., Mattson, S.S., Toigo, A.D, Ojha, L., Wray, J.J., Chojnacki, M., Byrne, S., Murchie, S.L., Thomas, N., 2014. Recurring slope lineae in equatorial regions of Mars. *Nature Geoscience*, **7**, 53–58, doi:10.1038/ngeo2014.

McEwen, A.S., Schaefer, E., Sutton, S., Chojnacki, M., 2019. Remarkably widespread RSL activity following the great martian dust storm of 2018. Presented at *EPSC-DPS Joint Meeting 2019*, Ab. EPSC-DPS2019-557.

McEwen, A.S., Schafer, E.I., Dundas, C.M., Sutton, S. S., Tamppiri, L. K., Chojnacki, M., 2021. Mars: Abundant recurring slope lineae (RSL) following the planet-encircling dust event (PEDE) of 2018. *Journal of Geophysical Research: Planets*, JGRE_21573, doi: 10.1029/2020JE006575.

McGlynn, I.O., Fedo, C.M., McSween Jr., H.Y., 2011. Origin of basaltic soils at Gusev crater, Mars, by aeolian modification of impact-generated sediment. *Journal of Geophysical Research: Planets*, **116**(E7), E00F22, doi:10.1029/2010JE003712.

McKee, E.D., 1979. Introduction to a study of global sand seas. In *A Study of Global Sand Seas*. U.S. Geol. Surv. Prof. Pap. **1052**: 3–17.

Mc Keown, L.E., Bourke, M.C., McElwaine, J.N., 2017. Experiments on sublimating carbon dioxide ice and implications for contemporary surface processes on Mars. *Scientific Reports*, **7**, 14181, doi:10.1038/s41598-017-14132-2.

Mc Keown, L.E., Bourke, M.C., McElwaine, J.N., Sylvest, M.E., Patel, M.R., 2021. The formation of araneiforms by carbon dioxide venting and vigorous sublimation dynamics under martian conditions. *Scientific Reports*, in press, https://www.essoar.org/doi/10.1002/essoar.10501015.1

McLennan, S.M., Grotzinger, J.P., Hurowitz, J.A., Tosca, N.J., 2019. The sedimentary cycle on Early Mars. *Annual Review of Earth and Planetary Sciences*, **47**, 91–118, doi:10.1146/annurev-earth-053018-060332.

McSween, H.Y., Arvidson, R.E., Bell, J.F., Blaney, D., Cabrol, N.A., Christensen, P.R., Clark, B.C., Crisp, J.A., Crumpler, L.S., Des Marais, D.J., Farmer, J.D., 2004. Basaltic rocks Aanalyzed by the Spirit rover in Gusev crater. *Science*, **305**, 842–845, doi:10.1126/science.3050842.

Mellon, M.T., 1997. Small-scale polygonal features on Mars: Seasonal thermal contraction cracks in permafrost. *Journal of Geophysical Research*, 102(E11), 25617–25628.

Mellon, M.T., Jakosky, B.M., 1993. Geographic variations in the thermal and diffusive stability of ground ice on Mars. *Journal of Geophysical Research*, 98, 3,345–3,364.

Mellon, M.T., Jakosky, B.M., 1995. The distribution and behavior of martian ground ice during past and present epochs. *Journal of Geophysical Research*, 100, 11,781–11,799.

Mellon, M. T., Jakosky, B.M., Postawko, S.E., 1997. The persistence of equatorial ground ice on Mars. *Journal of Geophysical Research*, 102, 19,357–19,369.

Mellon, M.T., Feldman, W.C., Prettyman, T.H., 2004. The presence and stability of ground ice in the southern hemisphere of Mars. *Icarus*, **169**, 324–340, doi:10.1016/j.icarus.2003.10.022.

Mellon, M.T., Arvidson, R.E., Marlow, J.J., Phillips, R.J., Asphaug, E., 2008. Periglacial landforms at the Phoenix landing site and the northern plains of Mars. *Journal of Geophysical Research*, **113**, E00A23, doi:10.1029/2007JE003039.

MEPAG, 2020. Mars Scientific Goals, Objectives, Investigations, and Priorities: 2020. D. Banfield, ed., 89 p. white paper posted March, 2020 by the Mars Exploration Program Analysis Group (MEPAG) at https://mepag.jpl.nasa.gov/reports.cfm.

Milkovich, S.M., Byrne, S., Russell, P.S., 2012. Variations in surface texture of the north polar residual cap of Mars. Presented at the *43rd Lunar and Planetary Science Conference*, Ab. 2226.

Milliken, R.E., Mustard, J.F., Goldsby, D.L., 2003. Viscous flow features on the surface of Mars: Observations from high–resolution Mars Orbiter Camera (MOC) images. *Journal of Geophysical Research: Planets*, **108**, 5057, doi:10.1029/2002JE002005.

Milliken, R.E., Ewing, R.C., Fischer, W.W., Hurowitz, J., 2014. Wind-blown sandstones cemented by sulfate and clay minerals in Gale Crater, Mars. *Geophysical Research Letters*, **41**, 2013GL059097, doi:10.1002/2013GL059097.

Ming, D.W., Gellert, R., Morris, R.V., Arvidson, R.E., Brueckner, J., Clark, B.C., Cohen, B.A., d'Uston, C., Economou, T., Fleischer, I., Klingelhoefer, G., 2008. Geochemical properties of rocks and soils in Gusev crater, Mars: Results of the Alpha-Particle X-Ray Spectrometer from Cumberland Ridge to Home Plate. *Journal of Geophysical Research*, 113, E12S39, doi:10.1029/2008JE003195.

Minitti, M.E., Kah, L.C., Yingst, R.A., Edgett, K.S., Anderson, R.C., Beegle, L.W., Carsten, J.L., Deen, R.G., Goetz, W., Hardgrove, C., Harker, D.E., 2013. MAHLI at the Rocknest sand shadow: Science and science-enabling activities. *Journal of Geophysical Research: Planets*, **118**(11), 2338–2360, doi:10.1002/2013JE004426.

Miyamoto, H., Dohm, J.M., Baker, V.R., Beyer, R.A., Bourke, M., 2004. Dynamics of unusual debris flows on martian sand dunes. *Geophysical Research Letters*, **31**, L13701, doi:10.1029/2004GL020313.

Möhlmann, D.T.F., Thomsen, K., 2011. Properties of cryobrines on Mars. *Icarus*, 212, 123–130.

Monin, A.S., Obukhov, A.M., 1954. Basic laws of turbulent mixing in the surface layer of the atmosphere. *Contrib. Geophys. Inst. Acad. Sci. USSR*, **151**(163), e187.

Moore, H.J., Bickler, D.B., Crisp, J.A., Eisen, H.J., Gensler, J.A., Haldemann, A.F.C., Matijevic, J.R., Reid, L.K., Pavlics, F., 1999. Soil-like deposits observed by Sojourner, the Pathfinder rover. *Journal of Geophysical Research*, **104**, 8729, doi:10.1029/1998JE900005.

Moore, J.M., Mellon, M.T., Zent, A.P., 1996. Mass wasting and ground collapse in terrains of volatile-rich deposits as a solar system-wide geological process: The pre-Galileo view. *Icarus*, **122** (1), 63–78, doi:10.1006/icar.1996.0109.

Moore, J.M., McKinnon, W.B., Spencer, J.R., Howard, A.D., Schenk, P.M., Beyer, R.A., Nimmo, F., Singer, K.N., Umurhan, O.M., White, O.L., Stern, S.A., 2016. The geology of Pluto and Charon through the eyes of New Horizons. *Science*, **352**, 1284–1293.

Moore, J.M., Howard, A.D., Umurhan, O.M., White, O.L., Schenk, P.M., Beyer, R.A., McKinnon, W.B., Spencer, J.R., Grundy, W.M., Lauer, T.R., Nimmo, F., Young, L.A., Stern, S.A., Weaver, H.A., Olkin, C.B., Ennico, K., 2017. Sublimation as a landform-shaping process on Pluto. *Icarus*, **287**, 320–333, doi:10.1016/j.icarus.2016.08.025.

Moores, J.E., Smith, C.L., Toigo, A.D., Guzewich, S.D., 2017. Penitentes as the origin of the bladed terrain of Tartarus Dorsa on Pluto. *Nature*, **541**(7636), 188–190, doi:10.1038/nature20779.

Morgenstern, A., Hauber, E., Reiss, D., van Gasselt, S., Grosse, G., Schirrmeister, L., 2007. Deposition and degradation of a volatile-rich layer in Utopia Planitia and implications for climate history on Mars. *Journal of Geophysical Research*, **112**, E06010.

Morris, R.V., Klingelhoefer, G., Schröder, C., Rodionov, D.S., Yen, A., Ming, D.W., De Souza, P.A., Fleischer, I., Wdowiak, T., Gellert, R., Bernhardt, B., 2006. Mössbauer mineralogy of rock, soil, and dust at Gusev Crater, Mars: Spirit's journey through weakly altered olivine basalt on the plains and pervasively altered basalt in the Columbia Hills. *Journal of Geophysical Research*, **111**, E02S13, doi:10.1029/2005JE002584.

Murchie, S., Arvidson, R., Bedini, P., Beisser, K., Bibring, J.-P., Bishop, J., Boldt, J., Cavender, P., Choo, T., Clancy, R.T., Darlington, E.H., 2007. Compact reconnaissance imaging

spectrometer for Mars (CRISM) on Mars reconnaissance orbiter (MRO). *Journal of Geophysical Research: Planets*, **112**, E05S03, doi:10.1029/2006JE002682.

Munaretto, G., Pajola, M., Cremonese, G., Re, C., Lucchetti, A., Simioni, E., McEwen, A. S., Pommerol, A., Becerra, P., Conway, S. J., Thomas, N., Massironi, M., 2020. Implications for the origin and evolution of martian Recurring Slope Lineae at Hale crater from CaSSIS observations. *Planetary and Space Science*, **187**, 104947.

Mustard, J.F., Cooper, C.D., Rifkin, M.K., 2001. Evidence for recent climate change on Mars from the identification of youthful near-surface ground ice. *Nature*, **412**, 411–414, doi:10.1038/35086515.

Neakrase, L.D.V., Klose, M., Titus, T.N., 2017. Terrestrial subaqueous seafloor dunes: Possible analogs for Venus. *Aeolian Research*, **26**, 47–56, doi:10.1016/j.aeolia.2017.03.002.

Neukum, G., Jaumann, R., the HRSC Co-Investigator Team, 2004a. HRSC: The High Resolution Stereo Camera of Mars Express. European Space Agency SP-1240, 17–36.

Neukum, G., Jaumann, R., Hoffmann, H., Hauber, E., Head, J.W., Basilevsky, A.T., Ivanov, B.A., Werner, S.C., Van Gasselt, S., Murray, J.B., McCord, T., 2004b. Recent and episodic volcanic and glacial activity on Mars revealed by the High Resolution Stereo Camera. *Nature*, **432**(7020), 971–979, doi:10.1038/nature03231.

NEX-SAG, 2015. Report from the Next Orbiter Science Analysis Group (NEX-SAG), chaired by B. Campbell and R. Zurek. 77 pages posted December, 2015 by the Mars Exploration Program Analysis Group (MEPAG) at http://mepag.nasa.gov/reports.cfm.

Newman, C.E., Gomez-Elvira, J., Marin, M., Navarro, S., Torres, J., Richarson, M.I., Battalio, J.M., Guzewich, S.D., Sullivan, R., de la Torre, M., Vasavada, A.R., Bridges, N.T. 2017. Winds measured by the Rover Environmental Monitoring Station (REMS) during the Mars Science Laboratory (MSL) rover's Bagnold dunes campaign and comparison with numerical modeling using MarsWRF. *Icarus*, **291**, 203–231, doi: 10.1016/j.icarus.2016.12.016

Nguyen, T.G., Radebaugh, J., Innanen, A., Moores, J.E., 2020. A survey of small-scale (<50 m) surface features on the martian north polar cap using HiRISE. *Planetary and Space Science*, **182**, 104809, doi:10.1016/j.pss.2019.104809.

O'Connell-Cooper, C.D., Spray, J.G., Thompson, L.M., Gellert, R., Berger, J.A., Boyd, N.I., Desouza, E.D., Perrett, G.M., Schmidt, M., VanBommel, S.J., 2017. APXS-derived chemistry of the Bagnold dune sands: Comparisons with Gale crater soils and the global martian average. *Journal of Geophysical Research: Planets*, **122**, 2623–2643, doi:10.1002/2017JE005268.

O'Connell-Cooper, C.D., Thompson, L.M., Spray, J.G., Berger, J.A., VanBommel, S.J., Gellert, R., Boyd, N.I., DeSouza, E., 2018. Chemical diversity of sands within the linear and barchan dunes of the Bagnold dunes, Gale crater, as revealed by APXS onboard Curiosity. *Geophysical Research Letters*, **45**(18), 9460–9470, doi:10.1029/2018GL079026.

Ojha, L., Wray, J.J., Murchie, S.L., McEwen, A.S., Wolff, M.J., Karunatillake, S., 2013. Spectral constraints on the formation mechanism of recurring slope lineae. *Geophysical Research Letters*, **40**(1), 5621–5626, doi:10.1002/2013GL057893.

Ojha, L., McEwen, A., Dundas, C., Byrne, S., Mattson, S., Wray, J., Massé, M., Schaefer, E., 2014. HiRISE observations of recurring slope lineae (RSL) during southern summer on Mars. *Icarus*, **231**, 365–376, doi:10.1016/j.icarus.2013.12.021.

Ojha, L., Wilhelm, M. B., Murchie, S. L., McEwen, A. S., Wray, J. J., Hanley, J., Massé, M., Chojnacki, M., 2015. Spectral evidence for hydrated salts in recurring slope lineae on Mars. *Nature Geoscience*, **8**, 829–833, doi:10.1038/ngeo2546.

Ojha, L., Nerozzi, S., Lewis, K., 2019. Compositional constraints on the north polar cap of Mars from gravity and topography. *Geophysical Research Letters*, **46**, 8671-8679, doi:10.1029/2019GL082294.

Olkin, C.B., Young, L.A., Borncamp, D., Pickles, A., Sicardy, B., Assafin, M., Bianco, F.B., Buie, M.W., de Oliveira, A.D., Gillon, M., French, R.G., 2015. Evidence that Pluto's atmosphere does not collapse from occultations including the 2013 May 04 event. *Icarus*, **246**, 220–225.

Orgel, C., Hauber, E., van Gasselt, S., Reiss, D., Johnsson, A., Ramsdale, J.D., Smith, I., Swirad, Z.M., Séjourné, A., Wilson, J.T., Balme, M.R., 2019. Grid mapping the northern plains of Mars: A new overview of recent water-and ice-related landforms in Acidalia Planitia. *Journal of Geophysical Research: Planets*, **124**(2), 454–482, doi:10.1029/2018JE005664.

Orloff, T., Kreslavsky, M., Asphaug, E., Korteniemi, J., 2011. Boulder movement at high northern latitudes of Mars. *Journal of Geophysical Research*, **116**, E11006, doi:10.1029/2011JE003811.

Ould Ahmedou, D., Ould Mahfoudh, A., Dupont, P., Ould El Moctar, A., Valance, A., Rasmussen, K.R., 2007. Barchan dune mobility in Mauritania related to dune and interdune sand fluxes. *Journal of Geophysical Research: Earth Surface*, **112**, F02016, doi:10.1029/2006JF000500.

Owen, T.C., Roush, T.L., Cruikshank, D.P., Elliot, J.L., Young, L.A., deBergh, C., Schmitt, B., Geballe, T.R., Brown, R.H., Bartholomew. M.J., 1993. Surface ices and the atmospheric composition of Pluto. *Science*, **261**,745-748.

Pahtz, T., Clark, A.H., Valyrakis, M., Duran, O. 2020. The physics of sediment transport initiation, cessation, and entrainment across aeolian and fluvial environments. *Reviews of Geophysics*, **58**(1), e2019RG000679, doi:10.1029/2019RG000679.

Pan, C., Rogers, A.D., 2017. Occurrence and scale of compositional heterogeneity in martian dune fields: Toward understanding the effects of aeolian sorting on martian sediment compositions. *Icarus*, **282**, 56–69, doi:10.1016/j.icarus.2016.09.021.

Parra, S.A., Milkovich, S.M., Byrne, S., Russell, P.S., 2017. Variations in texture of the north polar residual cap of Mars. Presented at the *48th Lunar and Planetary Science Conference*, Ab. 1719.

Parteli, E.J., Herrmann, H.J., 2007. Dune formation on the present Mars. *Physical Review E*, **76**(4), 041307, doi:10.1103/PhysRevE.76.041307.

Pasquon, K., Gargani, J., Massé, M., Conway, S.J., 2016. Present-day formation and seasonal evolution of linear dune gullies on Mars. *Icarus*, **274**, 195–210, doi:10.1016/j.icarus.2016.03.024.

Pasquon, K., Gargani, J., Nachon, M., Conway, S.J., Massé, M., Jouannic, G., Balme, M.R., Costard, F., Vincendon, M., 2019a. Are different martian gully morphologies due to different processes on the Kaiser dune field? *Geological Society, London, Special Publications*, **467**. doi:10.1144/SP467.13

Pasquon, K., Gargani, J., Massé, M., Vincendon, M., Conway, S.J., Séjourné, A., Jomelli, V., Balme, M.R., Lopez, S., Guimpier, A., 2019b. Present-day development of gully-channel sinuosity by carbon dioxide gas supported flows on Mars. *Icarus*, **329**, 296–313. doi:10.1016/j.icarus.2019.03.034

Pathare, A.V., Feldman, W.C., Prettyman, T.H., Maurice, S., 2018. Driven by excess? Climatic implications of new global mapping of near-surface water-equivalent hydrogen on Mars. *Icarus*, **301**, 97–116, doi:10.1016/j.icarus.2017.09.031.

Pelkey, S., Jakosky, B., 2002. Surficial geologic surveys of Gale crater and Melas Chasma, Mars: Integration of remote-sensing data. *Icarus*, **160**(2), 228–257, doi:10.1006/icar.2002.6978.

Pelletier, J.D., Kolb, K.J., Kirk, R.L., 2008. Recent bright gully deposits on Mars: Wet or dry flow? *Geology*, **36**, 211–214, doi:10.1130/G24346A.1.

Petersen, E.I., Holt, J.W., Levy, J.S., 2018. High ice purity of martian lobate debris aprons at the regional scale: evidence from an orbital radar sounding survey in Deuteronilus and Protonilus Mensae. *Geophysical Research Letters*, **45**(21), 11–595, doi:10.1029/2018GL079759.

Phillips, R.J., Davis, B.J., Tanaka, K.L., Byrne, S., Mellon, M.T., Putzig, N.E., Haberle, R.M., Kahre, M.A., Campbell, B.A., Carter, L.M., Smith, I.B., 2011. Massive CO_2 ice deposits sequestered in the south polar layered deposits of Mars. *Science*, **332**(6031), 838–841, doi:10.1126/science.1203091.

Pilorget, C., Forget, F., 2016. Formation of gullies on Mars by debris flows triggered by CO_2 sublimation. *Nature Geoscience*, **9**(1), 65–69, doi:10.1038/ngeo2619.

Pilorget, C., Forget, F., Millour, E., Vincendon, M., Madeleine, J.B., 2011. Dark spots and cold jets in the polar regions of Mars: New clues from a thermal model of surface CO_2 ice. *Icarus*, **213**(1), 131–149, doi:10.1016/j.icarus.2011.01.031.

Pilorget, C., Edwards, C.S., Ehlmann, B.L., Forget, F., Millour, E., 2013. Material ejection by the cold jets and temperature evolution of the south seasonal polar cap of Mars from THEMIS/CRISM observations and implications for surface properties. *Journal of Geophysical Research: Planets*, **118**(12), 2520–2536, doi:10.1002/2013JE004513.

Piqueux, S., Christensen, P.R., 2008. North and south subice gas flow and venting of the seasonal caps of Mars: A major geomorphological agent. *Journal of Geophysical Research: Planets*, **113**, E06005, doi:10.1029/2007JE003009.

Piqueux S., Byrne S., Richardson M. I., 2003. Sublimation of Mars' southern seasonal CO_2 ice cap and the formation of spiders. *Journal of Geophysical Research,* **108**, 5084, doi:10.1029/2002JE002007.

Piqueux, S., Byrne, S., Kieffer, H.H., Titus, T.N., Hansen, C.J., 2015a. Enumeration of Mars years and seasons since the beginning of telescopic exploration. *Icarus*, **251**, 332–338, doi:10.1016/j.icarus.2014.12.014.

Piqueux, S., Kleinböhl, A., Hayne, P.O., Kass, D.M., Schofield, J.T., McCleese, D.J., 2015b. Variability of the martian seasonal CO_2 cap extent over eight Mars years. *Icarus*, **251**, 164–180, doi:10.1016/j.icarus.2014.10.045.

Piqueux, S., Kleinböhl, A., Hayne, P.O., Heavens, N.G., Kass, D.M., McCleese, D.J., Schofield, J.T., Shirley, J.H., 2016. Discovery of a widespread low-latitude diurnal CO_2 frost cycle on Mars. *Journal of Geophysical Research: Planets*, **121**(7), 1174–1189, doi:10.1002/2016JE005034.

Piqueux, S., Buz, J., Edwards, C.S., Bandfield, J.L., Kleinböhl, A., Kass, D.M., Hayne, P.O., the MCS and THEMIS Teams, 2019. Widespread shallow water ice on Mars at high latitudes and midlatitudes. *Geophysical Research Letters*, *46*(24), 14290–14298.

Pollack, J.B., Haberle, R.M., Schaeffer, J., Lee, H., 1990. Simulations of the general circulation of the Martian atmosphere. 1. Polar processes. *Journal of Geophysical Research*, **95**, 1447–1473, doi:10.1029/JB095iB02p01447.

Pollack, J.B., Haberle, R.M., Murphy, J.R., Schaeffer, J., Lee, H., 1993. Simulations of the general circulation of the Martian atmosphere. 2. Seasonal pressure variations. *Journal of Geophysical Research*, **98**, 3149–3181, doi:10.1029/92JE02947.

Pommerol, A., Appéré, T., Portyankina, G., Aye, K.-M., Thomas, N., Hansen, C.J., 2013. Observations of the northern seasonal polar cap on Mars III: CRISM/HiRISE observations of spring sublimation. *Icarus*, **225**, 911–922, doi:10.1016/j.icarus.2012.08.039.

Pommerol, A., Jost, B., Poch, O., Yoldi, Z., Brouet, Y., Gracia-Berná, A., Cerubini, R., Galli, A., Wurz, P., Gundlach, B., Blum, J., Carrasco, N., Szopa, C., Thomas, N., 2019. Experimenting with mixtures of water ice and dust as analogues for icy planetary material. *Space Science Reviews*, **215**, 37, doi:10.1007/s11214-019-0603-0.

Portyankina, G., Markiewicz, W.J., Thomas, N., Hansen, C.J., Milazzo, M., 2010. HiRISE observations of gas sublimation-driven activity in Mars' southern polar regions: III. Models of processes involving translucent ice. *Icarus*, **205**, 311–320, doi:10.1016/j.icarus.2009.08.029.

Portyankina, G., Pommerol, A., Aye, K.-M., Hansen, C.J., Thomas, N., 2012. Polygonal cracks in the seasonal semi-translucent CO_2 ice layer in martian polar areas. *Journal of Geophysical Research: Planets*, **117**, E02006, doi:10.1029/2011JE003917.

Portyankina, G., Hansen, C.J., Aye, K.-M., 2017. Present-day erosion of Martian polar terrain by the seasonal CO_2 jets. *Icarus,* **282**, 93–103, doi:10.1016/j.icarus.2016.09.007.

Portyankina, G., Merrison, J., Iversen, J.J., Yoldi, Z., Hansen, C.J., Aye, K.-M., Pommerol, A., Thomas, N., 2019. Laboratory investigations of the physical state of CO_2 ice in a simulated Martian environment. *Icarus*, **322**, 210–220, doi:10.1016/j.icarus.2018.04.021.

Preston, S., Chojnacki, M., 2019. Aeolian ripple rate variability in response to different boundary conditions. Presented at the *50th Lunar and Planetary Science Conference*, Ab. 2142.

Prockter, L.M., Head, J.W., Pappalardo, R.T., Senske, D.A., Neukum, G., Wagner, R., Wolf, U., Oberst, J.O., Giese, B., Moore, J.M., Chapman, C.R., 1998. Dark terrain on Ganymede: Geological mapping and interpretation of Galileo Regio at high resolution. *Icarus*, **135**(1), 317–344.

Putzig, N.E., Mellon, M.T., 2007. Apparent thermal inertia and the surface heterogeneity of Mars. *Icarus*, **191**(1), 68–94, doi:10.1016/j.icarus.2007.05.013.

Putzig, N.E., Smith, I.B., Perry, M.R., Foss II, F.J., Campbell, B.A., Phillips, R.J., Seu, R., 2018. Three-dimensional radar imaging of structures and craters in the martian polar caps. *Icarus*, **308**, pp.138–147.

Raack, J., Reiss, D., Appéré, T., Vincendon, M., Ruesch, O., Hiesinger, H., 2015. Present-day seasonal gully activity in a south polar pit (Sisyphi Cavi) on Mars. *Icarus*, **251**, 226–243, doi:10.1016/j.icarus.2014.03.040.

Raack, J., Conway, S.J., Herny, C., Balme, M.R., Carpy, S., Patel, M.R., 2017. Water induced sediment levitation enhances downslope transport on Mars. *Nature Communications*, **8**(1), 1511, doi:10.1038/s41467-017-01213-z.

Raack, J., Conway, S.J., Heyer, T., Bickel, V.T., Philippe, M., Hiesinger, H., Johnsson, A., Massé, M., 2020. Present-day gully activity in Sisyphi Cavi, Mars - Flow-like features and block movements. *Icarus,* **350**, 113899, doi:10.1016/j.icarus.2020.113899

Radebaugh, J., Lorenz, R.D., Lunine, J.I., Wall, S.D., Boubin, G., Reffet, E., Kirk, R.L., Lopes, R.M., Stofan, E.R., Soderblom, L., Allison, M., 2008. Dunes on Titan observed by Cassini RADAR. *Icarus*, **194**(2), 690–703, doi:10.1016/j.icarus.2007.10.015

Radebaugh, J., Lorenz, R., Farr, T., Paillou, P., Savage, C., Spencer, C., 2010. Linear dunes on Titan and Earth: Initial remote sensing comparisons. *Geomorphology*, **121**(1–2), 122–132, doi:10.1016/j.geomorph.2009.02.022.

Rampe, E.B., Lapôtre, M.G.A., Bristow, T.F., Arvidson, R.E., Morris, R.V., Achilles, C.N., Weitz, C., Blake, D.F., Ming, D.W., Morrison, S.M., Vaniman, D.T., 2018. Sand mineralogy within the Bagnold dunes, Gale crater, as observed in situ and from orbit. *Geophysical Research Letters*, **45**(18), 9488–9497, doi:10.1029/2018GL079073.

Ramsdale, J.D., Balme, M.R., Gallagher, C., Conway, S.J., Smith, I.B., Hauber, E., Orgel, C., Séjourné, A., Costard, F., Eke, V.R., van Gasselt, S.A., 2019. Grid mapping the northern plains of Mars: Geomorphological, radar, and water-equivalent hydrogen results from Arcadia Plantia. *Journal of Geophysical Research: Planets*, **124**(2), 504–527, doi:10.1029/2018JE005663.

Reiss, D., Erkeling, G., Bauch, K.E., Hiesinger, H., 2010. Evidence for present day gully activity on the Russell crater dune field, Mars. *Geophysical Research Letters*, **37**(6), L06203, doi:10.1029/2009GL042192.

Roback, K.P., Runyon, K.D., Avouac, J.-P., Newman, C.E., Ayoub, F., 2019. Understanding ripple and whole-dune motion at active martian dune fields. Presented at the *50th Lunar and Planetary Science Conference*, Ab. 3169.

Roback, K.P., Runyon, K.D., Avouac, J.-P. 2020. Craters as sand traps: Dynamics, history, and morphology of modern sand transport in an active dune field. *Icarus*, **342**, 113642, doi:10.1016/j.icarus.2020.113642

Roberts, G.P., Matthews, B., Bristow, C., Guerrieri, L., Vetterlein, J., 2012. Possible evidence of paleomarsquakes from fallen boulder populations, Cerberus Fossae, Mars. *Journal of Geophysical Research: Planets*, **117**, E02009, doi:10.1029/2011JE003816.

Rogers, A.D., Aharonson, O., 2008. Mineralogical composition of sands in Meridiani Planum determined from Mars Exploration Rover data and comparison to orbital measurements. *Journal of Geophysical Research*, **113**, E06S14, doi:10.1029/2007JE002995.

Rubin, D.M., 1987. Cross-bedding, bedforms and paleocurrents. In *Concepts in Sedimentology and Palaeontology*, Editor D.M. Rubin, SEPM, 1, 187 pp.

Rubin, D. M., 2012. A unifying model for planform straightness of ripples and dunes in air and water. *Earth Science Review*, **113**, 176–185, doi:10.1016/j.earscirev.2012.03.010.

Rubin, D.M., Carter, C.L., 2006. Bedforms and Cross-Bedding in Animation. SEPM, Atlas Series, 2, DVD.

Rubin, D.M., Hunter, R.E. (1987). Bedform alignment in directionally varying flows. *Science*, **237**(4812), 276–278, doi:10.1126/science.237.4812.276.

Rummel, J.D., Beaty, D.W., Jones, M.A., Bakermans, C., Barlow, N.G., Boston, P.J., Chevrier, V.F., Clark, B.C., de Vera, J.-P.P., Gough, R.V., Hallsworth, J.E., Head, J.W., Hipkin, V.J., Kieft, T.L., McEwen, A.S., Mellon, M.T., Mikucki, J.A., Nicholson, W.L., Omelon, C.R., Peterson, R., Roden, E.E., Sherwood Lollar, B., Tanaka, K.L., Viola, D., Wray, J.J., 2014. A new analysis of Mars "special regions": findings of the second MEPAG special regions science analysis group (SR-SAG2). *Astrobiology,* 14 (11), 887–968, doi:10.1089/ast.2014.1227.

Runyon, K.D., Bridges, N.T., Ayoub, F., Newman, C.E., Quade, J.J., 2017. An integrated model for dune morphology and sand fluxes on Mars. *Earth and Planetary Science Letters,* **457**, 204-212, doi:10.1016/j.epsl.2016.09.054.

Russell, P., Thomas, N., Byrne, S., Herkenhoff, K., Fishbaugh, K., Bridges, N., Okubo, C., Milazzo, M., Daubar, I., Hansen, C., McEwen, A., 2008. Seasonally active frost-dust avalanches on a north polar scarp of Mars captured by HiRISE. *Geophysical Research Letters*, **35**, L23204, doi:10.1029/2008GL035790.

Russell, P.S., Byrne, S., Dawson, L.C., 2014. Active powder avalanches on the steep north polar scarps of Mars: 4 years of HiRISE observation. Presented at the *45th Lunar and Planetary. Science Conference*, Ab. 2688.

Russell, P.S., Parra, S.A., Milkovich, S.M., Becerra, P., Byrne, S., 2019. Visible and topographic texture of the north polar residual cap of Mars. Presented at the *50th Lunar and Planetary. Science Conference*, Ab. 3048.

Sagan, C., Veverka, J., Fox, P., Dubisch, R., Lederberg, J., Levinthal, E., Quam, L., Tucker, R., Pollack, J.B., Smith, B.A., 1972. Variable features on Mars: Preliminary Mariner 9 television results. *Icarus,* **17**(2), 346–372, doi:10.1016/0019-1035(72)90005-X.

Sagan, C., Toon, O.B., Gierasch, P.J., 1973. Climatic change on Mars. *Science*, **181**(4104), 1045–1049.

Schaefer, E.I., McEwen, A.S., Sutton, S.S., 2019. A case study of recurring slope lineae (RSL) at Tivat crater: Implications for RSL origins. *Icarus*, **317**, 621-648, doi:10.1016/j.icarus.2018.07.014.

Schenk, P., Singer, K., Beyer, R., Beddingfield, C., Robbins, S.J., McKinnon, W.B., Lauer, T.R., Verbiscer, A.J., Keane, James. T., Dhingra, R.D., Moore, J., Parker, J.W., Olkin, C., Spencer, J., Weaver, H., Stern, S.A., 2020. Origins of pits and troughs and degradation on a small

primitive planetesimal in the Kuiper Belt: high-resolution topography of (486958) Arrokoth (aka 2014 MU69) from New Horizons. *Icarus*, 113834, doi:10.1016/j.icarus.2020.113834.

Schmidt, F., Andrieu, F., Costard, F., Kocifaj, M., Meresescu, A., 2017. Formation of recurring slope lineae on Mars by rarefied gas–triggered granular flows. *Nature Geoscience*, **10**, 270–273, doi:10.1038/ngeo2917.

Schorghofer, N., Aharonson, O., 2005. Stability and exchange of subsurface ice on Mars. *Journal of Geophysical Research*, **110**, E05003, doi:10.1029/2004JE002350.

Schorghofer, N., Edgett, K.S., 2006. Seasonal surface frost at low latitudes on Mars. *Icarus*, **180**, 321–334, doi:10.1016/j.icarus.2005.08.022.

Schorghofer, N., Forget, F., 2012. History and anatomy of subsurface ice on Mars. *Icarus*, **220**, 1112–1120, doi:10.1016/j.icarus.2012.07.003.

Schorghofer, N., Aharonson, O., Khatiwala, S., 2002. Slope streaks on Mars: Correlations with surface properties and the potential role of water. *Geophysical Research Letters*, 29, 41-1–41-4, doi:10.1029/2002GL015889.

Schorghofer, N., Levy, J.S., Goudge, T.A., 2019. High-resolution thermal environment of Recurring Slope Lineae in Palikir Crater, Mars, and its implications for volatiles. *Journal of Geophysical Research Planets*, **124**(11), 2852–2862.

Schwamb, M.E., Aye, K.-M., Portyankina, G., Hansen, C.J., Allen, C., Allen, S., Calef, F.J., Duca, S., McMaster, A., Miller, G.R.M., 2018. Planet Four: Terrains – Discovery of araneiforms outside of the south polar layered deposits. *Icarus*, **308**, 148–187, doi:10.1016/j.icarus.2017.06.017.

Scully, J.E.C., Russell, C.T., Yin, A., Jaumann, R., Carey, E., Castillo-Rogez, J., McSween, H.Y., Raymond, C.A., Reddy, V., Le Corre, L., 2015. Geomorphological evidence for transient water flow on Vesta. *Earth and Planetary Science Letter*s, **411**, 151–163, doi:10.1016/j.epsl.2014.12.004.

Seelos, K.D., Seelos, F.P., Viviano-Beck, C.E., Murchie, S.L., Arvidson, R.E., Ehlmann, B.L., Fraeman, A.A., 2014. Mineralogy of the MSL Curiosity landing site in Gale crater as observed by MRO/CRISM. *Geophysical Research Letters*, **41**, 4880–4887, doi:10.1002/2014GL060310.

Séjourné, A., Costard, F., Gargani, J., Soare, R.J., Fedorov, A., Marmo, C., 2011. Scalloped depressions and small–sized polygons in western Utopia Planitia, Mars: A new formation hypothesis. *Planetary and Space Science*, **59**, 412–422.

Séjourné, A., Costard, F., Gargani, J., Soare, R.J., Marmo, C., 2012. Evidence of an eolian ice-rich and stratified permafrost in Utopia Planitia, Mars. *Planetary and Space Science*, **60**, 248–254.

Séjourné, A., Costard, F., Swirad, Z.M., Łosiak, A., Bouley, S., Smith, I., Balme, M.R., Orgel, C., Ramsdale, J.D., Hauber, E., Conway, S.J., 2019. Grid mapping the northern plains of Mars: Using morphotype and distribution of ice-related landforms to understand multiple ice-rich deposits in Utopia Planitia. *Journal of Geophysical Research: Planets*, **124**(2), 483–503, doi:10.1029/2018JE005665.

Senthil Kumar, P., Krishna, N., Prasanna Lakshmi, K.J., Raghukanth, S.T.G., Dhabu, A., Platz, T., 2019. Recent seismicity in Valles Marineris, Mars: Insights from young faults, landslides,

boulder falls and possible mud volcanoes. *Earth and Planetary Science Letters*, **505**, 51–64, doi:10.1016/j.epsl.2018.10.008.

Shao, Y., Lu, H., 2000. A simple expression for wind erosion threshold friction velocity. *Journal of Geophysical Research: Atmospheres*, **105**(D17), 22437–22443, doi:10.1029/2000JD900304.

Sharp, R.P., 1963. Wind ripples. *Journal of Geology*, **71**(5), 617–636.

Sharp, R.P., 1973. Mars: Fretted and chaotic terrains. *Journal of Geophysical Research,* **78**, 4073–4083.

Silvestro, S., Fenton, L.K., Vaz, D.A., Bridges, N.T., Ori, G.G., 2010. Ripple migration and dune activity on Mars: Evidence for dynamic wind processes. *Geophysical Research Letters*, **37**, L20203.

Silvestro, S., Fenton, L.K., Michaels, T.I., Valdez, A., Ori, G.G., 2012. Interpretation of the complex dune morphology on Mars: dune activity, modelling and a terrestrial analogue. *Earth Surface Processes and Landforms*, **37** (13), 1424–1436.

Silvestro, S., Vaz, D.A., Ewing, R.C., Rossi, A.P., Fenton, L.K., Michaels, T.I., Flahaut, J., Geissler, P.E., 2013. Pervasive aeolian activity along rover Curiosity's traverse in Gale crater, Mars. *Geology*, **41**, 483–486, doi:10.1130/G34162.1.

Silvestro, S., Chojnacki, M., Vaz, D.A., Cardinale, M., Yizhaq, H., Esposito, F., 2020. Megaripple migration on Mars. *Journal of Geophysical Research: Planets*, **125**, e2020JE006446, doi:10.1029/2020JE006446.

Sizemore, H.G., Platz, T., Schorghofer, N., Prettyman, T.H., De Sanctis, M.C., Crown, D.A., Schmedemann, N., Neesemann, A., Kneissl, T., Marchi, S., Schenk, P.M., Bland, M.T., Schmidt, B.E., Hughson, K.H.G., Tosi, F., Zambon, F., Mest, S.C., Yingst, R.A., Williams, D.A., Russell, C.T., Raymond, C.A., 2017. Pitted terrains on (1) Ceres and implications for shallow subsurface volatile distribution. *Geophysical Research Letters*, **44**, 6570–6578, doi:10.1002/2017GL073970.

Sizemore, H.G., Schmidt, B.E., Buczkowski, D.A., Sori, M.M., Castillo-Rogez, J.C., Berman, D.C., Ahrens, C., Chilton, H.T., Hughson, K.H.G., Duarte, K., Otto, K.A., Bland, M.T., Neesemann, A., Scully, J.E.C., Crown, D.A., Mest, S.C., Williams, D.A., Platz, T., Schenk, P., Landis, M.E., Marchi, S., Schorghofer, N., Quick, L.C., Prettyman, T.H., De Sanctis, M.C., Nass, A., Thangjam, G., Nathues, A., Russell, C.T., Raymond, C.A., 2019. A global inventory of ice-related morphological features on dwarf planet Ceres: Implications for the evolution and current state of the cryosphere. *Journal of Geophysical Research: Planets*, **124**, 1650–1689, doi:10.1029/2018JE005699.

Sletten, R.S., Hallet, B., Fletcher, R.C., 2003. Resurfacing time of terrestrial surfaces by the formation and maturation of polygonal patterned ground. *Journal of Geophysical Research: Planets*, **108**(E4), 8044, doi:10.1029-2002JE001914.

Smith, D.E., Zuber, M.T., Neumann, G.A., 2001. Seasonal variations of snow depth on Mars. *Science*, **294**(5549), 2141–2146.

Smith, I.B., Putzig, N.E., Holt, J.W., Phillips, R.J., 2016. An ice age recorded in the polar deposits of Mars. *Science*, **352**, 1075–1079, doi:10.1126/science.aad6968.

3693 Smith, I.B., Hayne, P.O., Byrne, S., Becerra, P., Kahre, M., Calvin, W., Hvidberg, C., Milkovich,
3694 S., Buhler, P., Landis, M., Horgan, B., 2020. The Holy Grail: A road map for unlocking the
3695 climate record stored within Mars' polar layered deposits. *Planetary and Space Science*, **184**,
3696 104841, doi:10.1016/j.pss.2020.104841.

3697 Smith, M.D., 2002. The annual cycle of water vapor on Mars as observed by the Thermal
3698 Emission Spectrometer. *Journal of Geophysical Research: Planets*, **107**(E11), 25-1–25-19,
3699 doi:10.1029/2001JE001522.

3700 Smith, M.D., 2008. Spacecraft observations of the martian atmosphere. *Annual Review Earth*
3701 *and Planetary Science*, **36**, 191–219.

3702 Smith, I.B., Holt, J.W., 2010. Onset and migration of spiral troughs on Mars revealed by orbital
3703 radar. *Nature*, **465**(7297), 450–453, doi:10.1038/nature09049

3704 Smith, P.H., Tamppari, L.K., Arvidson, R.E., Bass, D., Blaney, D., Boynton, W.V., Carswell, A.,
3705 Catling, D.C., Clark, B.C., Duck, T., DeJong, E., 2009. H_2O at the Phoenix landing site.
3706 *Science*, **325**(5936), 58–61.

3707 Smoluchowski, R., 1968. Mars: Retention of ice. *Science*, **159**(3821), 1348–1350.

3708 Soare, R.J., Kargel, J.S., Osinski, G.R., Costard, F., 2007. Thermokarst processes and the origin
3709 of crater-rim gullies in Utopia and western Elysium Planitia. *Icarus*, **191**, 95–112.

3710 Soare, R.J., Osinski, G.R., Roehm, C.L., 2008. Thermokarst lakes and ponds on Mars in the very
3711 recent (late Amazonian) past. *Earth and Planetary. Science Letters*, **272**, 382–393.

3712 Soare, R.J., Séjourné, A., Pearce, G., Costard, F., Osinski, G.R., 2011. The Tuktoyaktuk
3713 Coastlands of northern Canada: A possible ‘‘wet” periglacial analog of Utopia Planitia, Mars.
3714 *Geological Society of American, Special Paper*, **483**, 203–218.

3715 Soare, R.J., Conway, S.J., Dohm, J.M., 2014. Possible ice-wedge polygons and recent landscape
3716 modification by “wet” periglacial processes in and around the Argyre impact basin, Mars.
3717 *Icarus*, **233**, 214–228.

3718 Soare, R.J., Conway, S.J., Gallagher, C., Dohm, J.M., 2016. Sorted (clastic) polygons in the
3719 Argyre region, Mars, and possible evidence of pre- and post-glacial periglaciation in the Late
3720 Amazonian Epoch. *Icarus*, **264**, 184–197.

3721 Soare, R.J., Conway, S.J., Gallagher, C., Dohm, J.M., 2017. Ice-rich (periglacial) vs icy (glacial)
3722 depressions in the Argyre region, Mars: a proposed cold-climate dichotomy of landforms.
3723 *Icarus*, **282**, 70–83, doi:10.1016/j.icarus.2016.09.009.

3724 Soare, R.J., Conway, S.J., Gallagher, C.J., Williams, J.P., Osinski, G.R., 2018. Paleo-periglacial
3725 and “ice-rich” complexes in Utopia Planitia. In *Dynamic Mars*, pp. 209–237, Elsevier.

3726 Soare, R.J., Conway, S.J., Williams, J.P., Gallagher, C., Mc Keown, L.E., 2019. Possible (closed
3727 system) pingo and ice-wedge/thermokarst complexes at the mid latitudes of Utopia Planitia,
3728 Mars. *Icarus*, **342**, 113233, doi:10.1016/j.icarus.2019.03.010.

3729 Soderblom, L.A., Kieffer, S.W., Becker, T.L., Brown, R.H., Cook, A.F., Hansen, C.J., Johnson,
3730 T.V., Kirk, R.L., Shoemaker, E.M., 1990.Triton's geyser-like plumes: Discovery and basic
3731 characterization. *Science*, **250**(4979), 410–415.

Sori, M.M., Byrne, S., Hamilton, C.W., Landis, M.E., 2016. Viscous flow rates of icy topography on the north polar layered deposits of Mars. *Geophysical Research Letters*, **43**, 541–549, doi:10.1002/2015GL067298.

Sori, M.M., Bapst, J., Bramson, A.M., Byrne, S., Landis, M.E., 2017. A Wunda-full world? Carbon dioxide ice deposits on Umbriel and other Uranian moons. *Icarus*, **290**, 1–13, doi:10.1016/j.icarus.2017.02.029.

Soto, A., Mischna, M., Schneider, T., Lee, C., Richardson, M., 2015. Martian atmospheric collapse: Idealized GCM studies. *Icarus,* **250**, 553–569, doi:10.1016/j.icarus.2014.11.028.

Spencer, J., Denk, T., 2010. Formation of Iapetus' extreme albedo dichotomy by exogenically triggered thermal ice migration. *Science*, **327**, 432–435.

Spiga, A., Smith, I., 2018. Katabatic jumps in the martian northern polar regions. *Icarus*, **308**, 197–208, doi: 10.1016/j.icarus.2017.10.021.

Steele, L.J., Balme, M.R., Lewis, S.R., 2017. Regolith-atmosphere exchange of water in Mars' recent past. *Icarus*, **284**, 233–248, doi:10.1016/j.icarus.2016.11.023.

Stern, S.A., Bagenal, F., Ennico, K., Gladstone, G.R., Grundy, W.M., McKinnon, W.B., Moore, J.M., Olkin, C.B., Spencer, J.R., Weaver, H.A., Young, L.A., 2015. The Pluto system: Initial results from its exploration by New Horizons. *Science*, **350**(6258), aad1815, doi:10.1126/science.aad1815.

Stillman, D.E., 2018. Unraveling the mysteries of recurring slope lineae. In *Dynamic Mars: Recent and Current Landscape Evolution of the Red Planet*, Editors R.J. Soare, S.J. Conway, S.M. Clifford, Elsevier, 474 pages, doi:10.1016/C2016-0-04489-3.

Stillman, D.E., Grimm, R.E., 2018. Two pulses of seasonal activity in martian southern mid-latitude recurring slope lineae (RSL). *Icarus*, **302**, 126–133, doi:10.1016/j.icarus.2017.10.026.

Stillman, D.E., Michaels, T.I., Grimm, R.E, Harrison, K.P., 2014. New observations of martian southern mid-latitude recurring slope lineae (RSL) imply formation by freshwater subsurface flows. *Icarus*, **233**, 328–341, doi:10.1016/j.icarus.2014.01.017.

Stillman, D.E., Michaels, T.I., Grimm, R.E., Hanley, J., 2016. Observations and modeling of northern mid-latitude recurring slope lineae (RSL) suggest recharge by a present-day martian briny aquifer. *Icarus*, **265**, 125–138, doi:10.1016/j.icarus.2015.10.007.

Stillman, D.E., Michaels, T.I., Grimm, R.E., 2017. Characteristics of the numerous and widespread recurring slope lineae (RSL) in Valles Marineris, Mars. *Icarus*, **285**, 195–210, doi:10.1016/j.icarus.2016.10.025.

Stillman, D.E., Bue, B.D., Wagstaff, K.L., Primm, K.M., Michaels, T.I., Grimm, R.E., 2020. Evaluation of wet and dry recurring slope lineae (RSL) formation mechanisms based on quantitative mapping of RSL in Garni crater, Valles Marineris, Mars. *Icarus*, **335**, 113420.

Stockstill-Cahill, K.R., Anderson, F.S., Hamilton, V.E., 2008. A study of low-albedo deposits within Amazonis Planitia craters: Evidence for locally derived ultramafic to mafic materials. *Journal of Geophysical Research,* **113**, doi:10.1029/2007JE003036.

Sullivan, R., Kok, J., 2017. Aeolian saltation on Mars at low wind speeds. *Journal of Geophysical Research: Planets*, **122**, 2111–2143, doi:10.1002/2017JE005275.

3773 Sullivan, R., Banfield, D., Bell, J.F., Calvin, W., Fike, D., Golombek, M., Greeley, R.,
3774 Grotzinger, J., Herkenhoff, K., Jerolmack, D., Malin, M., 2005. Aeolian processes at the
3775 Mars exploration rover Meridiani Planum landing site. *Nature*, **436**(7047), 58–61,
3776 doi:10.1038/nature03641.

3777 Sullivan, R., Arvidson, R., Bell III, J.F., Gellert, R., Golombek, M., Greeley, R., Herkenhoff, K.,
3778 Johnson, J., Thompson, S., Whelley, P., Wray, J., 2008. Wind-driven particle mobility on
3779 Mars: Insights from Mars Exploration Rover observations at "El Dorado" and surroundings
3780 at Gusev Crater. *Journal of Geophysical Research*, **113**, E06S07,
3781 doi:10.1029/2008JE003101.

3782 Sullivan, R., Kok, J.F., Katra, I., Yizhaq, H. 2020. A broad continuum of aeolian impact ripple
3783 morphologies on Mars is enabled by low wind dynamic pressures. *Journal of Geophysical*
3784 *Research: Planets*, **125**(10), e2020JE006485, doi: 10.1029/2020JE006485

3785 Sunshine, J.M., Thomas, N., El-Maarry, M.R., Farnham, T.L., 2016. Evidence for geologic
3786 processes on comets. *Journal of Geophysical Research*: *Planets*, **121**, 2194–2210,
3787 doi:10.1002/2016JE005119.

3788 Swann, C., Sherman, D.J., Ewing, R.C., 2020. Experimentally derived thresholds for windblown
3789 sand on Mars. *Geophysical Research Letters*, **47**, e2019GL084484,
3790 doi:10.1029/2019GL084484.

3791 Sweeney, J., Warner, N.H., Ganti, V., Golombek, M.P., Lamb, M.P., Fergason, R., Kirk, R.,
3792 2018. Degradation of 100 m-scale rocky ejecta craters at the InSight landing site on Mars and
3793 implications for surface processes and erosion rates in the Hesperian and Amazonian.
3794 *Journal of Geophysical Research*, **123**, 2732–2759, doi:10.1029/2018JE005618.

3795 Svitek, T., Murray, B.C., 1990. Winter frost at Viking Lander 2 site. *Journal of Geophysical*
3796 *Research*, **95**, 1495-1510.

3797 Sylvest, M.E., Conway, S.J., Patel, M.R., Dixon, J.C., Barnes, A., 2016. Mass wasting triggered
3798 by seasonal CO_2 sublimation under Martian atmospheric conditions: Laboratory experiments.
3799 *Geophysical Research Letters*, **43**(24), 12–363, doi:10.1002/2016GL071022.

3800 Sylvest, M.E., Dixon, J.C., Conway, S.J., Patel, M.R., McElwaine, J.N., Hagermann, A., Barnes,
3801 A., 2019. CO_2 sublimation in martian gullies: Laboratory experiments at varied slope angle
3802 and regolith grain sizes. *Geological Society, London, Special Publications*, 467(1), 343–371,
3803 doi:10.1144/SP467.11.

3804 Tamppari, L.K., Lemmon, M.T., 2020. Near-surface atmospheric water vapor enhancement at
3805 the Mars Phoenix lander site. *Icarus*, **343**, 113624, doi:10.1016/j.icarus.2020.113624.

3806 Tamppari, L.K., Bass, D., Cantor, B., Daubar, I., Dickinson, C., Fisher, D., Fujii, K.,
3807 Gunnlauggson, H.P., Hudson, T.L., Kass, D., Kleinböhl, A., 2010. Phoenix and MRO
3808 coordinated atmospheric measurements. *Journal of Geophysical Research: Planets*, **115**,
3809 E00E17, doi:10.1029/2009JE003415.

3810 Tanaka, K.L., 2005. Geology and insolation-driven climatic history of Amazonian north polar
3811 materials on Mars. *Nature*, **437**(7061), 991–994, doi:10.1038/nature04065.
3812

3813 Taylor, P.A., Kahanpää, H., Weng, W., Akingunola, A., Cook, C., Daly, M., Dickinson, C.,
3814 Harri, A.M., Hill, D., Hipkin, V., Polkko, J., 2010. On pressure measurement and seasonal

pressure variations during the Phoenix mission. *Journal of Geophysical Research: Planets*, **115**(E3), E00E15, doi:10.1029/2009JE003422.

Tebolt, M., Levy, J., Goudge, T., Schorghofer, N., 2020. Slope, elevation, and thermal inertia trends of recurring slope lineae initiation and termination points: Multiple possible processes occurring on coarse, sandy slopes. *Icarus,* **338**, 113536, doi:10.1016/j.icarus.2019.113536.

Telfer, M.W., Parteli, E.J., Radebaugh, J., Beyer, R.A., Bertrand, T., Forget, F., Nimmo, F., Grundy, W.M., Moore, J.M., Stern, S.A., Spencer, J., 2018. Dunes on Pluto. *Science*, **360** (6392), 992–997, doi:10.1126/science.aao2975.

Tesson, P.-A., Conway, S.J., Mangold, N., Ciazela, J., Lewis, S.R., Mège, D., 2020. Evidence for thermal–stress–induced rockfalls on Mars impact crater slopes. *Icarus*, **342**, 113503, doi:10.1016/j.icarus.2019.113503.

Thomas, M.F., McEwen, A.S., Dundas, C.M., 2020. Present-day mass wasting in sulfate-rich sediments in the equatorial regions of Mars. *Icarus*, **342**, 113566, doi:10.1016/j.icarus.2019.113566.

Thomas, N., Hansen, C.J., Portyankina, G., Russell, P.S., 2010. HiRISE observations of gas sublimation-driven activity in Mars' southern polar regions: II. Surficial deposits and their origins. *Icarus*, **205** (1), 296–310, doi:10.1016/j.icarus.2009.05.030.

Thomas, N., Sierks, H., Barbieri, C., Lamy, P.L., Rodrigo, R., Rickman, H., Koschny, D., Keller, H.U., Agarwal, J., A'Hearn, M.F., Angrilli, F., 2015. The morphological diversity of comet 67P/Churyumov–Gerasimenko. *Science*, **347** (6220), aaa0440, doi:10.1126/science.aaa0440.

Thomas, N., Cremonese, G., Ziethe, R., Gerber, M., Brändli, M., Bruno, G., Erismann, M., Gambicorti, L., Gerber, T., Ghose, K., Gruber, M., 2017. The colour and stereo surface imaging system (CaSSIS) for the ExoMars trace gas orbiter. Space science reviews, 212(3–4), 1897–1944, doi10.1007/s11214-017-0421-1.

Thomas, P., Gierasch, P., 1985. Dust devils on Mars. *Science*, **230**(4722), 175–177, doi:10.1126/science.230.4722.175.

Thomas, P.C., Malin, M.C., Edgett, K.S., Carr, M.H., Hartmann, W.K., Ingersoll, A.P., James, P.B., Soderblom, L.A., Veverka, J., Sullivan, R., 2000. North-south geological differences between the residual polar caps on Mars. *Nature*, **404**(6774), 161–164.

Thomas, P.C., Malin, M.C., James, P.B., Cantor, B.A., Williams, R.M.E. Gierasch, P., 2005. South polar residual cap of Mars: Features, stratigraphy, and changes. *Icarus*, **174**(2), 535–559.

Thomas, P.C., James, P.B., Calvin, W.M., Haberle, R., Malin, M.C., 2009. Residual south polar cap of Mars: Stratigraphy, history, and implications of recent changes. *Icarus*, **203**(2), 352–375, doi:10.1016/j.icarus.2009.05.014.

Thomas, P.C., Calvin, W.M., Gierasch, P., Haberle, R., James, P.B., Sholes, S., 2013. Time scales of erosion and deposition recorded in the residual south polar cap of Mars. *Icarus*, **225**(2), 923–932, doi:10.1016/j.icarus.2012.08.038.

Thomas, P.C., Calvin, W., Cantor, B., Haberle, R., James, P.B. and Lee, S.W., 2016. Mass balance of Mars' residual south polar cap from CTX images and other data. *Icarus*, **268**, 118–130, doi:10.1016/j.icarus.2015.12.038.

Thomas, P.C., Calvin, W.M. James, P.B., 2020. Debris accumulations of CO_2 ice in the south polar residual cap of mars: Longevity and processes. *Icarus*, 113625.

Thomas, R.J., Rothery, D.A., Conway, S.J., Anand, M., 2014. Hollows on Mercury: Materials and mechanisms involved in their formation. *Icarus*, **229**, 221–235, doi:10.1016/j.icarus.2013.11.018.

Tirsch, D., Jaumann, R., Pacifici, A., Poulet, F., 2011. Dark aeolian sediments in martian craters: composition and sources. *Journal of Geophysical Research*, **116**, E03002, doi:10.1029/2009JE003562.

Titus, T.N., Kieffer, H.H., Christensen, P.R., 2003. Exposed water ice discovered near the south pole of Mars. *Science*, **299**(5609), 1048–1051.

Titus, T.N., Williams, K.E., Cushing, G.E., 2020. Conceptual model for the removal of cold-trapped H_2O ice on the Mars northern seasonal springtime polar cap. *Geophysical Research Letters*, **47**(15), e2020GL087387, doi:10.1029/2020GL087387.

Tornabene, L.L., Osinski, G.R., McEwen, A.S., Boyce, J.M., Bray, V.J., Caudill, C.M., Grant, J.A., Hamilton, C.W., Mattson, S., Mouginis-Mark, P.J., 2012. Widespread crater-related pitted materials on Mars: Further evidence for the role of target volatiles during the impact process. *Icarus*, **220**, 348–368, doi:10.1016/j.icarus.2012.05.022.

Trafton, L., 1984. Large seasonal variations in Triton's atmosphere. *Icarus*, **58**(1), 312–324.

Tsoar, H., Greeley, R., Peterfreund, A.R., 1979. Mars: The north polar sand sea and related wind patterns. *Journal of Geophysical Research*, **84**, 8167–8180.

Turbet, M., Bolmont, E., Leconte, J., Forget, F., Selsis, F., Tobie, G., Caldas, A., Naar, J., Gillon, M., 2018. Modeling climate diversity, tidal dynamics and the fate of volatiles on TRAPPIST-1 planets. *Astronomy and Astrophysics,* **612**, A86, doi:10.1051/0004-6361/201731620.

Ulrich, M., Morgenstern, A., Günther, F., Reiss, D., Bauch, K.E., Hauber, E., Rössler, S., Schirrmeister, L., 2010. Thermokarst in Siberian ice-rich permafrost: Comparison to asymmetric scalloped depressions on Mars. *Journal of Geophysical Research*, **115**, E10009.

Umurhan, O.M., White, O.L., Moore, J.M., Howard, A.D., Schenk, P., 2016. Modeling surface processes occurring on moons of the outer Solar System. Presented at the *AGU Fall Meeting*, Ab. EP43D-08.

Vaz, D.A., Silvestro, S., Sarmento, P.T., Cardinale, M., 2017. Migrating meter-scale bedforms on martian dark dunes: Are terrestrial aeolian ripples good analogues? *Aeolian Research*, **26**, 101–116, doi:10.1016/j.aeolia.2016.08.003.

Vermeesch, P., Drake, N., 2008. Remotely sensed dune celerity and sand flux measurements of the world's fastest barchans (Bodélé, Chad). *Geophysical Research Letters,* **35**, L24404, doi:10.1029/2008GL035921.

Vincendon, M., Mustard, J., Forget, F., Kreslavsky, M., Spiga, A., Murchie, S., Bibring, J.-P., 2010a. Near-tropical subsurface ice on Mars. *Geophysical Research Letters*, **37**, L01202, doi:10.1029/2009GL041426.

Vincendon, M., Forget, F., Mustard, J., 2010b. Water ice at low to midlatitudes on Mars. *Journal of Geophysical Research: Planets*, 115, E10001, doi:10.1029/2010JE003584.

Vincendon, M., Pilorget, C., Carter, J., Stcherbinine, A., 2019. Observational evidence for a dry dust–wind origin of Mars seasonal dark flows. *Icarus*, **325**, 115–127, doi:10.1016/j.icarus.2019.02.024.

Vincent, J.-B., Bodewits, D., Besse, S., Sierks, H., Barbieri, C., Lamy, P., Rodrigo, R., Koschny, D., Rickman, H., Keller, H.U., Agarwal, J., A'Hearn, M.F., Auger, A.-T., Barucci, M.A., Bertaux, J.-L., Bertini, I., Capanna, C., Cremonese, G., Da Deppo, V., Davidsson, B., Debei, S., De Cecco, M., El–Maarry, M.R., Ferri, F., Fornasier, S., Fulle, M., Gaskell, R., Giacomini, L., Groussin, O., Guilbert–Lepoutre, A., Gutierrez–Marques, P., Gutierrez, P.J., Guttler, C., Hoekzema, N., Hofner, S., Hviid, S.F., Ip, W.-H., Jorda, L., Knollenberg, J., Kovacs, G., Kramm, R., Kuhrt, E., Kuppers, M., La Forgia, F., Lara, L.M., Lazzarin, M., Lee, V., Leyrat, C., Lin, Z.-Y., Lopez Moreno, J.J., Lowry, S., Magrin, S., Maquet, L., Marchi, S., Marzari, F., Massironi, M., Michalik, H., Moissl, R., Mottola, S., Naletto, G., Oklay, N., Pajola, M., Preusker, F., Scholten, F., Thomas, N., Toth, I., Tubiana, C., 2015. Large heterogeneities in comet 67P as revealed by active pits from sinkhole collapse. *Nature*, **523**, 63–66, doi:10.1038/nature14564.

Viola, D., McEwen, A.S., Dundas, C.M., Byrne, S., 2015. Expanded secondary craters in the Arcadia Planitia region, Mars: Evidence for tens of Myr-old shallow subsurface ice. *Icarus*, **248**, 190–204.

Viola, D., McEwen, A., 2018. Geomorphological evidence for shallow ice in the southern hemisphere of Mars. *Journal of Geophysical Research: Planets*, **123**, 262–277.

Wagstaff, K.L., Titus, T.N., Ivanov, A.B., Castaño, R., Bandfield, J.L., 2008. Observations of the north polar water ice annulus on Mars using THEMIS and TES. *Planetary and Space Science*, **56**(2), 256-265.

Wall, S.D., 1981. Analysis of condensates formed at the Viking 2 Lander site: The first winter. *Icarus*, **47**(2), 173–183.

Waite, J.H., Glein, C.R., Perryman, R.S., Teolis, B.D., Magee, B.A., Miller, G., Grimes, J., Perry, M.E., Miller, K.E., Bouquet, A., Lunine, J.I., 2017. Cassini finds molecular hydrogen in the Enceladus plume: evidence for hydrothermal processes. *Science*, **356**(6334), 155–159, doi:10.1126/science.aai8703.

Wang, A., Ling, Z., Yan, Y., McEwen, A.S., Mellon, M.T., Smith, M.D., Jolliff, B.L., Head, J., 2019. Subsurface Cl-bearing salts as potential contributors to recurring slope lineae (RSL) on Mars. *Icarus*, **333**, 464–480.

Ward, A.W., 1979. Yardangs on Mars: Evidence of recent wind erosion. *JGR Solid Earth*, **84**(B14), 8147–8166, doi:10.1016/j.pss.2020.105035.

Weitz, C.M., Plaut, J.J., Greeley, R., Saunders, R.S., 1994. Dunes and microdunes on Venus: Why were so few found in the Magellan data. *Icarus*, **112**, 282–295.

Weitz, C., Sullivan, R., Lapôtre, M., Rowland, S., Grant, J., Baker, M., Yingst, R.A., 2018. Sand grain sizes and shapes in eolian bedforms at Gale crater, Mars. *Geophysical Research Letters*, **45**(18), 9471–9479, doi:10.1029/2018GL078972.

Weitz, C.M., Sullivan, R.J., Lapôtre, M.G.A., Rowland, S.K., Grant, J.A., Baker, M.M., Yingst, R.A., 2020. Physical Properties of Sand Grains in the Bagnold Dunes at Gale Crater, Mars. Presented at the *6th International Planetary Dunes Workshop*, Ab. 3004.

Werner, B., Haff, P., Livi, R., Anderson, R., 1986. Measurement of eolian sand ripple cross-sectional shapes. *Geology*, **14**, 743, doi:10.1130/0091-7613(1986)14<743:MOESRC>2.0.CO;2.

White, O.L., Umurhan, O.M., Moore, J.M., Howard, A.D., 2016. Modeling of ice pinnacle formation on Callisto. *Journal of Geophysical Research: Planets*, **121**(1), 21–45, doi:10.1002/2015JE004846.

Widmer, J.M., Diniega, S., Hayne, P.O., Alsaeed, N., Gary-Bicas, C.E., 2020. Martian seasonal frost and snowfall in the northern mid-latitudes—growing the seasonal frost cap and contributing environmental factors. Presented at the *2020 AGU Fall Meeting*, P033-0010.

Wilcoski, A.X., Hayne, P.O., 2020. Surface roughness evolution and implications for the age of the north polar residual cap of Mars. *Journal of Geophysical Research: Planets*, **125**(12), E006570, doi:10.1029/2020JE006570.

and and Wilson, I.G. (1972). Aeolian bedforms—their development and origins. *Sedimentology*, **19**(3–4), 173–210.

Wilson, L., Head, J.W., 1994. Mars: review and analysis of volcanic eruption theory and relationships to observed landforms. *Rev. Geophys.,* **32** (3), 221–263.

Wilson, S.A., Zimbelman, J.R., 2004. Latitude-dependent nature and physical characteristics of transverse aeolian ridges on Mars. *Journal of Geophysical Research*, **109**, E10003, doi:10.1029/2004JE002247.

Withers, P., Smith, M.D., 2006. Atmospheric entry profiles from the Mars Exploration Rovers Spirit and Opportunity. *Icarus*, **185**(1), 133–142, doi:10.1016/j.icarus.2006.06.013.

Witzke, A., 2015. Pluto snow forecast poses atmospheric conundrum. *Nature*, **525**, 13–14, doi:0.1038/525013a.

Yelle, R.V., Lunine, J.I., Pollack, J.B., Brown, R.H., 1995. Lower atmospheric structure and surface–atmosphere interactions on Triton'. In *Neptune and Triton*, Editor D.P. Cruikshank,, Univ. of Arizona Press, Tucson, 1021 pages.

Yen, A.S., Gellert, R., Schröder, C., Morris, R.V., Bell, J.F., Knudson, A.T., Clark, B.C., Ming, D.W., Crisp, J.A., Arvidson, R.E., Blaney, D., 2005. An integrated view of the chemistry and mineralogy of martian soils. *Nature*, **436**, 49–54, doi:10.1038/nature03637.

Yizhaq, H., Kok, J. F., Katra, I., 2014. Basaltic sand ripples at Eagle crater as indirect evidence for the hysteresis effect in martian saltation. *Icarus*, **230**, 143–150, doi:10.1016/j.icarus.2013.08.006.

Yoldi, Z., Pommerol, A., Poch, O., Thomas, N., 2021. Reflectance study of ice and Mars soil simulant associations – I. H_2O ice. *Icarus*, 114169, doi:10.1016/j.icarus.2020.114169.

Young, L.A., 2012. Volatile Transport on Inhomogeneous Surfaces: I Analytic Expressions, with Application to Pluto's Day. *Icarus*, **221**, 80–88, doi:10.1016/j.icarus.2012.06.032.

Zalucha, A.M., Michaels, T.I., 2013. A 3D general circulation model for Pluto and Triton with fixed volatile abundance and simplified surface forcing. *Icarus*, **223**(2), 819–83, doi:10.1016/j.icarus.2013.01.026.

Zanetti, M., Hiesinger, H., Reiss, D., Hauber, E., Neukum, G., 2010. Distribution and evolution of scalloped terrain in the southern hemisphere, Mars. *Icarus*, **206**, 691–706, doi:10.1016/j.icarus.2009.09.010.

Zimbelman, J.R., 2010. Transverse aeolian ridges on Mars: First results from HiRISE images. *Geomorphology*, **121**, 22–29, doi:10.1016/j.geomorph.2009.05.012.

Zimbelman, J.R., 2019. The transition between sand ripples and megaripples on Mars. *Icarus*, **333**, 127–129, doi:10.1016/j.icarus.2019.05.017.

Zimbelman, J.R., Foroutan, M. (2020). Dingo Gap: Curiosity went up a small transverse aeolian ridge and came down a megaripple. *Journal of Geophysical Research: Planets*, **125**(12), e2020JE006489, doi: 10.1029/2020JE006489.